

<https://doi.org/10.15388/vu.thesis.815>  
<https://orcid.org/0009-0001-6987-7527>

VILNIUS UNIVERSITY  
CENTER FOR PHYSICAL SCIENCES AND TECHNOLOGY

Eimantas Kriščiūnas

# Star Clusters in the Disc of the Andromeda Galaxy

**DOCTORAL DISSERTATION**

Natural Sciences,  
Physics (N 002)

VILNIUS 2025

This dissertation was prepared between 2021 and 2025 at Center for Physical Sciences and Technology. The research was supported by the Research Council of Lithuania. Project No. S-MIP-24-98.

**Academic Supervisor:**

**Prof. Dr. Vladas Vansevičius** (Center for Physical Sciences and Technology, Natural Sciences, Physics – N 002)

**Dissertation Defence Panel:**

**Chairman – Dr. Kastytis Zubovas** (Center for Physical Sciences and Technology, Natural Sciences, Physics – N 002)

**Members:**

**Dr. Vidas Dobrovolskas** (Vilnius University, Natural Sciences, Physics – N 002),

**Dr. Mindaugas Karčiauskas** (Center for Physical Sciences and Technology, Natural Sciences, Physics – N 002),

**Prof. Dr. Arūnas Kučinskas** (Vilnius University, Natural Sciences, Physics – N 002),

**Dr. Kārlis Pukītis** (University of Latvia, Natural Sciences, Physics – N 002).

The dissertation shall be defended at a public meeting of the Dissertation Defence Panel at 14:00 on 12 September 2025 in Room D401 of the Center for Physical Sciences and Technology.

Address: Saulėtekio av. 3, Vilnius, Lithuania.

Tel. +370 5 264 8884; email: office@ftmc.lt.

The text of this dissertation can be accessed at the Vilnius University Library, as well as on the website of Vilnius University: [www.vu.lt/naujienos/ivykiu-kalendorius](http://www.vu.lt/naujienos/ivykiu-kalendorius).

<https://doi.org/10.15388/vu.thesis.815>  
<https://orcid.org/0009-0001-6987-7527>

VILNIAUS UNIVERSITETAS  
FIZINIŲ IR TECHNOLOGIJOS MOKSLŲ CENTRAS

Eimantas Kriščiūnas

# Žvaigždžių spiečiai Andromedos galaktikos diske

## DAKTARO DISERTACIJA

Gamtos mokslai,  
Fizika (N 002)

VILNIUS 2025

Disertacija rengta 2021–2025 metais Fizinių ir technologijos mokslų centre. Moksli-  
nius tyrimus rėmė Lietuvos mokslo taryba. Projektas No. S-MIP-24-98.

**Mokslinis vadovas:**

**prof. dr. Vladas Vansevičius** (Fizinių ir technologijos mokslų centras, gamtos  
mokslai, fizika – N 002)

**Gynimo taryba:**

**Pirmininkas – dr. Kastytis Zubovas** (Fizinių ir technologijos mokslų centras,  
gamtos mokslai, fizika – N 002)

**Nariai:**

**dr. Vidas Dobrovolskas** (Vilniaus universitetas, gamtos mokslai, fizika – N 002),

**dr. Mindaugas Karčiauskas** (Fizinių ir technologijos mokslų centras, gamtos  
mokslai, fizika – N 002),

**prof. dr. Arūnas Kučinskas** (Vilniaus universitetas, gamtos mokslai, fizika –  
N 002),

**dr. Kārlis Puķītis** (Latvijos universitetas, gamtos mokslai, fizika – N 002).

Disertacija ginama viešame Gynimo tarybos posėdyje 2025 m. rugsėjo mėn. 12 d.  
14:00 val. Fizinių ir technologijos mokslų centro D401 auditorijoje.

Adresas: Saulėtekio al. 3, Vilnius, Lietuva.  
Tel. +370 5 264 8884; email: office@ftmc.lt.

Disertaciją galima peržiūrėti Vilniaus universiteto bibliotekoje ir VU interneto sve-  
tainėje adresu: [www.vu.lt/naujienos/ivykiu-kalendarius](http://www.vu.lt/naujienos/ivykiu-kalendarius).

# Contents

<b>Contents</b>	<b>7</b>
List of abbreviations . . . . .	8
<b>Introduction</b>	<b>9</b>
Motivation . . . . .	9
The objective of the thesis . . . . .	11
The main tasks of the thesis . . . . .	11
Results and statements to be defended . . . . .	11
Publications included in the thesis . . . . .	11
Presentations at conferences . . . . .	11
Summer schools . . . . .	12
Contribution of the author . . . . .	12
<b>1 Andromeda (M 31) galaxy</b>	<b>13</b>
1.1 Star clusters in the disc of Andromeda . . . . .	15
1.1.1 Overview of previous surveys . . . . .	15
1.1.2 Observation methods . . . . .	16
1.1.3 Derivation of cluster parameters: overview of the methods . . . . .	17
<b>2 Observational data</b>	<b>19</b>
2.1 PHAT survey . . . . .	19
2.2 Cluster sample . . . . .	20
2.2.1 Cleaning of defects . . . . .	22
2.2.2 Centre coordinates . . . . .	23
<b>3 Multicolour aperture photometry</b>	<b>24</b>
3.1 Sky background . . . . .	25
3.2 Apertures . . . . .	26
3.3 Photometric uncertainties . . . . .	28
3.4 Multi-colour photometry results . . . . .	31
3.5 Stochastic effects of star clusters . . . . .	34
3.6 Summary . . . . .	39
<b>Appendix: Double clusters</b>	<b>41</b>

<b>4 Star cluster parameters</b>	<b>42</b>
4.1 Cluster parameter determination . . . . .	42
4.2 Comparison with other studies . . . . .	49
4.3 Properties of star clusters . . . . .	50
4.4 Cluster mass function . . . . .	53
4.5 Cluster formation history . . . . .	58
4.6 Spatial distribution . . . . .	61
4.7 Structural cluster parameters . . . . .	66
4.8 Summary . . . . .	67
<b>Appendix: Star cluster parameter derivation examples and excluded objects</b>	<b>70</b>
<b>Conclusions</b>	<b>75</b>
<b>Bibliography</b>	<b>77</b>
<b>Santrauka</b>	<b>82</b>
Darbo tikslas . . . . .	84
Uždaviniai . . . . .	84
Rezultatai ir ginamieji teiginiai . . . . .	84
Autoriaus indėlis . . . . .	84
<b>1 Andromedos (M 31) galaktika</b>	<b>85</b>
<b>2 Stebėjimų duomenys</b>	<b>87</b>
2.1 PHAT apžvalga . . . . .	87
2.2 Spiečių imtis . . . . .	87
2.2.1 Defektų valymas . . . . .	88
2.2.2 Centro koordinačių nustatymas . . . . .	89
<b>3 Apertūrinė fotometrija</b>	<b>90</b>
3.1 Fono lygio nustatymas . . . . .	90
3.2 Apertūrų parinkimas . . . . .	91
3.3 Fotometrijos rezultatai . . . . .	92
3.4 Stochastiniai žvaigždžių spiečių efektai . . . . .	95
3.5 Apibendrinimas . . . . .	97
<b>4 Žvaigždžių spiečių parametrai</b>	<b>99</b>
4.1 Parametru nustatymas . . . . .	99
4.2 Žvaigždžių spiečių savybės . . . . .	103
4.3 Spiečių masės funkcija . . . . .	103
4.4 Spiečių formavimosi istorija . . . . .	107
4.5 Erdvinis pasiskirstymas . . . . .	109
4.6 Struktūriniai parametrai . . . . .	110
4.7 Apibendrinimas . . . . .	113
<b>Išvados</b>	<b>114</b>
<b>Acknowledgements</b>	<b>115</b>

<b>Gyvenimo aprašymas</b>	<b>116</b>
<b>Curriculum Vitae</b>	<b>117</b>

## List of abbreviations

- AC** – aperture correction  
**ACS** – Advanced Camera for Surveys  
**arcmin, arcsec** – minute of arc, second of arc  
**CFE** – cluster formation efficiency  
**CFR** – cluster formation rate  
**CMD** – colour-magnitude diagram  
**CMF** – cluster mass function  
**CR** – cosmic ray  
**GC** – globular cluster  
**GMC** – giant molecular cloud  
**HLA** – *Hubble* Legacy Archive  
**HST** – *Hubble* Space Telescope  
**IMF** – initial mass function  
**IR** – infrared  
**MIPS** – Multi-Band Imaging Photometer for Spitzer  
**MS** – main sequence  
**MW** – Milky Way galaxy  
**Myr, Gyr** – megayear (a million years), gigayear (a billion years)  
**OLR** – outer Lindblad resonance  
**pc, kpc** – parsec, kiloparsec  
**PDF** – probability distribution function  
**PHAT** – Panchromatic *Hubble* Andromeda Treasury  
**PHAST** – Panchromatic *Hubble* Andromeda Southern Treasury  
**PMS** – post main-sequence stars  
**RGB** – red-giant branch  
**SFR** – star formation rate  
**SLUG** – the Stochastically Lighting Up Galaxies  
**SSP** – single stellar population  
**S/N** – signal-to-noise ratio  
**TCD** – two-colour diagram  
**UV** – ultraviolet  
**WFC3** – Wide Field Camera 3  
**WFPC2** – Wide Field and Planetary Camera 2

# Introduction

## Motivation

Most stars form in star clusters, which are gravitationally bound groups of stars within a closed tidal surface (i.e., the boundary where cluster's gravity is insufficient to retain its stars, allowing them to escape due to external forces), as long as the volume is not dominated by dark matter and contains at least 12 stars (Trumpler 1930; Krause et al. 2020). The first condition separates star clusters from galaxies, the second one from multiple star systems. Therefore, star clusters are widely used in order to understand evolution and formation of the galaxies. Detailed star clusters surveys in the Milky Way (MW) are restricted due to limited volume and interstellar extinction within the Galactic plane, resulting in star cluster samples that are complete only within a small region (radius of  $\sim 2$  kpc, Kharchenko et al. 2013) around the Sun. This limits the variety of objects and galactic environments explored within the MW. To overcome the limitations of incomplete Galactic samples, cluster studies have been extended to other galaxies. A prime target for star cluster studies is Andromeda (M 31), the closest disc galaxy to the Milky Way. Andromeda's proximity allows for the resolution of individual bright stars within clusters and the reliable detection of clusters with luminosities as faint as  $< 10^4 L_\odot$  (Johnson et al. 2012). Additionally, M 31 provides access to a diverse range of environments across the extent of star-forming disc. Observations of spiral arms and star forming regions allow us to determine causes and consequences of star formation processes and their impact on the evolution of stellar population across the galaxy. Star clusters are suitable to solve this problem, as they represent single stellar populations with roughly the same age and metallicity. Also, their properties can be modelled at various evolutionary stages, offering a robust framework for comparison with observational data.

Numerous star cluster observations in M 31 were made by *Hubble* Space Telescope (HST). However, most research concentrates on studying massive globular clusters (GCs), which are in M 31 halo (Barmby et al. 2002, 2007; Caldwell et al. 2009). Detailed studies of star clusters in the disc started with the advent of Panchromatic Hubble Andromeda Treasury (PHAT, Dalcanton et al. 2012) survey, which covers a significant portion of the galaxy's disc in the north-east region, by including dense regions in M 31 centre to the galaxy outskirts. PHAT observations provide the highest quality data for studying star cluster physical parameters – age, mass, metallicity, and interstellar extinction. However, we still encounter age-extinction degeneracies, where a young cluster with extinction could exhibit similar colours to an older object without extinction (de Meulenaer et al. 2013, 2014).

In this thesis, we focus on M 31 disc star clusters. Since the accuracy of physi-

cal parameter determination correlates with observational quality, our first step is to improve the observational results. Integral photometry (Johnson et al. 2012, 2015) to the observed star clusters was applied for PHAT survey data, but bright field stars projected onto the cluster aperture can distort the true cluster colours, significantly affecting the derived physical parameters, which are highly sensitive to colour variations. Beerman et al. (2012) demonstrated that star cluster parameters can be determined with better accuracy when bright, evolved stars are excluded. Thus, in order to get accurate cluster colours, we used adaptive aperture photometry method (Naujalis et al. 2021). This method employs two apertures: a total aperture to measure total cluster flux, and a colour aperture, which measures only central parts of the cluster by excluding bright field stars. This two-aperture approach helps to mitigate contamination and provides more accurate cluster colour measurements. Then, using PHAT survey photometry catalogues (Naujalis et al. 2021; Kriščiūnas et al. 2023), we derived physical parameters – age, mass, and extinction, by using a large grid of stochastic models, and analysed the properties of star clusters within the disc of the M 31 galaxy.

## The objective of the thesis

Study the young star cluster population in the Andromeda galaxy (M 31).

## The main tasks of the thesis

- Perform multicolour aperture photometry of the star clusters in M 31.
- Determine the M 31 star cluster parameters: age, mass, and interstellar extinction.
- Investigate the properties of star cluster population in the M 31 galaxy disc.

## Results and statements to be defended

1. The six-colour aperture photometry of 1477 star clusters in the M 31 galaxy.
2. The parameters of 1922 star clusters in M 31: age, mass, and interstellar extinction.
3. The last major episode of star cluster formation in the present day north-eastern part of the M 31 disc occurred  $\sim(200 \pm 50)$  Myr ago.
4. The star cluster formation in the M 31 16 kpc ring became prominent only recently ( $<40$  Myr).
5. The mass function of the M 31 star clusters is well represented by the truncated Schechter-type function with a characteristic mass  $M_C = (13.3_{-2.6}^{+1.3}) \cdot 10^3 M_\odot$ .

## Publications included in the thesis

1. **Kriščiūnas, E.**, Daugevičius, K., Stonkutė, R., & Vansevičius, V. 2023, A&A, 677, A100
2. Daugevičius, K., **Kriščiūnas, E.**, Cicénas, E., Stonkutė, R., & Vansevičius, V. 2024, A&A, 688, A131
3. Daugevičius, K., Stonkutė, R., **Kriščiūnas, E.**, Cicénas, E., & Vansevičius, V. 2025, A&A, 699, A290
4. **Kriščiūnas, E.**, Stonkutė, R., Daugevičius, K., Cicénas, E., & Vansevičius, V. 2025, A&A, submitted for publication

## Presentations at conferences

1. **Kriščiūnas E.**, Vansevičius V., Star clusters in the Andromeda galaxy, Open Readings 2021, Vilnius, 2021. (poster presentation)

2. **Kriščiūnas E.**, Vansevičius V., Andromedos galaktikos žvaigždžių spiečiai, 44-oji Lietuvos Nacionalinė Fizikos Konferencija, Vilnius, 2021. (poster presentation)
3. **Kriščiūnas E.**, Stonkutė, R., Vansevičius V., HST aperture photometry of the star clusters in M 31, Open Readings 2023, Vilnius, 2023. (oral presentation)
4. **Kriščiūnas E.**, Daugevičius K., Cicėnas E., Stonkutė R., Vansevičius V., Andromedos galaktikos žvaigždžių spiečių sistema, 45-oji Lietuvos Nacionalinė Fizikos Konferencija, Vilnius, 2023. (poster presentation)
5. **Kriščiūnas E.**, Daugevičius K., Cicėnas E., Stonkutė R., Vansevičius V., Star clusters in the disc of Andromeda, MODEST-24: Exploring Dense Stellar Systems Across Cosmic Time, Warsaw, 2024. (poster presentation)
6. **Kriščiūnas E.**, Daugevičius K., Cicėnas E., Stonkutė R., Vansevičius V., Star clusters and spiral arms of the M31 galaxy, Open Readings 2024, Vilnius, 2024. (oral presentation)
7. **Kriščiūnas E.**, Daugevičius K., Cicėnas E., Stonkutė R., Vansevičius V., Star Clusters in the Disc of Andromeda, Bridging scales: star clusters and their host galaxies from the local to the high-z Universe, Matera, 2025. (poster presentation)

## Summer schools

1. IMPRS Summer School Stellar Ecosystems 2021, Heidelberg, Germany, 2021 (online school)
2. COST NanoSpace James Webb Space Telescope (JWST) Training School, San Cristóbal de La Laguna, Spain, 2023
3. IMPRS Summer School Unravelling Galaxy Evolution with JWST 2023, Heidelberg, Germany, 2023

## Contribution of the author

The author determined cluster centre coordinates, aperture sizes, sky background levels, and performed frame cleaning for defects. The author together with co-authors determined star cluster physical parameters (age, mass, and extinction), analysed properties of the star cluster population in M 31, and prepared the catalogues of aperture photometry and cluster parameters.

# Chapter 1

## Andromeda (M 31) galaxy

Andromeda (M 31) is the nearest spiral galaxy in the Local Group, located at a distance of  $\sim 785$  kpc (at this distance,  $1'' = 3.8$  pc; McConnachie et al. 2005; Vansevičius et al. 2009), making it one of the premier laboratories for understanding disc galaxies like our own. Slightly more massive than the Milky Way (Peñarrubia et al. 2016; Hammer et al. 2025), Andromeda has significantly different evolutionary history, shaped by multiple major mergers with smaller galaxies over the past 4 Gyr (Williams et al. 2015; Hammer et al. 2018). These interactions likely played a key role in shaping Andromeda’s structure and star formation activity, including the formation of massive middle-aged star clusters, which are absent in the Milky Way (Vansevičius et al. 2009). Also, intergalactic mergers are known to trigger intense bursts of star formation, contributing to the formation of large star clusters (Di Matteo et al. 2007) and prominent star-forming rings. Unfortunately, the high inclination angle ( $\sim 77.5^\circ$ , van der Marel et al. 2019) makes it difficult to determine the large-scale structure of M 31, and there is no clear consensus regarding the organization of spiral structure in this important galaxy (see Table 1.1 for M 31 parameters). One of the key structures of M 31 galaxy is the well-known 10 kpc star-forming ring, which has been observed in previous studies (Gordon et al. 2006; Kang et al. 2012; Lewis et al. 2015; De Somma et al. 2025). Additionally, the presence of a second, inner dust ring with an offset of  $\sim 0.5$  kpc from the galaxy’s nucleus, has also been identified (Block et al. 2006). The presence of two off-centre circular rings suggests that the disc of M 31 has been distorted by a very recent passage of its satellite galaxy through the disc (i.e., a head-on collision with the satellite galaxy about a few tens or hundred Myrs ago, Gordon et al. 2006; Block et al. 2006; Dierickx et al. 2014), supporting the hypothesis of multiple mergers. Such a recent event may have enhanced the efficiency of star formation in the disc of M 31 galaxy (Yin et al. 2009).

Star cluster systems in M 31 are fundamental probes of galaxy evolution and assembly, in the sense that significant star cluster formation is typically produced by major star-forming episodes in the galaxy (Larsen & Richtler 2000; Brodie & Strader 2006). Star clusters are commonly classified into two main types: massive globular clusters and younger open star clusters (hereinafter disc star cluster). In contrast, groups of stars that are not gravitationally bound are called stellar associations (Blaauw 1964; Gieles & Portegies Zwart 2011; Adamo et al. 2020). Globular clusters are generally old ( $> 1$  Gyr), massive ( $\geq 10^4 M_\odot$ ), and trace the halo and formation histories of galaxies (Kruijssen et al. 2019). Disc star clusters are generally young

( $\leq 1$  Gyr), have low mass ( $\leq 10^5 M_{\odot}$ ), and trace the quantity and characteristics of on-going recent star formation. Historically, the distinction between the two cluster types closely aligns with a fundamental difference in photometric and chemical abundance patterns. Disc clusters are mostly single population clusters with a single main sequence in the colour-magnitude diagram (CMD). In comparison, nearly all globular clusters have multiple main sequences and significant star-to-star variations in light element abundances, i.e., multiple stellar populations. Therefore, a more practical classification of star clusters is based on their stellar populations, distinguishing between single-population and multiple-population clusters (Carretta et al. 2010; Bastian & Lardo 2018). Moreover, this classification into two types has also historically persisted because such distinction is clearly seen in the MW. However, recent studies have shown that this clear separation does not necessarily hold in other galaxies, where massive and young clusters have been observed, including in M 31.

**Table 1.1.** Parameters of the M 31 galaxy.

Parameter	Value	Reference
<i>Hubble</i> type	SA(s)b	Jarrett et al. (2003)
$\alpha(J2000); \delta(J2000)$	$00^{\text{h}} 42^{\text{m}} 44.3^{\text{s}}$ ; $+41^{\circ} 16' 9''$	McConnachie et al. (2005)
P.A.	$37.7^{\circ}$	Chemin et al. (2009)
Incl.	$77.5^{\circ}$	van der Marel et al. (2019)
Distance	$785 \pm 25$ kpc	McConnachie et al. (2005)
$(m - M)_0$	$24.47 \pm 0.07$ mag	McConnachie et al. (2005)
$E(B - V)$	0.06 mag	McConnachie et al. (2005)
$V_{rot}$	$\sim 250$ km/s	Chemin et al. (2009)
Dynamical mass	$4.5 \cdot 10^{11} M_{\odot}$	Hammer et al. (2025)

$\alpha(J2000)$  and  $\delta(J2000)$  – equatorial coordinates of the galaxy centre; P.A. – position angle of the major axis; Incl. – inclination angle;  $(m - M)_0$  – distance modulus;  $E(B - V)$  – interstellar extinction along the line of sight;  $V_{rot}$  – rotational velocity at a distance of 10 kpc from the centre of M 31.

In the past two decades most studies of M 31 galaxy concentrated on globular clusters (Racine 1980; Barmby et al. 2000, 2002; Puzia et al. 2005), as they are relatively bright, composed of stars that are strongly concentrated toward the centre, and mostly distributed in the galaxy’s halo, away from the dense disc, which makes them easier to detect. The high luminosity of GCs allows for the use of spectroscopy to determine their age and chemical composition. More than 400 GCs are known in M 31 (Caldwell & Romanowsky 2016), which is about three times more than in MW. Beasley et al. (2004); Puzia et al. (2005); Caldwell et al. (2009, 2011) demonstrated that M 31 contains not only old ( $\sim 10$  Gyr) but also intermediate ( $\sim 7$  Gyr) and young ( $\sim 1$  Gyr) high-mass ( $10^4 M_{\odot}$ ) clusters that have strong concentration toward the centre, resembling GCs of the Milky Way. Their metallicities in M 31 range from  $[Z/H] = -2.0$  (100 times lower than the Sun’s metallicity) to solar metallicity, with the youngest GCs having the highest metallicities. Thus, the GC system in M 31 consists of two subpopulations: one is a metal-rich and spatially concentrated, while the other is metal-poor and spatially extended (Kang et al. 2012).

## 1.1 Star clusters in the disc of Andromeda

In this thesis, we mainly focus on star clusters located in the galactic disc. These clusters typically form in the densest cores of giant molecular clouds (GMCs), where accreting gas is converted into stars until feedback disperses the remaining material (Krumholz et al. 2019). This effect is quantified as the cluster formation efficiency (CFE), which represents the fraction of stellar mass formed in long-lived star clusters (Adamo & Bastian 2015; Renaud 2018). CFE depends on the scale over which it is measured and varies from a few percent in galaxies with low star formation intensity up to  $\sim$ 50% in intense starburst events, such as galaxy mergers. Johnson et al. (2016) demonstrated that the CFE in the M 31 galaxy ranges between 4-8%. This result indicates that less than 10% of the initial cluster mass remains gravitationally bound after 10 Myr, a period known as the infant mortality limit (Lada & Lada 2003). This term describes the effect that gas expulsion has on concentrations of young embedded stars. The rapid removal of gas significantly alters the potential felt by the stars and can result in the destruction of the cluster (Smith et al. 2013). Clusters that survive gas removal from the system can remain in the galactic disc for several hundred million years or even longer. Nevertheless, when star clusters form, they continue to lose part of their mass. In the first  $\sim$ 100 Myr after gas removal, clusters disperse through a combination of mass loss and tidal shocks by dense molecular structures in the star-forming environment. Mass loss could be caused due to stellar evolution and relaxation (Gieles et al. 2011). At young ages ( $<40$  Myr), stellar populations eject  $\sim$ 20% of their mass in supernovae, releasing high-speed gas that almost certainly escapes the parent cluster. After 40 Myr, mass loss is dominated by asymptotic giant branch stars, which shed their envelopes through slow stellar winds (Krumholz et al. 2019). After  $\sim$ 100 Myr, clusters lose their mass via two-body relaxation and tidal interactions with massive objects such as GMCs (Spitzer 1958; Gieles et al. 2006; Binney & Tremaine 2008), processes that preferentially affect low-mass clusters.

### 1.1.1 Overview of previous surveys

The first mention of an "open star cluster" in M 31 appears in Hubble's pioneering paper that provided his evidence that M 31 is an extragalactic object (Hubble 1929). He suggested that a group of stars catalogued as NGC 206, located in the south-western region of M 31, had similar properties to an open clusters in our galaxy. However, it is now understood that while NGC 206 contains bright, young stars typical of open clusters, its extensive size (over 1200 pc) aligns more closely with very large stellar associations (van den Bergh 1964). Later, Hodge (1979) conducted a survey for disc clusters using the Kitt Peak National Observatory 4-m telescope, covering the entire M 31 disc. The survey resulted in the catalogue of 403 candidate disc star clusters, which were primarily young objects, as they were resolved on the photographic plates. However, analysis of HST images revealed that the sample was contaminated, including objects such as small OB associations and asterisms (Williams & Hodge 2001a). An asterism is a pattern of stars that appear grouped together in the sky but are not necessarily gravitationally bound, unlike true star clusters. A later study by Hodge et al. (1987), using three-colour charge-coupled device photometry of a selection of the catalogued clusters, confirmed that these clusters are very young. More recently, Williams & Hodge (2001b) used HST WFPC2 images to obtain CMDs for four young populous clusters, often referred to as "blue globular" clusters. Their analysis revealed

these clusters have ages between 60 and 150 Myr, distinguishing them from traditional GCs in the Milky Way, which are significantly older. This result differs from earlier studies (e.g., Vetešnik 1962; van den Bergh 1967), which classified these clusters as globular based on their colour measurements.

In the past two decades, large catalogues of star clusters in M 31 have been published (e.g., Barmby et al. 2000; Galleti et al. 2004; Kim et al. 2007; Caldwell et al. 2009, 2011). Barmby et al. (2000) presented UBVR<sub>I</sub> and JHK photometry of 435 clusters and cluster candidates. However, only for 268 objects optical photometry in four or more bands is available, and 224 have infrared photometry. Galleti et al. (2004) identified 693 known and candidate globular clusters in M 31 using the 2 Micron All Sky Survey database, and presented the Revised Bologna Catalogue. Kim et al. (2007) carried out wide field observations and found 113 new star clusters and 258 probable objects that could be classified as star clusters. Caldwell et al. (2009) published a new catalogue of 670 likely star clusters, with accurate coordinates from the Local Group Galaxy Survey and the Digitized Sky Survey data. Despite these efforts, creating a complete, deep, and homogeneous catalogue of disc star clusters in M 31 proved to be challenging. Detecting relatively faint star clusters, which project onto the bright disc structure or the bulge, was difficult. As a result, most of the star cluster research concentrated on GCs, since they are massive and bright, making them easier to observe in the M 31 halo. More detailed disc star cluster surveys started with the advent of HST (Williams & Hodge 2001b,a). However, cluster samples were not big enough (Barmby et al. 2009; Perina et al. 2010) or homogeneous (Krienke & Hodge 2007a, 2008; Hodge et al. 2009) in order to make conclusions about M 31 disc evolution or formation. The first homogeneous star cluster survey was conducted in the south-western part of M 31 (Kodaira et al. 2004; Narbutis et al. 2008; Vansevičius et al. 2009). Using Subaru flagship telescope 238 star clusters were identified in the disc of M 31 galaxy. A few years later, the PHAT survey (Dalcanton et al. 2012) followed and expanded disc star cluster sample by ~10 times in the north-eastern part of M 31. Recently, the Panchromatic Hubble Andromeda Southern Treasury (PHAST) survey (Chen et al. 2025), contiguous to PHAT, was performed down to the southern half of M 31, further expanding star cluster studies. Therefore, the biggest challenge in studying cluster formation and evolution lies in the complexity of observations and measurements, as well as the limited sample sizes, which often include only high-mass clusters (Krumholz et al. 2019).

### 1.1.2 Observation methods

In order to study star cluster evolution, it is crucial to determine their physical parameters. They can be calculated using two main methodologies: spectroscopy and photometry. With spectroscopy we compare observed spectra with models or other known spectra, often focusing on spectral line indices – quantitative measurements of the strength of specific absorption features – which are sensitive to variations in stellar population age and metallicity (Vazdekis et al. 2010). The advantage of spectroscopy lies in its ability to target specific spectral regions that provide the most detailed information. However, in order to perform spectroscopic observations we need bright objects with high signal-to-noise ratio (S/N). Also, dense stellar regions pose a challenge as background and foreground stars could affect our results.

In contrast, photometry is used to estimate the age, mass and extinction of a cluster

by comparing the observed cluster luminosity and colours to single stellar population (SSP) models (where all stars have the same age and metallicity within some small tolerance) or stochastic models. By using traditional SSP models, an implicit assumption is made that the initial mass function (IMF) of stars within the cluster is fully sampled. However, this is only strictly valid for the most massive clusters  $>10^5$  M<sub>⦿</sub>. For lower mass objects, stochastic sampling of the IMF can give inaccurate estimates of age, mass, and extinction (Daugevičius et al. 2024). Thus, for disc cluster parameter derivation it is more convenient to use stochastic models, which account for star stochasticity. Furthermore, photometry also has the advantage of collecting more light from the object, allowing the study of dimmer and more distant clusters compared to spectroscopy. The images obtained during photometric observations are used to identify star clusters and analyse their structure. In order to improve results, we have to examine star clusters across different passbands, from ultraviolet (UV) to infrared (IR) wavelengths. However, interstellar extinction can significantly affect the results, as shorter UV wavelengths are absorbed or scattered by dust and gas particles.

### 1.1.3 Derivation of cluster parameters: overview of the methods

Star cluster parameters can be derived using various methods and algorithms. The most accurate approaches involve constructing colour-magnitude diagrams for clusters based on photometric measurements of individual stars and then comparing them with synthetic CMDs generated from stellar population models or fitting theoretical isochrones directly to the observed CMDs (Johnson et al. 2016; Wainer et al. 2022; Čeponis et al. 2024). However, those methods rely on resolving individual upper main-sequence (MS) stars and on detecting stars below the MS turn-off point with sufficient accuracy. As a result, accurate and robust parameter estimates can be achieved only for nearby, young star clusters, significantly limiting the number of objects that can be studied using CMDs. Wainer et al. (2022) demonstrated that parameter estimates using CMDs are good up to 300 Myr and for clusters more massive than 1000 M<sub>⦿</sub>. Integral cluster spectroscopy methods (Caldwell et al. 2009, 2011; Caldwell & Romanowsky 2016) are also suitable for deriving accurate cluster parameter; however, only relatively massive clusters in M 31 can be studied with this approach.

Other group of methods fit stochastic theoretical stellar population models to the observed integrated cluster magnitudes and colour indices (Deveikis et al. 2008; Fouesneau & Lançon 2010; de Meulenaer et al. 2013; Fouesneau et al. 2014; Krumholz et al. 2015). These techniques enable the study of lower-mass, older, and more distant star clusters, significantly expanding the number of objects that can be investigated. Also, the study of unresolved star clusters could be mimicked using ground based observations of M 31 clusters (Kodaira et al. 2004; Narbutis et al. 2008; Bridžius et al. 2008). This approach enables the study of star formation histories in galactic disc across a broader range of star cluster masses and over extended timescales. However, the accuracy of derived star cluster parameters using such methods is highly sensitive to uncertainties in aperture photometry (Narbutis et al. 2007) and the proper accounting for projected background and foreground stars (hereinafter referred to as field stars), as well as the brightest evolved cluster members (Beerman et al. 2012; Daugevičius et al. 2024). This is especially critical for low-mass clusters ( $<3000$  M<sub>⦿</sub>), where integrated photometry methods are highly sensitive to stochastic effects, particularly the random sampling of the stellar initial mass function (Fouesneau & Lançon 2010;

Beerman et al. 2012; de Meulenaer et al. 2013, 2017).

For low-mass clusters ( $<10^4 M_{\odot}$ ), photometric variability is driven by stars that have left the MS and already are in transient late-evolutionary phases. These phases are sparsely populated, leading to significant fluctuations in the observed brightness and colour of the cluster. Beerman et al. (2012) studied the effect of bright post main-sequence stars (PMS) on the accuracy of star cluster parameters derived using the integrated photometry method. They showed that excluding these bright, resolved PMS members from aperture photometry, and focusing on the unresolved light component, improves the precision of age and mass estimates. Additionally, de Meulenaer et al. (2017) highlighted that the presence of bright field stars significantly affects the accuracy of cluster parameter derivation. It was shown that in cases when bright field stars (that are mostly red) reside within the aperture used for the photometry of star cluster, strong age-extinction degeneracies are introduced. Therefore, in order to tackle these problems arising due to bright field stars, we use adaptive aperture photometry method presented in Chapter 3.

# Chapter 2

## Observational data

### 2.1 PHAT survey

The recent progress in understanding star clusters in galaxies outside our own has been driven by the comprehensive Panchromatic *Hubble* Andromeda Treasury Program (PHAT; Dalcanton et al. 2012), the Panchromatic *Hubble* Andromeda Treasury: Triangulum Extended Region (PHATTER; Williams et al. 2021), and the Panchromatic *Hubble* Andromeda Southern Treasury (PHAST; Chen et al. 2025) surveys, performed with the *Hubble* Space Telescope. Stellar and cluster populations of M 31 galaxy disc is well-represented by published photometry results for a large sample (2753 objects, Johnson et al. 2015) of star clusters that reside in diverse environments: from extremely crowded central parts of the galaxy to rather sparse outskirts.

Our research is based on the HST PHAT survey data obtained from the *Hubble* Legacy Archive (HLA)<sup>1</sup>. We used the so-called "Level 2" products that have been processed by the automated HLA pipeline (with bias and dark frames subtracted, flat fielding applied, and all available exposures combined). PHAT observations are segmented into 23 sub-areas known as "bricks" (Fig. 2.1), with numbering increasing from the galaxy centre outwards. Each brick is composed of 18 different frames taken by HST, arranged in a rectangular grid of 6 by 3, covering approximately a  $12' \times 6.5'$  portion of the sky. Star cluster dataset is made of six passbands from three different HST channels: the  $F475W$  and  $F814W$  passbands are from the Advanced Camera for Surveys (ACS/WFC); the  $F275W$ ,  $F336W$  and  $F110W$ ,  $F160W$  passbands are from the Wide Field Camera 3 UVIS (WFC3/UVIS) and Wide Field Camera 3 IR (WFC3/IR) channels, respectively. Various passbands have different number of exposures: the  $F475W$  frames are combined from five exposures, the  $F814W$  and  $F160W$  frames – from four exposures, the  $F275W$  and  $F336W$  frames – from two exposures, and the  $F110W$  frame is produced from a single exposure. The resulting total exposure times are 1935 s in  $F275W$ , 2600 s in  $F336W$ , 3620 s in  $F475W$ , 3235 s in  $F814W$ , 1498 s in  $F110W$ , and 3292 s in  $F160W$  (Dalcanton et al. 2012). The spatial alignment of the images was carried out by Naujalis et al. (2021).

---

<sup>1</sup><https://hla.stsci.edu>

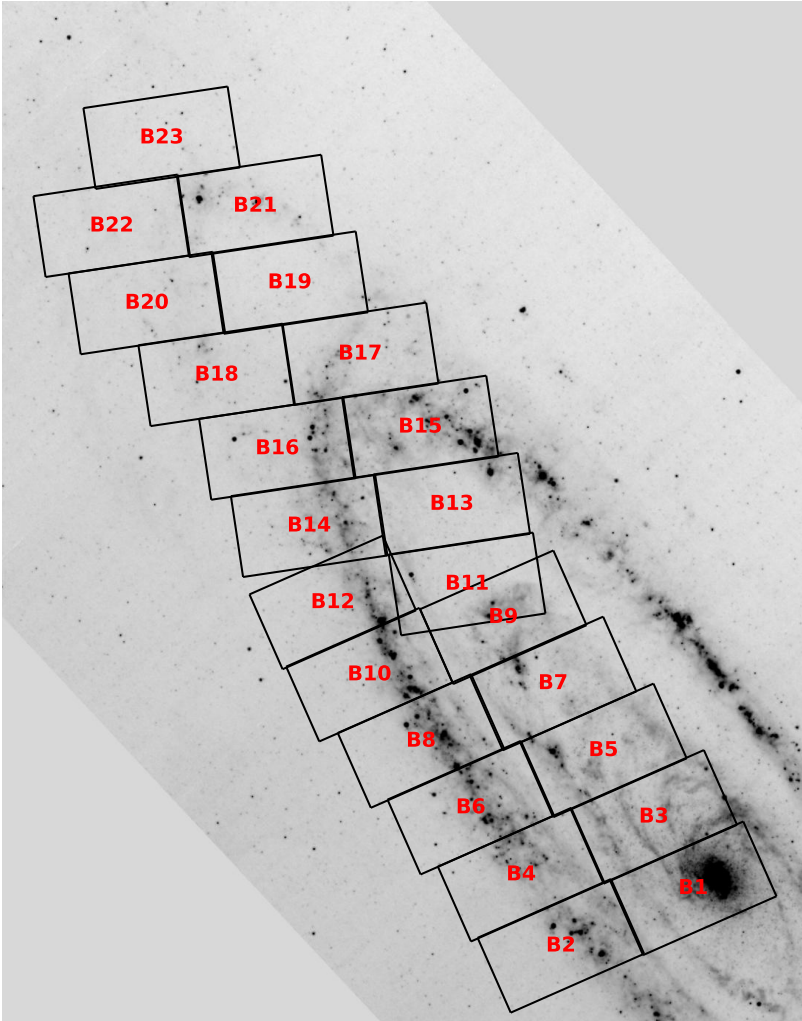


**Figure 2.1.** Multi-Band Imaging Photometer for Spitzer (Spitzer/MIPS) 70  $\mu\text{m}$  M 31 map. Black contours show 23 bricks from PHAT survey. North is up, east is left.

## 2.2 Cluster sample

In the M 31 PHAT fundamental star cluster catalogue published by Johnson et al. (2015) there are 2753 objects. Using PHAT survey data Naujalis et al. (2021) measured 1181 star clusters by applying the adaptive aperture method; therefore, our aim was to analyse the remaining objects ( $N = 1572$ ) in order to have a comprehensive catalogue, where adaptive aperture photometry method is applied. We visually inspected each object using colour images constructed from the following passbands:  $F275W+F336W+F475W$ ;  $F336W+F475W+F814W$ ;  $F475W+F110W+F160W$ ; and looking into individual grey-scale frames (Fig. 2.2). The selected passband combinations were chosen to maximize sensitivity to various stellar populations. The com-

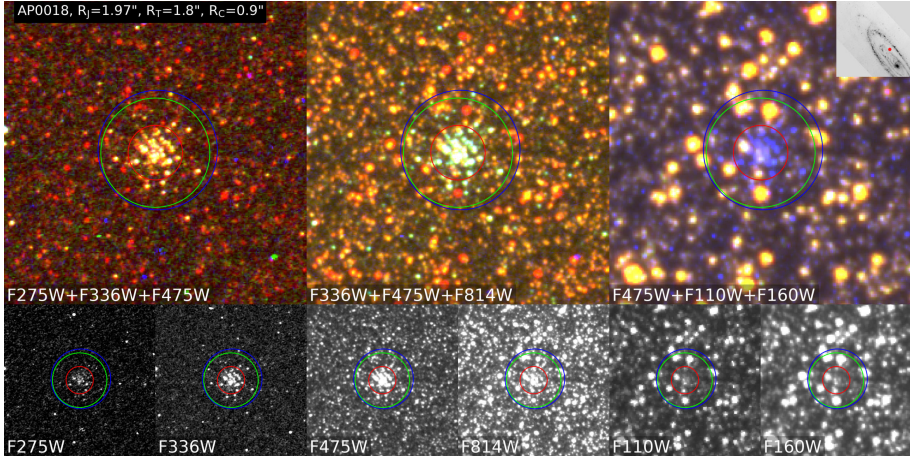


**Figure 2.2.** Images of the cluster AP0018 in colour panels (top), produced by combining three passbands, and grey-scale panels (bottom), produced from individual passband frames (the passbands are labelled inside the panels). Blue, green, and red circles mark Johnson et al. (2015), T, and C apertures, respectively. The size of each panel is  $10'' \times 10''$ . An insert at the top-right corner indicates the location of the cluster in M 31. North is up, and east is to the left.

bination of  $F275W$ ,  $F336W$ , and  $F475W$  is sensitive to young stars, including those on the MS, which are crucial for identifying young star clusters. In addition, this combination helps to distinguish cosmic ray (CR) artefacts. The  $F336W$ ,  $F475W$ , and  $F814W$  combination targets stars in both blue and red regions of the spectrum, making it effective for identifying intermediate-age clusters and their stellar populations. Finally, the  $F475W$ ,  $F110W$ , and  $F160W$  combination helps to distinguish bright field stars from cluster members, with the  $F475W$  passband assisting in identifying the cluster centre by resolving regions of higher stellar density.

We discarded from further analysis 90 objects, which have frames only in the  $F475W$  and the  $F814W$  passbands. The objects AP1848 and AP2446 were abandoned since they are contaminated by background galaxies. The objects AP1588, AP1661, and AP2687 were also omitted, as they resemble reflections of bright stars or emission nebulae. The frames of the objects AP3630, AP4034, and AP4132 have irreparable empty pixel defects in the  $F475W$  passband; therefore, we discarded them. Moreover, three clusters – AP0239, AP1782, and AP3306 – seem to be double objects (see Fig. A1 in the Appendix); therefore, we separated them into two parts. In the published catalogues the second components are marked: AP60239, AP61782, and AP63306 respectively. We use the names of clusters in the format that they are introduced in Johnson et al. (2015). Then we examined all possible frames in the  $F275W$ ,  $F336W$  and  $F110W$ ,  $F160W$  passbands, where we selected frames with the highest S/N ratio and the lowest number of CR artefacts. For 11 objects the  $F110W$ ,  $F160W$  passband frames were changed, because they had no available signal; for 64 objects we changed the  $F275W$ ,  $F336W$  passband frames, since new ones have better S/N ratio or less CR artefacts.

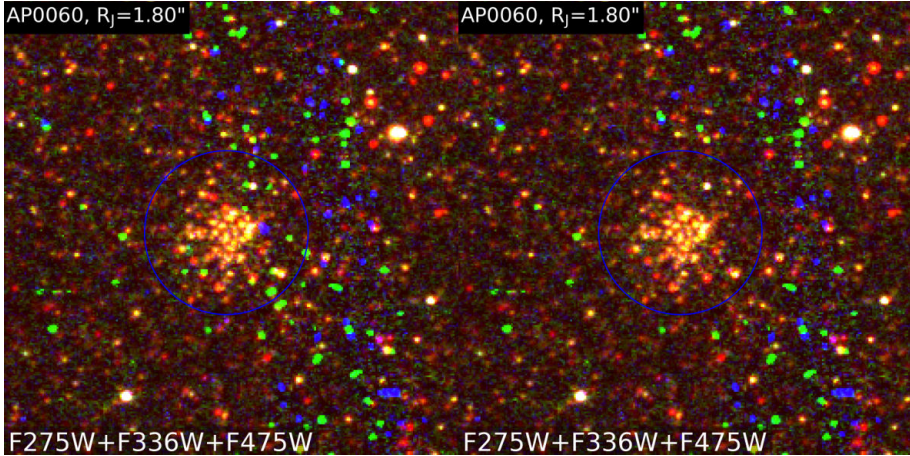


**Figure 2.3.** Images of the cluster AP0060 made from a combination of  $F275W+F336W+F475W$  passbands. Left: the uncleaned  $F275W$  and  $F336W$  passbands are shown with a significant number of cosmic ray artefacts (bright green and blue objects). Right: the same image after artefact removal.

### 2.2.1 Cleaning of defects

The frames of the  $F275W$  and  $F336W$  passbands contain larger numbers of CR artefacts since they are composed only from two exposures available, which makes it difficult to reliably clean them in an automated way. Cosmic rays are high-energy particles that transfer energy to detector pixels upon impact, creating signals that mimic external light sources. Thus, CR artefacts can appear similar to stellar objects. In order to remove CRs, we used the `imedit` task from `IRAF`<sup>2</sup> software (Tody 1986). This function replaces image pixels affected by CR defects with interpolated values from the nearest background column or row. As a result, `imedit` enabled us to carefully remove defects manually, that fall inside or close to object apertures defined in Johnson et al. (2015). There are some clusters residing within the gap between two WFC3/UVIS sensors. Within these gaps, there is a significantly larger number of CRs and higher noise due to only a single exposure being available at that location. Therefore, UV measurements were discarded where the gap area overlaps with star clusters. In the composite  $F275W+F336W+F475W$  image (Fig. 2.3), CRs appear as green and/or blue spots that do not have counterparts in other filters. The size of these spots can range from a few pixels to several dozen. It is worth noting that in some cases, CRs can overlap with stars, making them difficult to remove. Fortunately, these instances can be identified in the growth curves and the passbands used for photometry can be excluded. An example of CR artefact removal is shown in Fig. 2.3, where on the left side the cluster is covered by a large amount of CRs, while on the right side, CRs have been cleaned in the vicinity of cluster's aperture. Even though the obvious artefacts were removed during visual inspection, in some cases, unrecognized CRs could remain.

In some frames, pixels with zero values were present. This is an important issue, especially for the  $F110W$  passband, in which there is only one exposure available for

---

<sup>2</sup><https://iraf-community.github.io>

each field. We assigned an interpolated value for these pixels – an average out of eight surrounding non-zero-valued pixels. However, in cases when at least one uncorrected pixel inside the aperture remained after this procedure, we abandoned measurements in this passband.

In the final sample, we measured 1477 star clusters. In Fig. 2.4, locations of the objects analysed in this work are compared to the distribution of the 1181 clusters from Naujalis et al. (2021). Our sample includes the central areas covered by the PHAT survey.

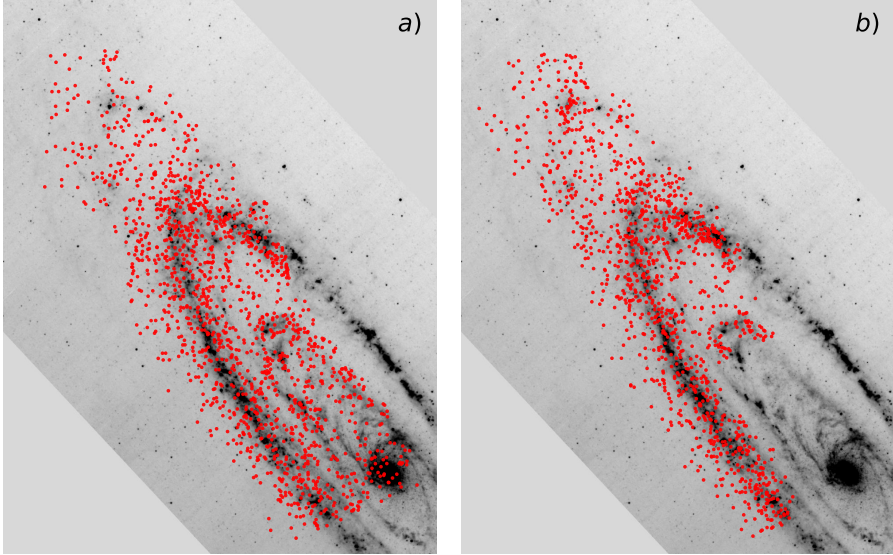


**Figure 2.4.** Locations of star clusters overlaid on the Multi-Band Imaging Photometer for Spitzer (Spitzer/MIPS) 70  $\mu\text{m}$  M 31 map: (a) 1477 clusters measured in this study; (b) 1181 clusters presented in Naujalis et al. (2021).

## 2.2.2 Centre coordinates

Additionally, using DS9 software (Joye & Mandel 2003) and based on the  $F336W$ ,  $F475W$ , and  $F814W$  passband frames, we interactively adjusted the centre coordinates of 1331 clusters. These passbands were selected since they are less affected by field stars, allowing for clearer identification of star cluster centres. In the majority of cases, coordinates were changed only slightly by a few pixels, except for stellar associations, where we selected mostly the cluster-like parts. An example of different centre coordinates is shown in Fig. 2.2, where the apertures defined by Johnson et al. (2015) and those used in our study have different central positions.

# Chapter 3

## Multicolour aperture photometry

Naujalis et al. (2021) introduced an adaptive aperture photometry method to address the challenges in deriving star cluster parameters, arising due to the effects of bright field stars and evolved bright cluster members, which were noticed by Beerman et al. (2012) and de Meulenaer et al. (2017), respectively. In this thesis, we follow the same prescription for performing aperture photometry. We used circular apertures from `photutils`<sup>1</sup> package. The exact measurement method was selected to account for partial pixel coverage. For each cluster we produced the magnitude growth curves in all six passbands in steps of  $0''.01$  up to two times the aperture radius of a cluster. For clusters with smaller apertures, a minimum radius of  $5''$  was applied to ensure sufficient sky background coverage. Photometric zero points for the ACS camera were taken from the ACS Zero Point Calculator<sup>2</sup>, while the ones for both WFC3 channels are taken from the Space Telescope Science Institute (STScI) website<sup>3</sup>. The zero points are listed in Table 3.1, which are used to convert the obtained instrumental magnitudes into a standard system.

A set of figures, shown in Figs. 2.2 and 3.1 for guidance, were produced for each cluster under consideration and used for the analysis. In Fig. 2.2, the green circle indicates the aperture used to measure "total" (T) fluxes and magnitudes, while the red circle shows the smaller aperture used to measure central parts of star clusters and applying an aperture correction, based on the  $F475W$  passband measurements, to other passbands – "colour" (C) fluxes and magnitudes. By selecting C apertures, we avoid the majority of bright field stars and ensure consistent colour indices for star clusters in our sample. For details on the aperture selection criteria, refer to Section 3.2. We stress that adaptive aperture photometry is reliable only for clusters without strong colour gradients beyond the clusters' half-light radii, which could arise due to gradual variations in cluster stellar populations. These variations may appear due to various factors, such as mass segregation of stars or real gradients in stellar populations within some clusters.

---

<sup>1</sup><https://zenodo.org/records/14889440>

<sup>2</sup><https://www.stsci.edu/hst/instrumentation/acs/data-analysis/zeropoints>

<sup>3</sup><https://www.stsci.edu/hst/instrumentation/wfc3/data-analysis/photometric-calibration>

**Table 3.1.** Photometric Zero Points.

<i>F275W</i>	<i>F336W</i>	<i>F475W</i>	<i>F814W</i>	<i>F110W</i>	<i>F160W</i>
22.67	23.52	26.15	25.52	26.06	24.70

Figure 3.1 shows measured growth curves (top) and differential flux profiles (bottom) in each passband. Vertical red and green lines mark  $R_C$  and  $R_T$  aperture radii, respectively. Green horizontal lines indicate magnitudes derived from T fluxes. Negative values in the differential profile indicate that the fluxes in those areas are, on average, lower than the subtracted sky background level. Various positive peaks show the presence of resolved, bright stars and demonstrate the complexity of the surrounding sky backgrounds.

The diverse appearances of star clusters and their surrounding sky backgrounds make it challenging to distinguish individual stars that are part of the cluster from those that are field objects. However, in the majority of cases, by using the multi-colour star cluster images (Fig. 2.2) together with cluster profiles (Fig. 3.1) we determined optimal radii for the  $R_C$  and  $R_T$  apertures.

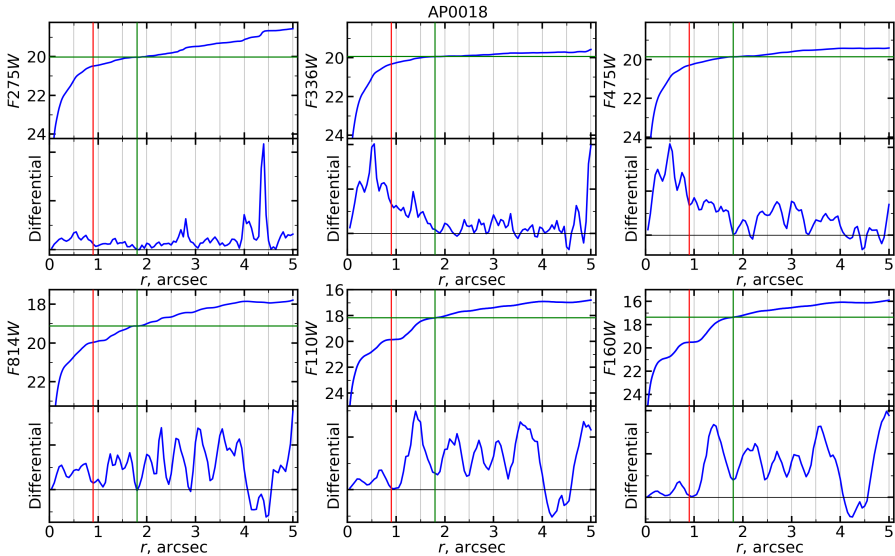


**Figure 3.1.** Growth curves (top, in magnitudes) and differential flux profiles (bottom, in arbitrary units) for the cluster AP0018. Vertical red and green lines show  $R_C$  and  $R_T$  aperture radii, respectively. The green horizontal line indicates the magnitude derived from T fluxes.

### 3.1 Sky background

Sky backgrounds consist of unresolved stellar and galaxy components, as well as the Milky Way and M 31 stars projected in the field of view. Therefore, sky backgrounds

are unpredictable and their correct determination is the main problem when applying star cluster aperture photometry methods in the case of disc galaxies. Sky background areas around clusters usually contain a small number of well-resolved bright stars, which are irregularly distributed, making it challenging to determine background levels across different passbands. Also, flux measurements in various passbands are often dominated by stars with significantly different colours (Fig. 2.2). Since most bright field stars in M 31 are red giants, they mostly impact the IR passbands, complicating cluster parameter derivation by mimicking the effects of extinction and/or older ages (de Meulenaer et al. 2017). The influence of IR-bright field stars varies significantly with distance from the M 31 centre and especially dominates in the *F110W* and *F160W* passbands.

Various automated methods have been proposed to determine background levels (Barmby & Huchra 2001; Krienke & Hodge 2007b; Johnson et al. 2012). However, their reliability is rather low in extremely dense regions such as the M 31 disc. Since automatic methods give inconsistent background level results among various passbands, we plotted growth and differential flux profiles in all passbands (Fig. 3.1) for each cluster and derived consistent sky background levels interactively. The main goal of the interactive procedure is to accurately determine the values of unresolved sky background and to estimate the impact of bright resolved field stars. Differential growth curve profiles (bottom panels in Fig. 3.1) show fluctuations caused by individual stars and were crucial in our decision-making process. We paid special attention to accurately account for bright field stars (especially in the IR passbands), as well as addressing abundant image defects and CR artefacts that dominate in the UV passbands (Naujalis et al. 2021).

Initially, we calculated the mean and median sky background values within ring-shaped regions spanning from  $1.2R_T$  to  $3.4R_T$ , where  $R_T$  is the radius of the cluster's T aperture. These values were used to plot the initial iteration of star cluster growth curves and differential flux profiles. Then the sky background levels were adjusted interactively for each passband to flatten growth curves and bring differential flux profiles close to zero within the sky background determination region.

By combining visual analysis of cluster images with their growth curves and differential flux profiles, we achieved accurate and consistent sky backgrounds across all six passbands, where estimated background levels are compatible across filters. However, this method has two major disadvantages – it is a highly time-consuming process and it may introduce systematic errors if background has a very complex structure.

## 3.2 Apertures

The high density of luminous field stars increases the likelihood of them projecting onto the cluster's aperture. To minimize the impact of resolved field stars on aperture photometry measurements, we used two co-centred apertures. The main criterion for selecting radii of the T apertures is to avoid splitting into parts the bright star images in the *F336W*, *F475W*, and *F814W* passbands; the main criterion for selecting radii of the C apertures is to avoid the brightest field and evolved bright cluster members inside of it (Fig. 2.2). It is expected that C magnitudes should provide more consistent cluster colour indices (less contaminated by bright stars), which are critical in determining star cluster physical parameters from integrated photometry results (de Meulenaer et al. 2017).

We measured the T magnitudes by applying apertures, the radii of which for the majority of objects (~80%) vary in the range of  $\pm 0''.25$  compared with the ones used by Johnson et al. (2015). In total, we decreased the apertures of 687 clusters and increased the apertures of 733 clusters (Fig. 3.2). The radii of apertures we selected range from  $\sim 1''$  ( $\sim 3.8$  pc) for compact star clusters to  $\sim 4''$  ( $\sim 15.2$  pc) for globular-like clusters and stellar associations. The magnitudes of all star clusters in our sample are measured in at least four passbands (including  $F336W$ ,  $F475W$ , and  $F814W$ ).

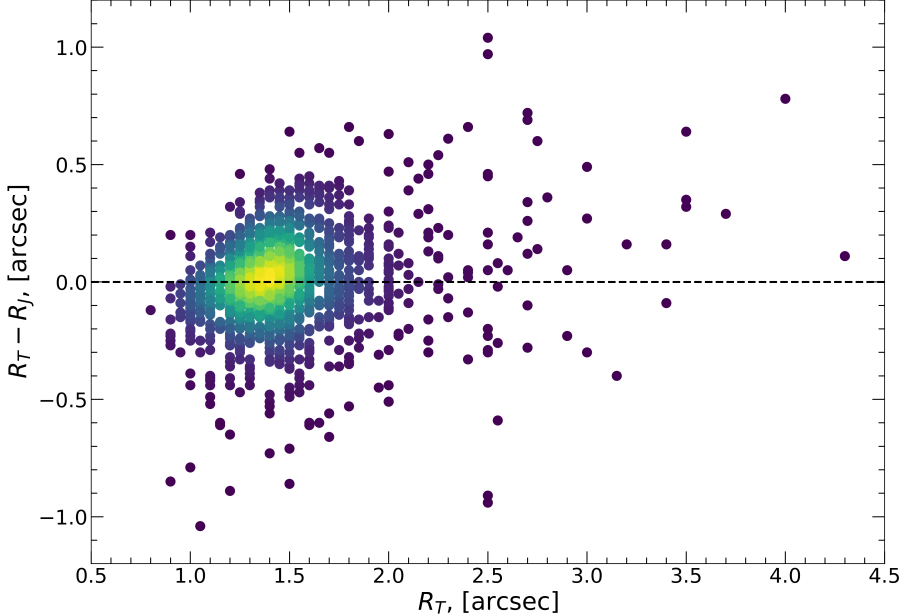


**Figure 3.2.** Differences in aperture sizes used in this study ( $R_T$ ) and in Johnson et al. (2015) ( $R_J$ ). The colours of dots indicate the local point density.

The colour-consistent cluster C magnitudes in all passbands were derived by applying aperture corrections (ACs,  $F475W_{AC}$ ), which are necessary because the C aperture is smaller compared to the T aperture, resulting in less flux being captured. Therefore, to account for the missing flux, we used the difference between magnitudes derived from the fluxes measured through T and C apertures for the  $F475W$  passband:  $F475W_{AC} = F475W_T - F475W_C$ . The  $F475W$  passband was chosen as a base to calculate colour-consistent magnitudes. Observations in the  $F475W$  passband have higher S/N ratio compared to the  $F336W$ ,  $F814W$  passbands, and are less contaminated by the light of resolved field stars from old M 31 populations. The final C magnitudes are  $F?W = F?W_C + F475W_{AC}$ , where the "?" marks the HST three-digit passband code and  $F?W_C$  are the magnitudes measured through the C aperture. We want to stress that in some complicated cases the accuracy of photometry results can be underestimated. However, in most cases, the adaptive aperture photometry provides colour-consistent cluster magnitudes that fit well with the models.

We use cluster AP0018 (Figs. 2.2 and 3.1) as an example to demonstrate how we selected the appropriate aperture sizes. The cluster has a dense core that appears bright in the  $F336W+F475W+F814W$  passband combination, allowing us to distinguish it

from the surrounding field stars. Within the cluster, a few bright IR stars dominate the light in the  $F110W$  and  $F160W$  passbands. These stars could be evolved cluster members or projected field stars. To assess whether a star belongs to the cluster, we examine the background stars around the object. Since these bright stars have colours similar to those of field stars and are also visible in the differential profiles across the  $F814W$ ,  $F110W$ , and  $F160W$  passbands (Fig. 3.1), we excluded them by selecting a smaller C aperture. The main criterion for selecting the T aperture was to avoid splitting bright stars at the edge of the aperture. Measured T magnitudes of cluster AP0018 in all passbands are shown in Fig. 3.1 by the horizontal green lines. The green and red vertical lines represent the sizes of the T and C apertures, respectively.

### 3.3 Photometric uncertainties

In order to estimate photometric uncertainties, we considered two main sources that contribute to the errors of cluster magnitudes. The first contributor of magnitude uncertainty is sky background variation. Since the mean sky background level has already been subtracted in the HLA frames, directly determining a realistic S/N ratio is not possible. Therefore, we estimated the amplitude of sky background variation by fitting the Gaussian profile to the histogram of pixel values. However, the histogram is generally asymmetric due to the presence of bright resolved stars, which do not represent the true sky background and significantly skew the distribution. The asymmetric distribution of pixel values is shown by the grey bars in Fig. 3.3. In the initial step, we applied a  $2\sigma$  clipping in order to remove outliers, resulting in the red bars used for the first Gaussian fit. To enhance the accuracy of the fit, we then excluded all pixel values exceeding the full width at half maximum of the initial Gaussian. The remaining values (green bars) were used for the final fit, where the sky background flux variation per pixel was then derived as the Gaussian  $\sigma_{\text{sb}}$  (Naujalis et al. 2021). Thus, the first part of magnitude uncertainty in each passband, arising due to sky background variations, was calculated as:

$$\sigma_1 = 2.5 \log_{10} \left( 1 + \frac{\sigma_{\text{sb}} \sqrt{A_{\text{ap}}}}{F_{\text{cl}}} \right), \quad (3.1)$$

where  $F_{\text{cl}}$  is the integrated cluster flux inside the T or C aperture and  $A_{\text{ap}}$  is the area of aperture in pixels.

The second part of errors could arise because of a possible aperture position bias and different sizes of stellar images in various passbands. To estimate these effects, we performed photometry at eight additional positions symmetrically shifted by  $0''.05$  (one pixel in ACS/WFC) around the cluster's centre for C magnitudes and by  $0''.1$  (two pixels in ACS/WFC) for T magnitudes. The standard deviation ( $\sigma_2$ ) was calculated from these nine independent cluster measurements in each passband. The final uncertainty ( $\sigma$ ) of the cluster photometry in each passband was calculated as:

$$\sigma = \sqrt{\sigma_1^2 + \sigma_2^2}. \quad (3.2)$$

In Figs. 3.4 and 3.5, we show estimated T and C magnitude uncertainties. Photometric errors in the UV passbands are dominated by sky background uncertainties ( $\sigma_1$ ) and correlate with magnitudes, except for a few dozens of clusters which have

a higher scattering due to a small S/N ratio or CR artefact residues. Uncertainties in the IR passbands are more widely scattered due to the presence of irregularly distributed bright stars ( $\sigma_2$ ), making these measurements more sensitive to aperture size and centre position compared to other passbands.

In Fig. 3.6, we show the differences between photometric uncertainties derived from T and C magnitudes versus C magnitudes for each passband. The uncertainties in the  $F475W$  passband remain consistent, as this filter was used as the reference during the aperture correction process. As expected, the largest discrepancies in uncertainties are observed in the  $F275W$ ,  $F110W$ , and  $F160W$  passbands. The differences in the  $F275W$  passband increase with the magnitude due to lower S/N ratios for fainter objects. As clusters emit less intrinsic light in the UV, the impact of cosmic ray defects may become more pronounced in the observed data. In contrast, the  $F336W$  and  $F814W$  passbands show smaller photometric uncertainty differences, benefiting from higher S/N ratios and lower sensitivity to variations in extinction. The uncertainty differences in the IR passbands are more dispersed due to the presence of irregularly distributed bright stars. In some cases, C magnitudes exhibit higher uncertainty values as a result of low S/N ratios, particularly when no bright stars are present within the photometric aperture.

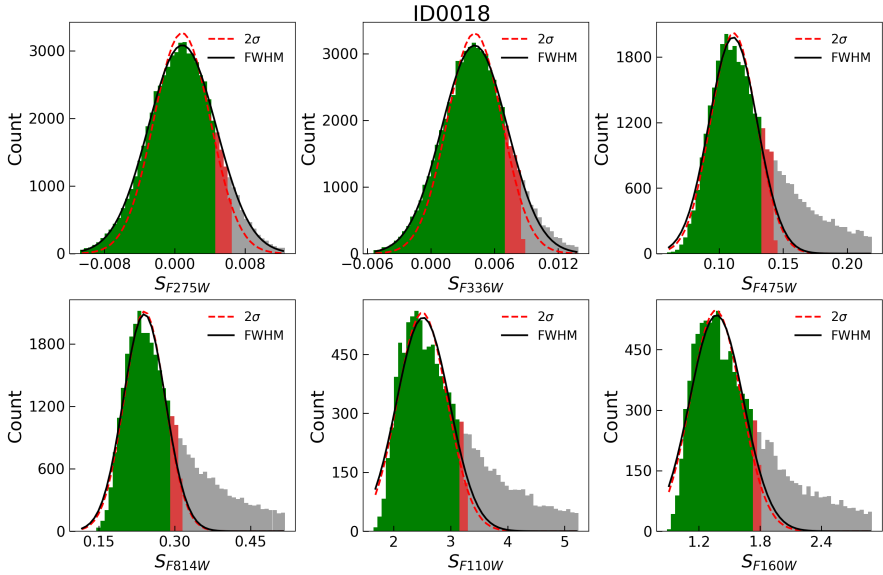


**Figure 3.3.** The signal histogram of pixels in the background region of cluster AP0018 (grey bars). The background region covers a ring around the cluster from  $1.2R_T$  to  $3.4R_T$ . Red bars represent data remaining after  $2\sigma$  clipping, while the red dashed line indicates the first Gaussian profile fitted to these values. Green bars correspond to data remaining after removing pixel signal values greater than the full width at half maximum of the initial Gaussian fit. The final Gaussian fit is represented by the black solid line.

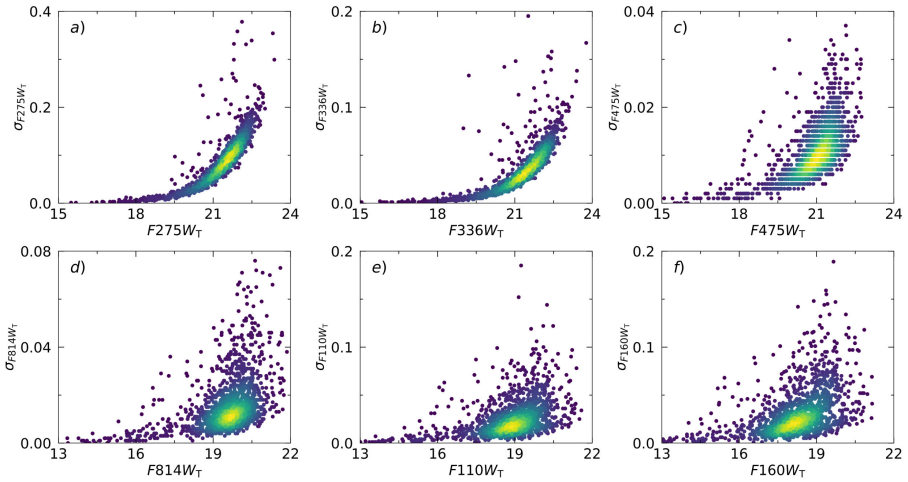


**Figure 3.4.** Photometric uncertainties of star cluster T magnitudes ( $\sigma_T$ ) in all six passbands versus their T magnitudes. The colours of dots indicate the local point density.

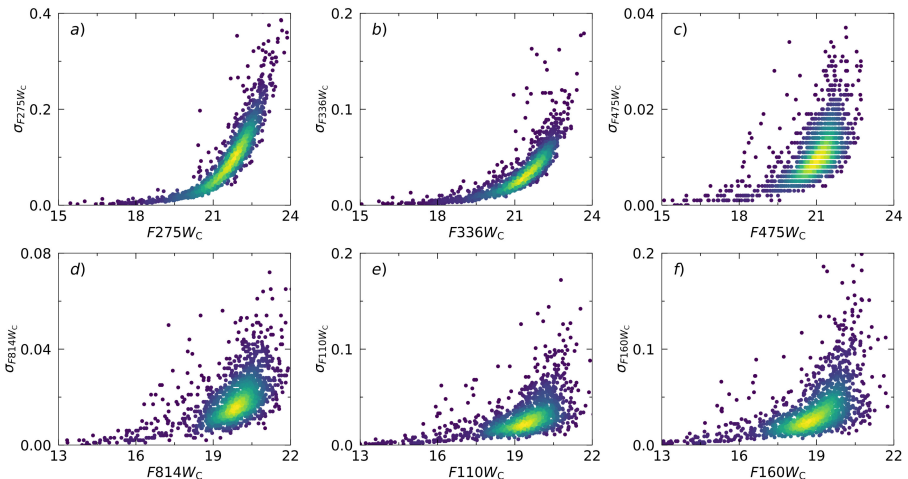


**Figure 3.5.** Photometric uncertainties of star cluster C magnitudes ( $\sigma_C$ ) in all six passbands versus their C magnitudes. The colours of dots indicate the local point density.

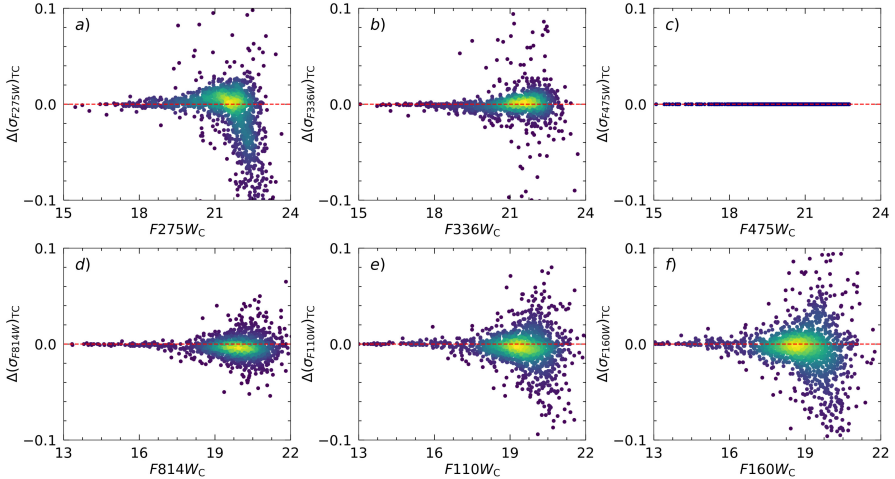


**Figure 3.6.** Differences between uncertainties derived from the T and C magnitudes (the uncertainty calculated from T magnitudes minus the uncertainty calculated from C magnitudes). The colours of dots indicate the local point density.

### 3.4 Multi-colour photometry results

The photometry results, along with photometric errors ( $\sigma$ ) in each passband have been compiled for all 1477 studied clusters. A subset of the T aperture photometry results is presented in Table 3.2, while a subset of the C aperture photometry results is provided in Table 3.3. To analyse the entire sample of star clusters possessing homogeneous aperture photometry, we merged cluster catalogues presented in this study (1477 objects) and in Naujalis et al. (2021) (1181 objects).

In Fig. 3.7, we show the differences between colour indices derived from T and C magnitudes versus C magnitudes. The differences arise due to the C apertures, which are selected to avoid the brightest field and cluster stars. Other parameters affecting photometry, such as star cluster positions, T aperture sizes, and sky background levels, remain the same in the cases of both apertures. Therefore, the large differences in Fig. 3.7 show a high sensitivity to the presence of bright field stars and highlight the importance of a careful consideration of the problems addressed in this study.

In order to test the quality of our photometry data, we compare the results with stochastic star cluster models in the age range of  $\log_{10}(t/\text{yr})$  from 6.6 to 10.1, masses from  $10^2 M_\odot$  to  $10^5 M_\odot$ , and in the metallicity, [M/H], range from -2.2 to +0.4. These models are based on the PAdova and tRieste Stellar Evolutionary Code (PARSEC)-COLIBRI isochrones<sup>4</sup> (Marigo et al. 2017) and were computed using the same method as described in Deveikis et al. (2008); de Meulenaer et al. (2017); Daugevičius et al. (2024). Free-of-extinction models are plotted in the background of Figs. 3.8 and 3.9.

In Fig. 3.8, we show two-colour diagrams (TCDs) constructed from T aperture photometry (panels a-c) and C aperture photometry (panels d-f) results compared to

<sup>4</sup><http://stev.oapd.inaf.it/cgi-bin/cmd>

**Table 3.2.** M 31 star cluster T aperture photometry results.

AP	RA(2000) <sup>(a)</sup>	DEC(2000) <sup>(a)</sup>	R <sub>T</sub> <sup>(b)</sup>	F275W <sub>T</sub>	F336W <sub>T</sub>	F475W <sub>T</sub>	F814W <sub>T</sub>	F110W <sub>T</sub>	F160W <sub>T</sub>
12	11.45697	41.65734	1.95	21.201 0.082	20.491 0.017	19.887 0.005	18.384 0.004	17.784 0.005	17.124 0.007 <sup>(c)</sup>
17	11.49040	42.02750	1.80	20.857 0.057	20.724 0.019	20.377 0.005	19.523 0.006	19.326 0.013	19.066 0.020
18	10.87149	41.57674	1.80	20.035 0.030	19.946 0.010	19.860 0.006	19.128 0.013	18.171 0.020	17.364 0.019
36	11.11896	41.49611	1.50	20.218 0.028	20.052 0.009	20.071 0.005	19.358 0.010	19.124 0.027	18.798 0.039
59	11.35843	41.93100	2.20	21.018 0.080	20.409 0.019	19.893 0.008	19.345 0.017	19.034 0.019	18.332 0.019
60	11.15443	41.84543	1.90	20.346 0.041	20.234 0.018	19.830 0.004	18.953 0.009	18.540 0.012	18.019 0.017
61	11.33710	41.95119	1.75	20.825 0.048	20.536 0.015	20.258 0.013	19.249 0.041	18.690 0.072	18.109 0.094
70	11.86315	41.98962	2.00	21.250 0.086	20.993 0.024	20.724 0.007	20.080 0.012		
71	11.04998	41.84103	1.40	22.386 0.184	21.533 0.032	20.911 0.007	19.000 0.009		
83	11.17470	41.41221	1.80	20.627 0.046	20.416 0.014	20.079 0.005	18.978 0.009	18.749 0.024	18.146 0.030
89	11.29143	41.70648	2.00	20.417 0.042	19.905 0.011	19.528 0.003	18.623 0.005	18.115 0.010	17.493 0.012
99	10.80829	41.18881	2.20	19.026 0.013	18.309 0.003	18.053 0.002	16.711 0.003	16.228 0.006	15.676 0.008
108	11.24786	41.91301	3.40	18.805 0.016	18.579 0.005	18.243 0.002	17.233 0.003	16.657 0.005	16.156 0.008
111	10.75556	41.43999	1.40	20.704 0.040	19.995 0.008	19.621 0.006	18.403 0.020	17.755 0.028	17.158 0.043
112	10.99776	41.10297	3.00	18.840 0.025	17.715 0.002	17.810 0.001	16.381 0.001		
129	11.65914	42.00298	1.40	20.244 0.025	20.143 0.009	20.291 0.006	19.507 0.010	18.942 0.044	18.140 0.053
131	11.52651	41.84367	1.80	20.267 0.036	19.877 0.009	19.695 0.004	18.910 0.008	18.462 0.009	18.005 0.010
136	11.50835	41.83461	1.90	21.273 0.096	20.916 0.035	20.594 0.007	19.621 0.006	19.359 0.014	19.039 0.022
146	11.14159	41.28450	1.50	22.181 0.147	20.739 0.015	20.264 0.007	18.809 0.017	18.310 0.020	17.783 0.022
153	10.90920	41.60673	2.90	19.996 0.054	20.539 0.032	18.926 0.003	16.837 0.002	15.868 0.003	15.011 0.003
157	10.90755	41.55624	1.40	21.510 0.091	20.655 0.018	20.225 0.007	19.073 0.014	18.335 0.018	17.592 0.016
159	11.06652	41.70332	1.55	21.874 0.136	21.497 0.038	20.959 0.010	19.450 0.011	18.720 0.015	18.046 0.016
162	11.26140	41.78398	1.70	22.354 0.198	21.490 0.036	20.659 0.008	18.548 0.006	17.718 0.006	16.995 0.007
166	10.82595	41.18186	2.50	17.983 0.006	17.269 0.001	17.008 0.001	15.606 0.001	15.142 0.002	14.528 0.002
196	11.44276	41.80583	2.40	20.582 0.060	20.246 0.017	19.757 0.004	18.249 0.004	17.296 0.004	16.432 0.004
199	11.65336	42.29523	1.90	21.229 0.092	21.169 0.047	20.918 0.006	19.823 0.007	19.303 0.006	18.860 0.007
202	11.61429	41.99898	1.40	19.338 0.012	19.436 0.005	19.971 0.003	19.683 0.008	19.704 0.020	19.510 0.038
205	11.30743	41.70952	1.20	21.482 0.074	20.960 0.018	20.566 0.006	19.695 0.008	19.552 0.023	19.241 0.050
209	11.16939	41.50176	1.80	20.316 0.037	19.953 0.010	19.516 0.004	18.410 0.006	17.885 0.017	17.387 0.023
211	11.60530	42.26599	2.00	21.206 0.095	21.885 0.063	20.937 0.005	18.594 0.002	17.454 0.001	16.560 0.001

**Notes.** The table shows an excerpt from data presented in the catalogue. <sup>(a)</sup>The RA(2000) and DEC(2000) coordinates are in degrees. <sup>(b)</sup>The T aperture is in arcseconds. <sup>(c)</sup>The uncertainties of T magnitudes ( $\sigma_T$ ) in corresponding passbands.

**Table 3.3.** M 31 star cluster C aperture photometry results.

AP	RA(2000) <sup>(a)</sup>	DEC(2000) <sup>(a)</sup>	R <sub>C</sub> <sup>(b)</sup>	F275W <sub>C</sub>	F336W <sub>C</sub>	F475W <sub>C</sub>	F814W <sub>C</sub>	F110W <sub>C</sub>	F160W <sub>C</sub>
12	11.45697	41.65734	0.80	21.533 0.103	20.539 0.017	19.887 0.005	18.547 0.007	18.083 0.009	17.543 0.010 <sup>(c)</sup>
17	11.49040	42.02750	0.95	20.898 0.055	20.660 0.017	20.377 0.005	19.715 0.009	19.595 0.014	19.406 0.023
18	10.87149	41.57674	0.90	20.055 0.024	19.896 0.010	19.860 0.006	19.534 0.013	19.423 0.031	19.081 0.045
36	11.11896	41.49611	1.20	20.224 0.024	20.080 0.014	20.071 0.005	19.370 0.011	19.132 0.027	18.810 0.040
59	11.35843	41.93100	1.70	20.900 0.065	20.369 0.018	19.893 0.008	19.316 0.012	18.991 0.018	18.387 0.021
60	11.15443	41.84543	1.35	20.315 0.033	20.188 0.035	19.830 0.004	19.046 0.012	18.860 0.019	18.568 0.026
61	11.33710	41.95119	1.20	20.961 0.049	20.537 0.018	20.258 0.013	19.606 0.016	19.462 0.025	19.231 0.036
70	11.86315	41.98962	2.00	21.250 0.081	20.993 0.025	20.724 0.007	20.080 0.011		
71	11.04998	41.84103	1.00	22.562 0.163	21.707 0.030	20.911 0.007	19.060 0.010		
83	11.17470	41.41221	0.85	21.117 0.057	20.619 0.015	20.079 0.005	19.051 0.010	18.760 0.015	18.221 0.018
89	11.29143	41.70648	0.85	20.556 0.034	19.855 0.009	19.528 0.003	18.735 0.006	18.528 0.011	18.179 0.016
99	10.80829	41.18881	1.40	19.028 0.011	18.314 0.003	18.053 0.002	16.716 0.003	16.255 0.004	15.710 0.005
108	11.24786	41.91301	1.50	18.659 0.012	18.452 0.005	18.243 0.002	17.363 0.004	16.915 0.005	16.466 0.007
111	10.75556	41.43999	0.90	20.601 0.029	20.006 0.009	19.621 0.006	18.555 0.009	18.118 0.017	17.653 0.024
112	10.99776	41.10297	1.80	18.866 0.012	17.622 0.004	17.810 0.001	16.369 0.001		
129	11.65914	42.00298	1.00	20.721 0.037	20.386 0.014	20.291 0.006	19.555 0.009	19.156 0.013	18.509 0.015
131	11.52651	41.84367	1.80	20.267 0.034	19.877 0.010	19.695 0.004	18.910 0.006	18.462 0.008	18.005 0.009
136	11.50835	41.83461	1.00	21.396 0.078	20.897 0.020	20.594 0.007	19.798 0.010	19.584 0.016	19.327 0.020
146	11.14159	41.28450	1.30	22.182 0.133	20.755 0.016	20.264 0.007	18.836 0.008	18.379 0.010	17.879 0.011
153	10.90920	41.60673	1.75	20.468 0.079	20.484 0.029	18.926 0.003	16.896 0.005	15.926 0.005	15.106 0.005
157	10.90755	41.55624	1.40	21.510 0.088	20.655 0.019	20.225 0.007	19.073 0.013	18.335 0.018	17.592 0.017
159	11.06652	41.70332	1.00	22.058 0.123	21.584 0.032	20.959 0.010	19.485 0.015	18.892 0.018	18.188 0.020
162	11.26140	41.78398	0.50	22.584 0.214	21.609 0.036	20.659 0.008	18.869 0.015	18.320 0.019	17.727 0.024
166	10.82595	41.18186	1.70	17.968 0.004	17.276 0.002	17.008 0.001	15.590 0.002	15.089 0.002	14.477 0.002
196	11.44276	41.80583	1.55	21.088 0.081	20.321 0.017	19.757 0.004	18.244 0.006	17.177 0.007	16.315 0.007
199	11.65336	42.29523	1.90	21.229 0.092	21.169 0.036	20.918 0.006	19.823 0.009	19.303 0.010	18.860 0.010
202	11.61429	41.99898	1.40	19.338 0.012	19.436 0.006	19.971 0.003	19.683 0.006	19.704 0.012	19.510 0.022
205	11.30743	41.70952	1.20	21.482 0.072	20.960 0.019	20.566 0.006	19.695 0.010	19.552 0.023	19.241 0.036
209	11.16939	41.50176	1.20	20.394 0.035	20.003 0.012	19.516 0.004	18.436 0.014	17.912 0.017	17.393 0.020
211	11.60530	42.26599	1.50	21.344 0.099	21.882 0.058	20.937 0.005	18.563 0.007	17.370 0.007	16.466 0.007

**Notes.** The table shows an excerpt from data presented in the catalogue. <sup>(a)</sup>The RA(2000) and DEC(2000) coordinates are in degrees. <sup>(b)</sup>The C aperture is in arcseconds. <sup>(c)</sup>The uncertainties of C magnitudes ( $\sigma_C$ ) in corresponding passbands.

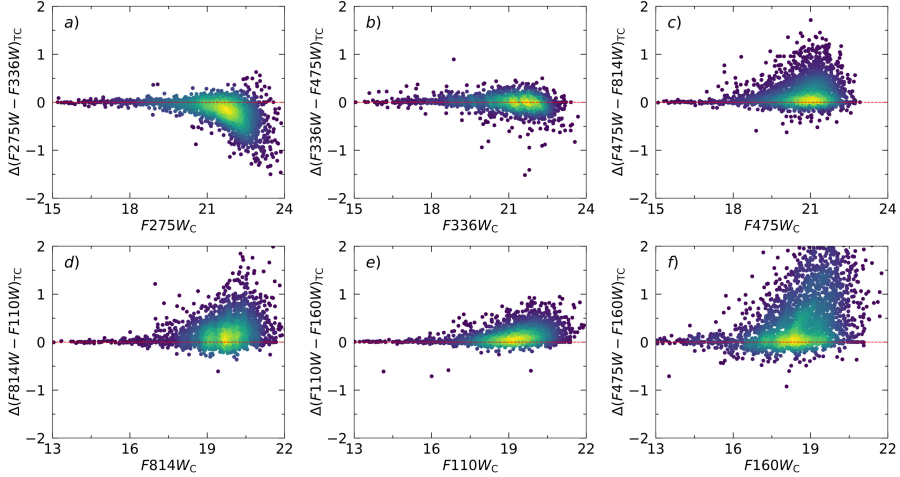


**Figure 3.7.** Differences between colour indices derived from the T and C magnitudes (the colour index calculated from T magnitudes minus the colour index calculated from C magnitudes).

the stochastic models (grey in the background). The C aperture photometry results of star clusters follow theoretical models closely for all colour index combinations. The largest differences between the T and C colours are observed in the IR passbands, primarily due to the stronger contamination by numerous red field stars. Photometric results (C magnitudes) of the youngest star clusters are less reliable because measured fluxes are very faint in the IR passbands (Fig. 3.8f). The accuracies of UV colour indices (Fig. 3.8a,d) are limited due to the low S/N ratio rather than other biases. Outliers in Fig. 3.8d-f usually have very complicated surrounding sky backgrounds, or have bright field stars falling inside the C aperture. Some star clusters are strongly affected by the presence of interstellar extinction; noticeable systematic shifts in colour indices are evident when comparing observed clusters with the stochastic star cluster models. The extinction vectors, assuming the standard Milky Way extinction law, are shown at the bottom-left corners of panels. In Fig. 3.9a, we show photometry results by applying T aperture magnitudes in the  $F336W$ ,  $F475W$ , and  $F814W$  passbands; in Fig. 3.9b: photometry results by applying the C apertures. Most clusters align well with the star cluster models drawn in the background. However, the C photometry results, compared with the stochastic star cluster models, are more compatible than the T photometry results.

### 3.5 Stochastic effects of star clusters

To investigate the impact of stochastic effects on star cluster aperture photometry, we used artificial star clusters to examine how the stochastic nature of low-mass clusters affects the measurement of photometric parameters. Stochastic sampling of the initial mass function is one of the main factors limiting the accuracy and reliability of cluster physical parameters derived using aperture photometry.

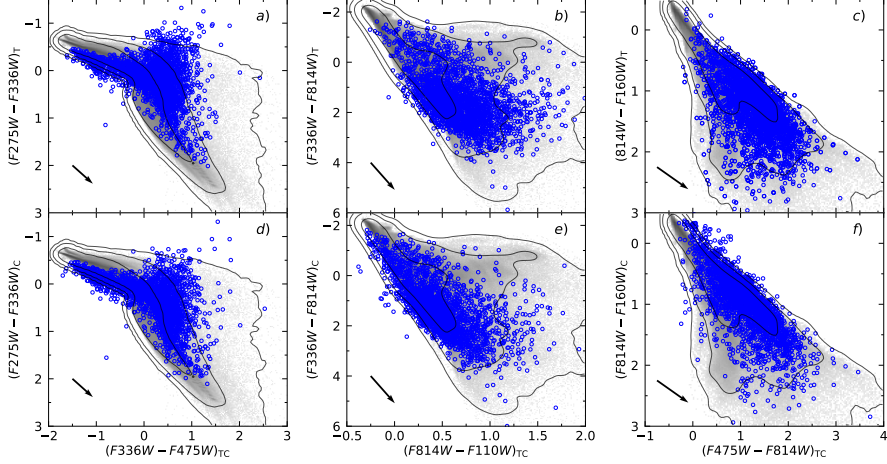


**Figure 3.8.** Two-colour diagrams showing photometry results of star clusters. Panels a-c show T aperture photometry; panels d-f give the C aperture photometry. The grey colour in the background indicates areas occupied by stochastic star cluster models with masses from  $10^2$  to  $10^5$   $M_\odot$ . Colour indices indicated on the X axis are constructed from T magnitudes in panels a-c and from C magnitudes in panels d-f. Arrows indicate the extinction vectors of  $A_V = 1$ , assuming the standard Milky Way extinction law.

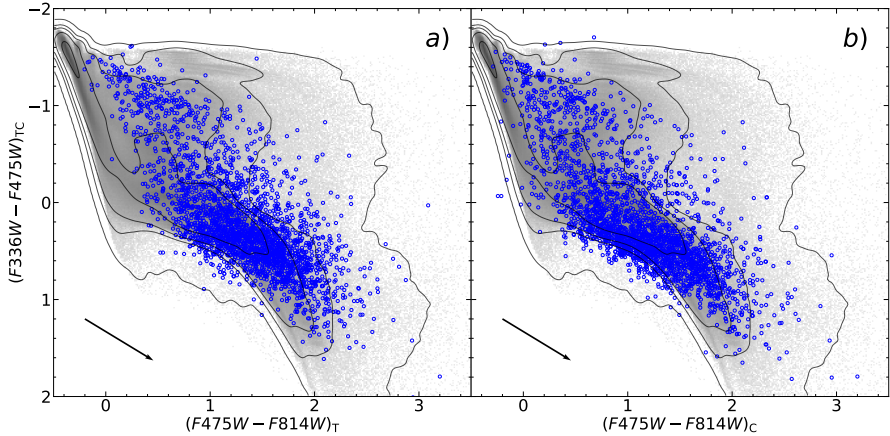


**Figure 3.9.** Two-colour diagrams showing star clusters over-plotted on the distributions of models. The models of clusters (areas of grey colour) are with masses from  $10^2$  to  $10^5$   $M_\odot$ . The subscript TC indicates that colour index is based on T and C aperture photometry in panels a and b, respectively. Arrows indicate extinction vectors of  $A_V = 1$ , assuming the standard Milky Way extinction law.

In order to generate an artificial star cluster, we assigned stellar masses by randomly sampling the IMF, which defines the number of stars formed within a given mass range. In this study, we used the Kroupa (2001) IMF, defined by the multi-power law:

$$\xi(m) = k \cdot b_i \cdot m^{-\alpha_i}, \quad (3.3)$$

where  $\alpha_i$  – the IMF slope for the mass range of  $[m_{i-1}, m_i]$ ,  $k$  and  $b_i$  – the normalisation and continuation constants of the function, respectively. We sampled the initial stellar masses within the range of 0.1 to  $100 M_\odot$ . In this mass range, the Kroupa IMF simplifies to an equation, characterized by two power-law slopes:

$$\begin{cases} \alpha_1 = 1.3, & \text{if } m < 0.5 M_\odot, \\ \alpha_2 = 2.3, & \text{if } m \geq 0.5 M_\odot. \end{cases} \quad (3.4)$$

Individual stars are fully stochastic sampled until the total mass within a sphere of  $7.5''$  radius ( $\sim 28$  pc at the M 31 distance) matches the cluster's target mass. After generating stellar masses, magnitudes were assigned based on each star's mass and the cluster's age. To accomplish this, we interpolated the PARSEC-COLIBRI (Marigo et al. 2017) isochrones. For this study, we adopted a fixed solar metallicity and zero interstellar extinction. To generate realistic artificial clusters that resemble M 31 objects observed in the PHAT survey, isochrones were interpolated across six corresponding HST passbands, covering a spectral range from 0.25 to  $1.6 \mu\text{m}$ . As a result, we produced a grid of artificial star cluster models that span the parameter space of real clusters observed in M 31 (Daugevičius et al. 2024).

The PARSEC isochrones were selected because they offer a wide coverage of stellar parameters, including age, mass, and metallicity. They are compatible with many photometric systems. Additionally, PARSEC isochrones include fast transient evolutionary phases, which are essential for modelling integrated cluster light, especially at young ages. In contrast, other isochrone models do not include young ages at all, e.g., BaSTI models (Hidalgo et al. 2018) start at around  $\sim 13$  Myr. The Yonsei-Yale and Dartmouth isochrones, while valuable for certain applications, provide more limited coverage in mass, metallicity, and lack consistent updates for later evolutionary phases.

The CMDs in Fig. 3.10 show three artificial clusters of the same mass ( $1000 M_\odot$ ) along with the appropriate isochrones. This illustrates that for young low-mass clusters, significant variations arise despite having the same physical parameters due to the effects of IMF stochasticity. In such cases, measured properties of star clusters will differ from those obtained using the standard SSP integration method, which accounts for all stellar evolutionary phases. This issue is particularly important for lower-mass clusters ( $\leq 10^4 M_\odot$ ), where a single PMS star can cause significant changes in photometric properties.

Figures 3.11 and 3.12 provide a clear presentation of stochastic sampling effects on cluster photometry, where we show TCDs and CMDs of simulated clusters, based on their initial mass and age (Daugevičius et al. 2024). These figures also show the PARSEC-COLIBRI non-stochastic simple stellar population models with solar metallicity (Marigo et al. 2017). As noted in previous studies (Deveikis et al. 2008; Fouesneau & Lançon 2010; de Meulenaer et al. 2013), low-mass stochastic clusters ( $\log(M/M_\odot) \leq 4.0$ ) show significant scatter, with colour indices and fluxes varying across multiple magnitudes. In general, the scatter of photometric parameters

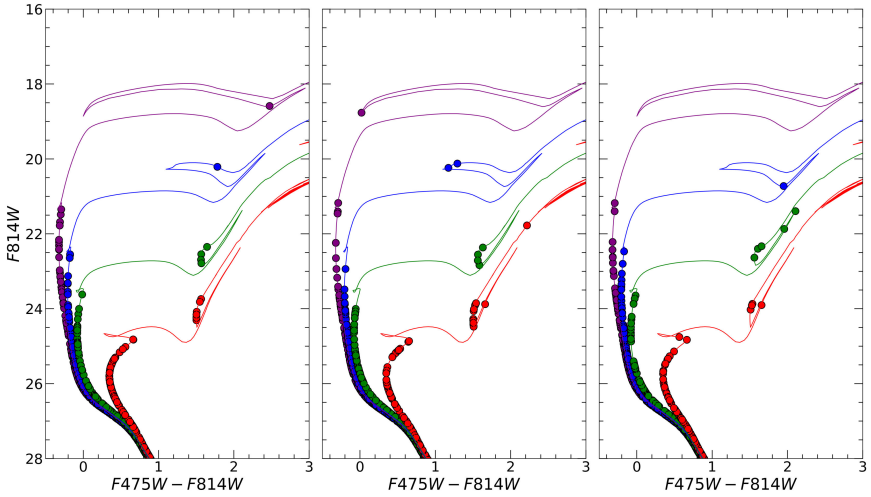


**Figure 3.10.** CMDs of three simulated clusters of mass  $1000 M_{\odot}$  and of age: 30 Myr (purple), 100 Myr (blue), 300 Myr (green), and 1 Gyr (red). Solid lines mark PARSEC-COLIBRI (Marigo et al. 2017) isochrones. Filled circles – individual stars.

is stronger for younger and less massive clusters. This indicates that stochasticity can introduce considerable uncertainties and degeneracies (Worley 1994; Bridžius et al. 2008) in the derived values of cluster age, mass, extinction, and metallicity. Additionally, Figs. 3.11 and 3.12 demonstrate that the brightest clusters with  $\log(M/M_{\odot}) = 2.5$  and  $\log(M/M_{\odot}) = 3.5$  show very similar colours and magnitudes in the visual to near-infrared parts of the spectrum.

For low-mass star clusters (younger than 1 Gyr) two photometrically distinct groups of objects emerge (Figs. 3.11 and 3.12), due to stochastic IMF sampling. The first group, G1, consists of clusters that do not contain any PMS stars, while the second group, G2, includes clusters with at least one evolved PMS star. The difference between these two groups is particularly prominent at young ages ( $\leq 100$  Myr) and gradually diminishes as clusters evolve. With increasing age, the mass of stars at the main sequence turn-off decreases, allowing even low-mass clusters ( $\log(M/M_{\odot}) \leq 3.0$ ) eventually become populous enough to have some evolved stars.

Moreover, similarly to previous studies (Deveikis et al. 2008; Bridžius et al. 2008; Fouesneau & Lançon 2010; de Meulenaer et al. 2013), our results demonstrate that non-stochastic SSP models – commonly used to derive physical parameters of stellar populations – are an inappropriate approximation. Figs. 3.11 and 3.12 indicate that at young ages, the non-stochastic SSP models lie in regions of the TCD and CMD that are sparsely populated by stochastic clusters. These models poorly represent young clusters ( $\leq 100$  Myr), placing them between the two stochastic cluster groups. It is worth noting that at 1 Gyr, the non-stochastic SSP models align reasonably well with the distribution of stochastic clusters. However, stochastic clusters still show a large scatter, covering a wide range of ages compared to the non-stochastic models. In TCDs, the spread of stochastic cluster colours tends to follow the direction of the interstellar extinction vector. In general, these results reinforce the well-established idea that relying on non-stochastic SSP models to derive parameters for low-mass

clusters – especially at younger ages – can lead to misleading results, and stochasticity must be accounted for to obtain reliable parameter estimates.

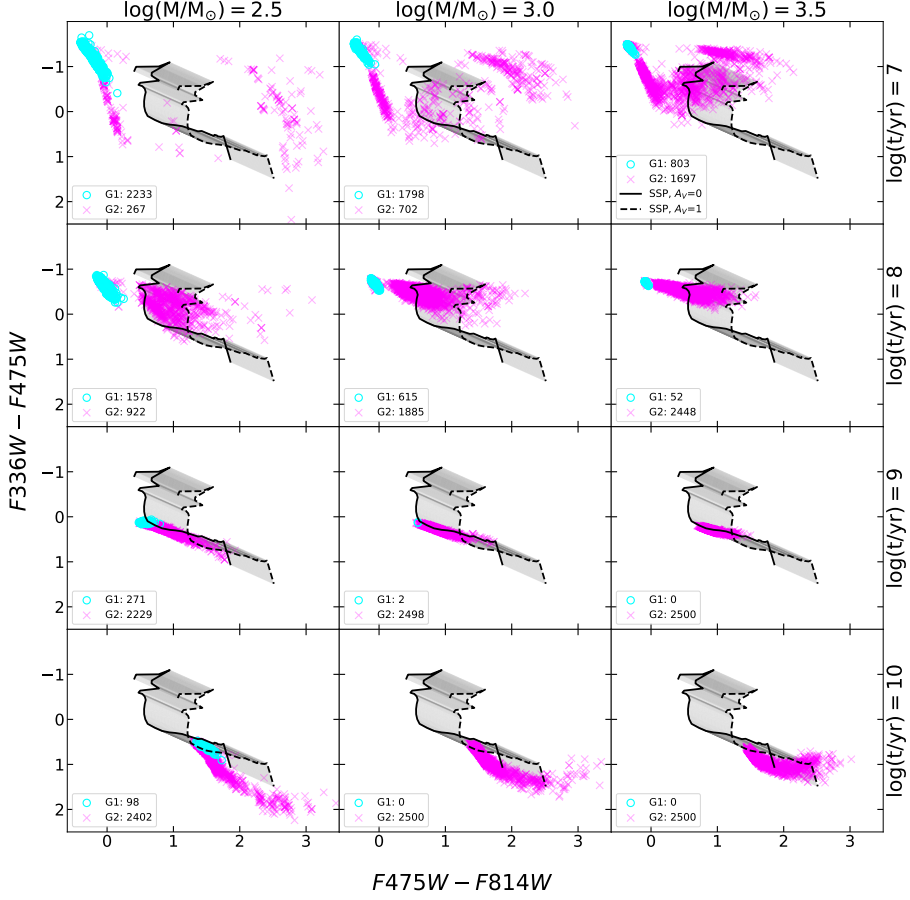


**Figure 3.11.** Two-colour diagrams of simulated stochastic star clusters (Daugevičius et al. 2024). Each panel shows aperture photometry results for different combinations of cluster mass (marked above the panels) and age (marked to the right of the panels). G1 group consists of clusters without any PMS stars, while G2 group includes clusters with at least one evolved PMS star. Black lines (solid – no interstellar extinction; dashed –  $A_V = 1$ , calculated using the Fitzpatrick 1999 extinction curve) PARSEC-COLIBRI-based non-stochastic SSP solar metallicity models (Marigo et al. 2017) from 10 Myr to 12.6 Gyr. Measurements are performed using the circular aperture of radius  $R_{\text{ap}} = 3.0$  arcsec.

Also, we find that G1 clusters tend to exhibit more consistent and reliable photometric measurements, occupying a much narrower area in both TCDs and CMDs compared to G2 clusters. In contrast, G2 clusters appear redder and cover a wider range of colour indices. For low-mass clusters ( $\log(M/M_\odot) \leq 4.0$ ), significant photometric differences between the two groups at young ages are driven by the presence of a few or often just one bright evolved PMS star, such as yellow or red supergiant,

whose flux dominates the overall cluster light. These results align with Beerman et al. (2012) and suggest that a reliable photometry of young low-mass star clusters can be achieved, and physical parameters can be derived with higher precision, if these bright PMS stars are excluded or avoided when performing aperture photometry of clusters.

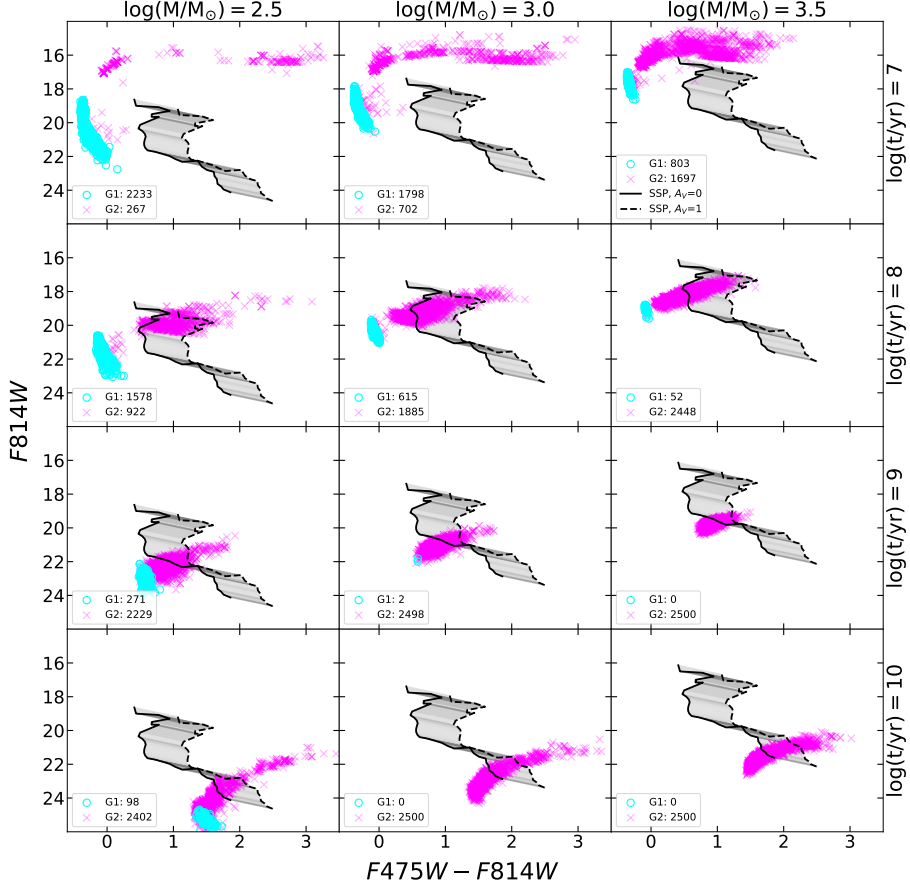


**Figure 3.12.** Same as in Fig. 3.11, but CMDs are shown.

## 3.6 Summary

We performed multi-colour aperture photometry of 1477 star clusters from the M 31 galaxy PHAT survey (Dalcanton et al. 2012; Johnson et al. 2012, 2015). We used two variants of photometry by applying standard (T) and adaptive (C) apertures. A catalogue excerpt for the T and C aperture photometry results are presented in Tables 3.2 and 3.3.

We have demonstrated that the C aperture photometry provides more robust results in the sense of consistent colour indices compared to the T aperture photometry (Fig. 3.8). Two aspects are notable: our photometry results are in a good agreement with the available stochastic cluster models and the T photometry results (Fig. 3.8a-c,

3.9a) differ significantly compared with the C photometry results (Fig. 3.8d-f, 3.9b).

We emphasize two major challenges in performing accurate star cluster aperture photometry in crowded fields: (i) uncertainty in sky background estimation, (ii) contamination from projected field stars within the photometric aperture. Therefore, carefully accounting for both problems is the only way to guarantee reliable star cluster aperture photometry results within the discs of such galaxies as M 31.

Finally, we demonstrate that clusters with PMS stars (G2) and those without (G1) exhibit significant photometric differences, with G2 clusters showing a much larger scatter in photometric parameters. Our findings are in agreement with Beerman et al. (2012), showing that the absence of PMS stars results in much more consistent and well-defined cluster photometric parameters, which in turn lead to a more reliable derivation of physical parameters.

## Appendix: Double clusters

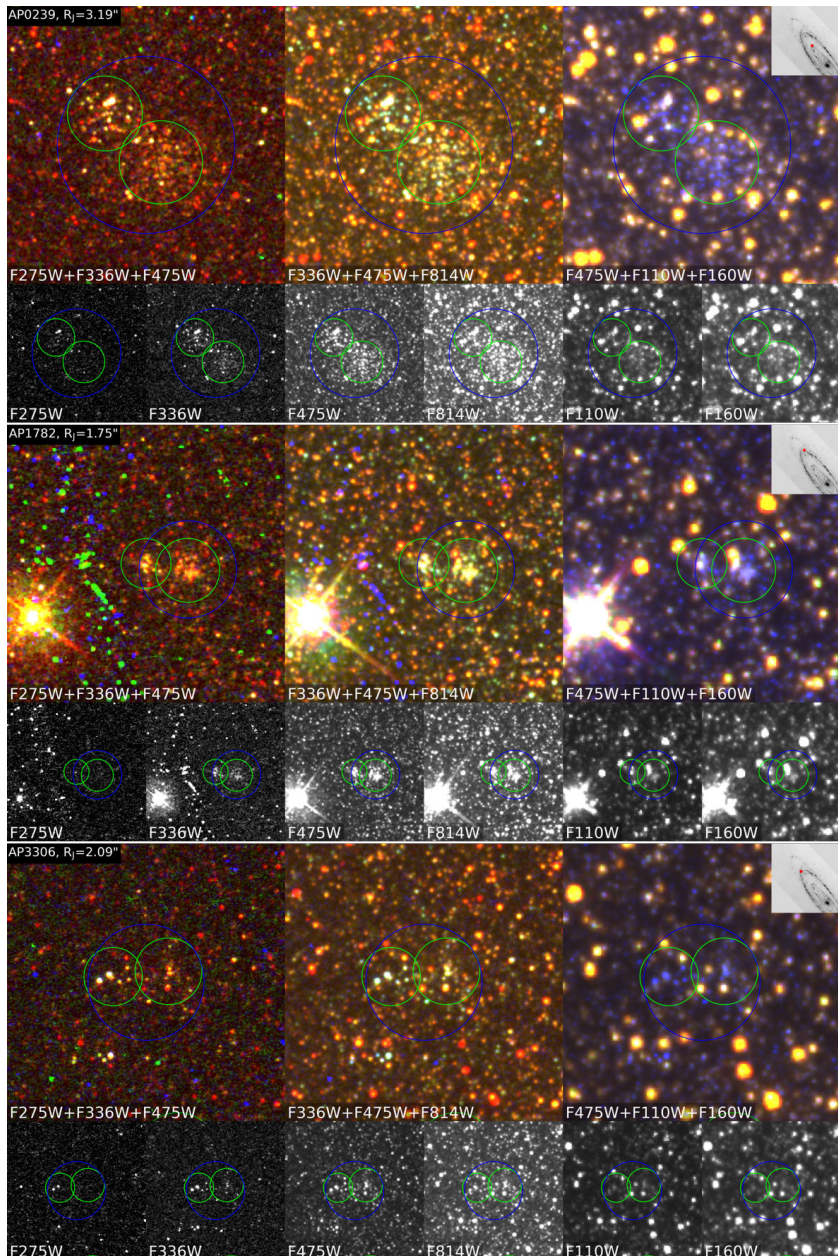


**Figure A1.** Same as in Fig. 2.2, but for the images of clusters: AP0239, AP1782, and AP3306, where double objects were detected. Blue and green circles show Johnson et al. (2015) and T apertures, respectively.

# Chapter 4

## Star cluster parameters

We employed stochastic star cluster models to derive physical parameters (age, mass, metallicity, and colour excess) for the full sample of 2658 clusters in the M 31 galaxy, based on integrated photometry catalogues from Naujalis et al. (2021) and this work.

### 4.1 Cluster parameter determination

Star cluster physical parameters were determined following the procedures described in de Meulenaer et al. (2013, 2014, 2017). The age, mass, metallicity, and colour excess  $E(B - V)$  of star clusters were estimated by comparing the integrated broadband photometry of clusters to a four-dimensional (4D) grid of stochastic models. The grid covers the following parameter ranges: age,  $\log_{10}(t/\text{yr})$  from 6.0 to 10.3 in steps of 0.02; mass  $\log_{10}(M/M_\odot)$  from 2 to 7 in steps of 0.05; metallicity, [M/H] from  $-2.2$  to  $+0.7$  in steps of 0.1; and colour excess,  $E(B - V)$  from  $-0.03$  to  $2.00$  in steps of 0.01. Negative  $E(B - V)$  values are used to account for the average foreground extinction toward the M 31. In this study, each node of the grid contains 10 000 stochastic star cluster models, with the total number of nodes – more than 133 million. Here, a node refers to a specific combination of age, mass, metallicity, and colour excess values in the model grid. These models are constructed by randomly sampling stellar masses according to the initial mass function (Kroupa 2001), following the method described in Deveikis et al. (2008). We adopted a distance modulus of  $(m - M)_0 = 24.47$  (McConnachie et al. 2005), the standard Milky Way interstellar extinction law with  $R_V = 3.1$ , and stellar models from the PARSEC-COLIBRI release v1.2S (Marigo et al. 2017).

We derived physical cluster parameters based on C and T aperture photometry, using five different passband combinations described as follows: F0 we used all six WFC3+ACS filters; F1 we omitted the  $F275W$  passband; F2 we omitted the  $F275W$  and  $F336W$  passbands; F5 we omitted the  $F110W$  passband; F6 we omitted the  $F110W$  and  $F160W$  passbands. For each passband combination, we computed the likelihood of each node of the grid to represent the magnitudes of a given observed cluster. Parameter probabilities were calculated based on Eqs. (1) and (2) from de Meulenaer et al. (2017). Within each node, we first computed the likelihood of each of the 10 000 star cluster models:

$$L_{\text{model}} = \prod_{f=1}^F \frac{1}{\sqrt{2\pi}\sigma_f} \exp \left[ -\frac{(\text{mag}_{f,\text{obs}} - \text{mag}_{f,\text{model}})^2}{2\sigma_f^2} \right], \quad (4.1)$$

where  $f$  denotes a specific PHAT survey filter,  $\text{mag}_{f,\text{obs}}$  and  $\text{mag}_{f,\text{model}}$  represent the observed and model magnitudes in that filter, respectively, and  $F$  is the total number of filters. The likelihood of a node defined by age, mass, extinction, and metallicity is then given by the sum of the likelihoods of its models:

$$L_{\text{node}}(t, M, E(B-V), [\text{M}/\text{H}]) = \sum_{n=1}^N L_{\text{model},n}, \quad (4.2)$$

where  $N$  – number of models within the node. The set of parameters (age, mass, extinction, metallicity) corresponding to the node with the highest likelihood is referred to as BEST. The set of parameters of the node with the highest likelihood in the case of fixed solar metallicity is referred to as BESTsun. Additionally, we adopted the peak values of the one-dimensional probability histograms for age, mass, extinction, and metallicity as the MAX values (see Fig. 4.1).

To decide on the final parameter set for individual M 31 clusters, we visually examined one-dimensional probability histograms for age, mass, extinction, and metallicity, as well as two-dimensional probability density maps of these parameters. The plots produced for each passband combination were compared and evaluated alongside the cluster images, with C and T aperture photometry results analysed separately (see Fig. 4.1 for the F0 case with C aperture). The main goal of this interactive procedure was to ensure an accurate parameter estimation, as the derived values can be influenced by various factors – for instance, the presence of bright UV and IR field stars within the photometric aperture; the significant differential extinction effects across the cluster’s image; strong parameter degeneracies.

Here, we illustrate parameter determination issues using the cluster AP0230 (see Fig. 4.1). This object resides in a dense background of bright blue and red stars. Several bright stars are visible in the  $F814W$ ,  $F110W$ , and  $F160W$  passbands that fall within the C and T apertures, affecting the photometry and, consequently, the derived cluster parameters. Since these stars have colours similar to those of background stars (in the  $F475W+F110W+F160W$  passband combination), we concluded that photometry contaminating stars are most likely field objects. Therefore, we opted to use the C aperture with the F0 filter combination and BESTsun solution, resulting in an estimated age of 300 Myr, which seems appropriate for clusters of this type. The BEST, BESTsun, and MAX results are all consistent for this object. Then, using the model density maps along with the age parameter, we subsequently derived the mass ( $\sim 18\,000\,M_\odot$ ) and colour excess (0.19 mag). Additional parameter determination examples are presented in the Appendix (see Figs. B1–B4). However, for more complex cases, human expertise is essential in deriving the most appropriate parameters.

Another complex case, showing the importance of human expertise in navigating parameter selection issues is cluster AP1867 (Fig. 4.2). This object is heavily affected by interstellar extinction and is likely projected behind the star-forming ring of M 31. Moreover, the presence of young, relatively massive stars, which are bright in the UV, fall within the C and T apertures of the target cluster, affecting parameter derivation results, where cluster is automatically classified as a young object. Such cases have been excluded from the final sample, as their parameters cannot be determined with suffi-

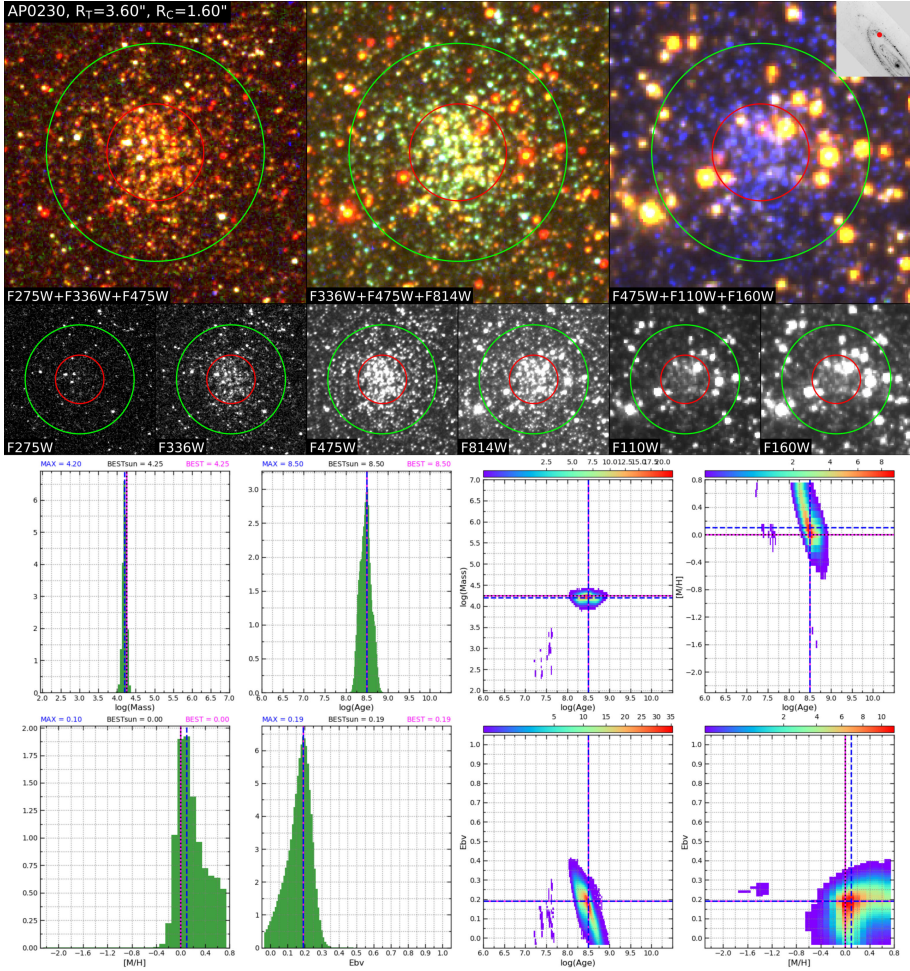


**Figure 4.1.** Top panel: images of the AP0230 cluster in colour (top row) and grey-scale (bottom row) panels. The colour images are generated by combining three passbands, while the grey-scale images show individual passbands (labelled within each panel). Green and red circles indicate T and C apertures, respectively. Each image covers an area of  $10'' \times 10''$ . An insert at the top-right corner shows the location of the cluster within M 31. North is up, and east is to the left. Bottom panel: histograms and density maps representing classification results (likelihoods) for the AP0230 cluster (measured through the C aperture) based on stochastic models. The colours of 2D maps correspond to the number of models representing actual parameter combinations. Redder colours indicate a larger number of models, bluer colours indicate a smaller number. The vertical and horizontal lines show the calculated solution: BEST (magenta), BESTsun (black), MAX (blue). For definitions of the BEST, BESTsun, and MAX parameters, see the text. Derived parameters for the AP0230 cluster are: age –  $\log_{10}(t/\text{yr}) = 8.50$  ( $\sim 300$  Myr), mass –  $\log_{10}(M/M_\odot) = 4.25$  ( $\sim 18\,000 M_\odot$ ), colour excess –  $E(B - V) = 0.19$  mag, metallicity –  $[\text{M}/\text{H}] = 0.0$ .

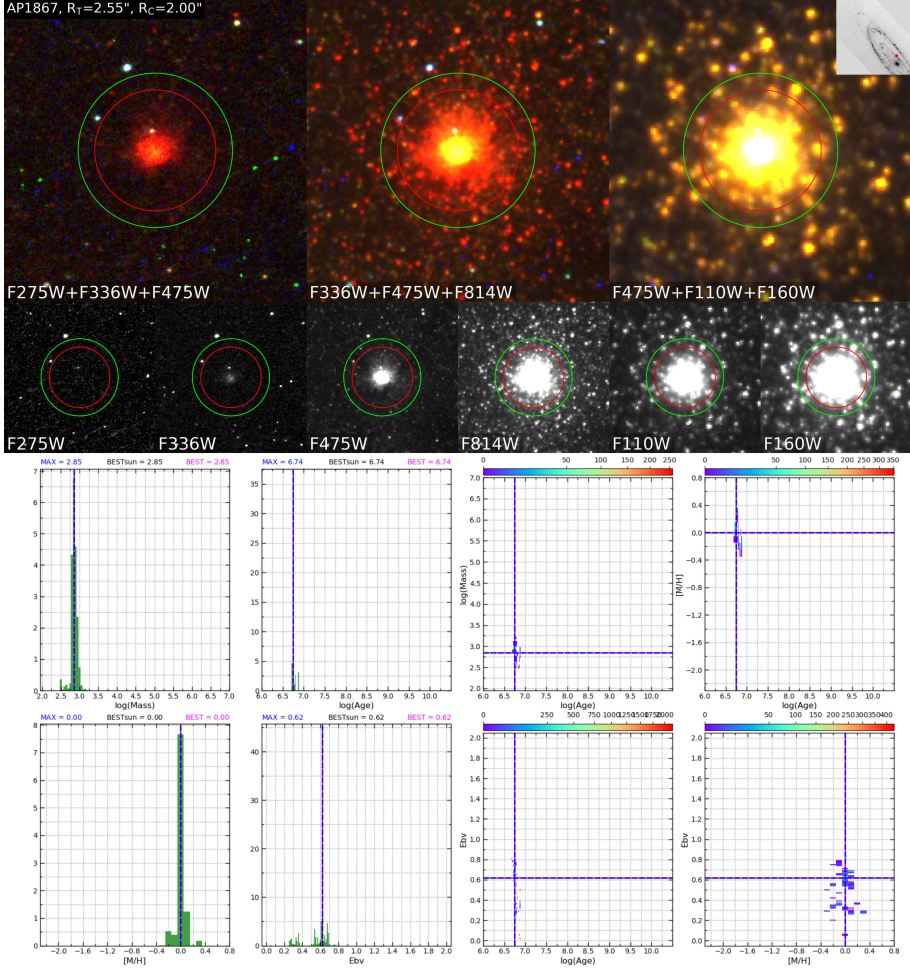


**Figure 4.2.** Same as in Fig. 4.1, but for cluster AP1867. This object was excluded from further analysis due to insufficient parameter reliability. The presence of young, relatively massive stars, that are bright in the UV affect parameter derivation results, where cluster is classified as a young object.

cient reliability. Other examples of excluded objects are presented in the Appendix (see Fig. C1).

After deriving cluster parameters, we excluded 733 objects older than 800 Myr, for which solar metallicity cannot be assumed, as well as clusters heavily contaminated by bright field stars projected within the photometric apertures (Fig. 4.2). For clusters younger than 800 Myr, the colours are nearly insensitive to metallicity. Therefore, we adopted solar metallicity based on Gregersen et al. (2015) findings, who showed that inner disc of M 31 galaxy ( $\sim$ 4-20 kpc) has metallicities close to the solar value. This resulted in a final sample of 1922 clusters.

Moreover, Johnson et al. (2022) and Daugevičius et al. (2024) demonstrated that the parameters of young star clusters ( $\lesssim$ 40 Myr) cannot be reliably determined using only aperture photometry. As a result, the parameters of resolved and semi-resolved young star clusters should be determined using CMD analysis methods (Weisz et al. 2015; Johnson et al. 2016; Wainer et al. 2022; Čeponis et al. 2024), which are likely to provide more accurate results compared to those derived from aperture photometry. Therefore, for the youngest objects, we applied a probabilistic approach to determine the ages and interstellar extinctions of star clusters by fitting theoretical isochrones to the resolved stars within each cluster (Čeponis et al. 2024). To accomplish this, photometric data of individual stars within each cluster's aperture are compared with a database of stellar models, and the probability that a given star matches those parameters is calculated. This comparison produced a probability distribution function (PDF) across a range of age and extinction values, which was then used to identify the best-fitting set of parameters for each cluster. Consistent with our previous approach, we visually inspected the CMDs and PDF distributions of each M 31 cluster under consideration, and determined the final age and extinction values. In total, the CMD-based method was applied to 426 clusters. In all cases, metallicity was fixed to the solar value, and cluster mass was determined using stochastic models.

A subset of parameter results are presented in Table 4.1. Accuracy of the parameters were estimated based on our previous studies of the PHAT cluster samples (Bialopetravičius et al. 2019; Čeponis et al. 2024; Daugevičius et al. 2024). For each cluster, a parameter accuracy ( $\delta$ ) group ( $Q$ ) is indicated and valid for all parameters ( $\log_{10}(t/\text{yr})$ ,  $\log_{10}(M/M_\odot)$ ,  $E(B - V)$ ) as follows:  $Q = 0$  ( $\delta \leq 0.08$ );  $Q = 1$  ( $0.08 < \delta \leq 0.12$ );  $Q = 2$  ( $0.12 < \delta \leq 0.20$ );  $Q = 3$  ( $\delta > 0.20$ ). The number of objects in each group is: 837 for  $Q = 0$ , 654 for  $Q = 1$ , 380 for  $Q = 2$ , and 51 for  $Q = 3$ .

After deriving the physical parameters, we grouped star clusters into bins based on their age and mass, and demonstrate the relationship between their observed photometric properties and the physical parameters (Fig. 4.3). Each subplot shows density contours of observed clusters in the TCDs, using T aperture photometry (dashed blue contours) and C aperture photometry (solid red contours). Blue and red dots represent the centroids of each distribution, highlighting systematic trends across the panels. In the background, light and dark grey points are C and T aperture photometry results.

The vertical shift in the contours indicates the expected reddening of clusters with increasing age. On the other hand, young clusters (top row) appear significantly bluer. The general overlap of red and blue contours across all panels indicates that both C and T aperture photometry give consistent photometric properties when objects are binned by age and mass. While minor offsets appear in certain bins due to stochasticity and field star exclusion, the overall agreement supports the reliability of both methods when determining the physical parameters using stochastic models.

**Table 4.1.** Derived physical parameters of the M 31 star clusters.

AP <sup>(a)</sup>	R.A.(2000) <sup>(b)</sup>	DEC(2000) <sup>(b)</sup>	$\log_{10}(t/\text{yr})^{(c)}$	$\log_{10}(M/M_\odot)^{(d)}$	$E(B-V)^{(e)}$	$R_{50}^{(f)}$	$Q^g$
0001	11.43552	41.69856	8.80	4.35	0.06	0.56	0
0002	11.36651	41.70101	8.56	3.80	0.27	0.59	2
0003	11.47129	42.04925	8.44	3.30	0.21	0.74	1
0004	11.47466	42.03835	8.78	4.20	0.09	0.90	0
0005	10.99164	41.35933	8.48	3.45	0.12	0.36	1
0006	11.12445	41.85557	8.50	3.90	0.12	0.81	1
0007	11.58366	42.25498	8.26	3.25	0.16	0.66	1
0009	11.36310	41.72914	8.50	4.35	0.25	1.11	1
0011	11.81412	42.10896	8.70	3.75	0.32	0.54	1
0013	11.43981	41.76452	8.55	4.25	0.15	0.89	0
0014	11.14083	41.88189	8.20	4.15	0.34	0.73	0
0015	11.08198	41.40248	8.52	3.90	0.09	0.89	1
0016	10.93957	41.14912	8.30	3.60	0.31	0.43	0
0017	11.49040	42.02751	8.64	3.40	0.06	0.72	2
0018	10.87150	41.57674	8.35	3.45	0.10	0.65	1
0023	11.27975	41.42988	8.62	3.85	0.08	0.66	0
0024	11.33163	41.80840	7.30	3.25	0.22	0.33	0
0025	11.64901	42.32663	8.58	3.30	0.12	0.42	2
0027	11.01625	41.27622	7.55	3.60	0.15	0.63	0
0028	11.38640	42.02739	8.60	3.95	0.14	0.52	0
0029	11.52844	42.02333	8.64	4.40	0.13	1.14	0
0031	11.55573	41.82271	8.32	3.40	0.06	0.85	1
0032	11.23506	41.89575	8.18	3.75	0.27	0.88	1
0033	11.87833	42.08423	8.26	3.70	0.18	0.43	1
0034	11.40393	42.00191	8.58	3.75	0.29	0.61	0
0035	11.38898	42.00342	8.44	3.90	0.12	0.81	1
0036	11.11897	41.49612	8.36	3.40	0.10	0.58	2
0044	11.36613	41.95737	8.70	3.95	0.20	0.71	0
0045	11.02481	41.67607	8.40	4.05	0.16	0.96	0
0047	11.45351	41.80560	8.30	4.05	0.39	0.66	0
0048	11.11268	41.57693	8.30	4.15	0.10	0.67	0
0050	11.13551	41.86193	8.34	4.05	0.31	0.72	1
0052	11.03665	41.63221	8.20	4.45	0.10	0.96	0
0053	11.29973	41.93023	8.20	4.05	0.34	0.73	1
0055	11.41601	41.87978	8.40	4.10	0.37	0.87	0
0056	11.14150	41.35086	8.50	3.80	0.10	0.49	2
0059	11.35844	41.93100	8.56	3.55	0.08	1.10	1
0060	11.15443	41.84543	8.64	3.75	0.14	0.73	2
0061	11.33711	41.95119	8.38	3.50	0.22	0.56	2
0063	11.55334	42.15193	8.48	3.65	0.14	0.71	1
0064	11.42251	42.06264	8.68	3.30	0.30	0.56	2
0065	11.33550	41.96125	8.50	3.75	0.26	0.56	0
0066	11.56122	41.92155	8.40	3.15	0.11	0.46	1
0070	11.86316	41.98962	8.64	3.25	0.06	0.94	0
0072	11.26696	41.77239	8.30	4.10	0.42	0.49	0
0080	11.29070	41.91940	8.84	3.95	0.18	0.80	0
0081	11.55928	42.18901	7.30	3.30	0.23	0.39	0
0083	11.17470	41.41221	8.72	3.75	0.17	0.73	0
0084	11.30735	41.83549	8.25	4.15	0.23	0.44	0
0085	11.63698	42.32512	8.14	3.55	0.10	0.56	2
0086	11.19980	41.89623	8.42	3.50	0.11	0.76	1

**Notes.** An excerpt from the full catalogue. Cluster parameters: <sup>(a)</sup> identification number (Johnson et al. 2015); <sup>(b)</sup> equatorial coordinates (degrees) (Naujalis et al. 2021; Kriščiūnas et al. 2023); <sup>(c)</sup> age (years); <sup>(d)</sup> mass (solar masses,  $M_\odot$ ); <sup>(e)</sup> colour excess (magnitudes); <sup>(f)</sup> half-light radius (arcseconds); <sup>(g)</sup> parameter accuracy group.

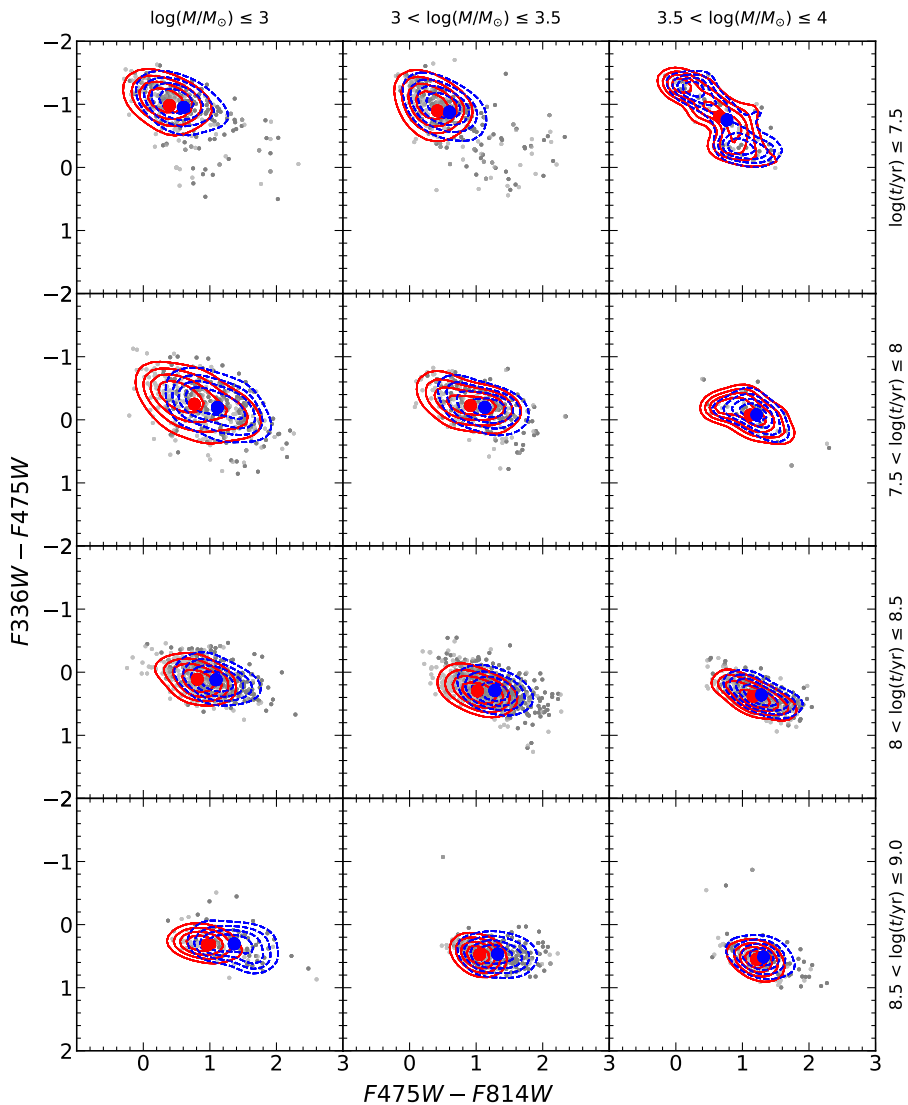


**Figure 4.3.** The relationship between observed photometric and physical properties of star clusters. Each panel shows aperture photometry results for different combinations of cluster mass (marked above the panels) and age (marked to the right of the panels). Red contours represent C aperture photometry and blue contours T aperture photometry results. Red and blue dots indicate the centroid of each respective distribution. Light and dark grey points indicate individual measurements from C and T aperture photometry, respectively.

## 4.2 Comparison with other studies

To verify the reliability of our results, we compare the derived ages, masses, and extinction values with the M 31 star cluster data published by Johnson et al. (2022) and Caldwell & Romanowsky (2016) as shown in Fig. 4.4.

Johnson et al. (2022) determined PHAT cluster parameters based on integrated photometry using the Stochastically Lighting Up Galaxies (SLUG, Krumholz et al. 2015)<sup>1</sup> code, which performs stochastic stellar population synthesis. SLUG method shares some similarities with our stochastic model approach and also has key differences. Both methods rely on stochastic sampling of the IMF to account for variations in stellar content, particularly in low-mass clusters. However, the main difference lies in their fitting procedures. While stochastic models use precomputed grid of models and integrated photometry in discrete filters to derive cluster parameters, SLUG generates models dynamically and compares them to the observed spectral energy distributions.

We excluded 150 clusters in Johnson et al. (2022) catalogue flagged as having uncertain parameter fits. As a result, we used 767 clusters for comparison. As noted by Johnson et al. (2022), the derived SLUG ages have a gap,  $\log_{10}(t/\text{yr}) \sim 7.0 - 7.5$  (Fig. 4.4a). This gap appears to be related to the emergence of evolved supergiant stars. Therefore, we consider the SLUG ages to be less reliable up to  $\log_{10}(t/\text{yr}) = 7.6$ . For older ( $>40$  Myr) clusters, the parameters determined in this study show a reasonable agreement with the SLUG results (Fig. 4.4a-c). The median differences between our and SLUG parameter values:  $\Delta \log_{10}(t/\text{yr}) \sim 0.07$  dex,  $\Delta \log_{10}(M/M_\odot) \sim 0.12$  dex, and  $\Delta A_V \sim -0.09$  mag. Our method favours slightly older ages, higher masses, and lower extinction values (Fig. 4.4a-c). The discrepancies between parameters may arise due to the smaller apertures (C) used for cluster photometry in our study, which reduce contamination from bright field stars that could otherwise lead to parameter degeneracies (Naujalis et al. 2021; Kriščiūnas et al. 2023).

Using an isochrone fitting procedure applied to CMDs of resolved and semi-resolved clusters, Johnson et al. (2016) derived age and mass parameters for young clusters ( $\leq 300$  Myr). In addition, the catalogue was further supplemented with extinction values provided by Johnson et al. (2022), whose data we use for comparison. In total, 851 objects are available for comparison with our data. Most of the derived values are in agreement with each other (Fig. 4.4d-f), showing only small median differences between our and Johnson et al. (2022) parameters:  $\Delta \log_{10}(t/\text{yr}) \sim 0.08$  dex,  $\Delta \log_{10}(M/M_\odot) \sim 0.09$  dex, and  $\Delta A_V \sim -0.09$  mag. Some outliers exhibit large differences in age and(or) extinction (Fig. 4.4d,f), likely due to contamination by bright UV and(or) IR field stars within the cluster apertures. Nonetheless, the strong correlation with parameters derived from CMDs supports the validity of our method of cluster parameter determination.

Using spectroscopy, Caldwell et al. (2009) estimated the age, mass, and extinction of young clusters ( $< 1$  Gyr). In this study, we used updated catalogue from Caldwell & Romanowsky (2016) and compared 53 clusters with our dataset. Our parameter estimates are systematically lower, with median differences between our and Caldwell & Romanowsky (2016):  $\Delta \log_{10}(t/\text{yr}) \sim -0.15$  dex,  $\Delta \log_{10}(M/M_\odot) \sim -0.08$  dex, and  $\Delta A_V \sim -0.24$  mag (Fig. 4.4g-i). Despite some deviations, our age, mass, and extinction estimates remain in reasonable agreement with spectroscopic results. It

<sup>1</sup><https://slug2.readthedocs.io/en/latest/intro.html>

is also worth noting that the age and mass differences are opposite to those when comparing our results with the parameters derived by Johnson et al. (2022).

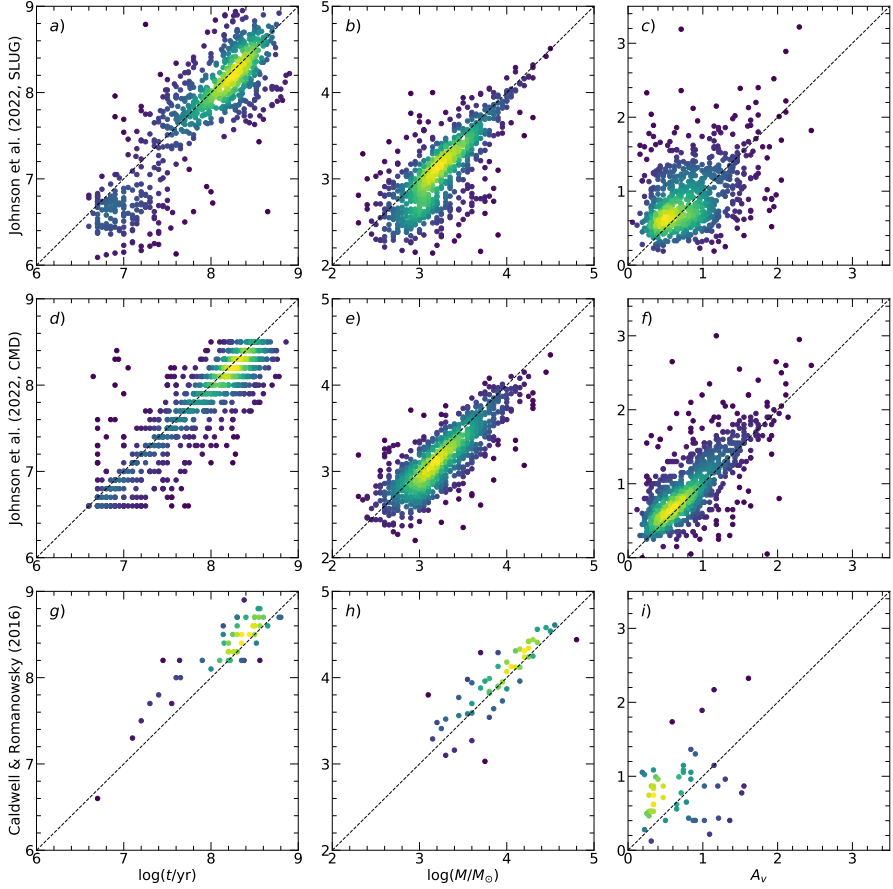


**Figure 4.4.** Comparison of derived cluster parameters: age (left), mass (middle), and extinction (right) – with published values from Johnson et al. (2022) (a-f) and Caldwell & Romanowsky (2016) (g-i). The colours of dots indicate the local point density.

### 4.3 Properties of star clusters

The distribution of clusters in the mass-age diagram is shown in Fig. 4.5a. The red dashed and solid lines represent the approximate selection limits of  $F475W < 21.5$  mag and  $F475W < 22.5$  mag, respectively. They are drawn based on SSP models of solar metallicity and assuming zero extinction. It is worth noting that the actual selection limit is heavily influenced by the cluster’s specific extinction value and the density of field stars in the surrounding environment.

The distribution of cluster masses (Fig. 4.5a) span the range from  $\sim 200 M_{\odot}$  to  $\sim 30\,000 M_{\odot}$ . The decrease in the number of low-mass clusters appears to be influenced by selection effects rather than representing a physical trend. At the same time,

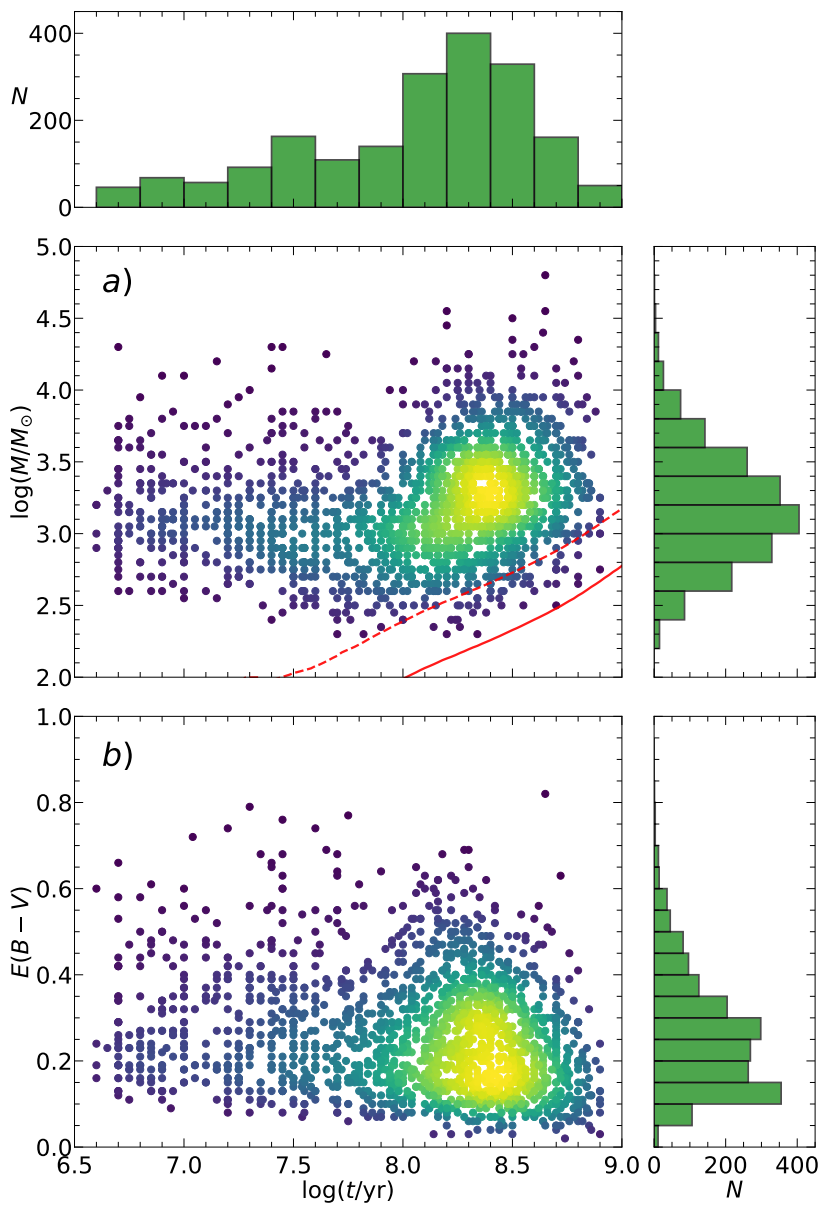


**Figure 4.5.** Top: derived cluster masses versus age. The red dashed and solid lines indicate the cluster selection limits of  $F475W < 21.5$  mag and  $F475W < 22.5$  mag, respectively. Bottom: derived cluster colour excess  $E(B - V)$  versus age. The colours of dots indicate the local point density.

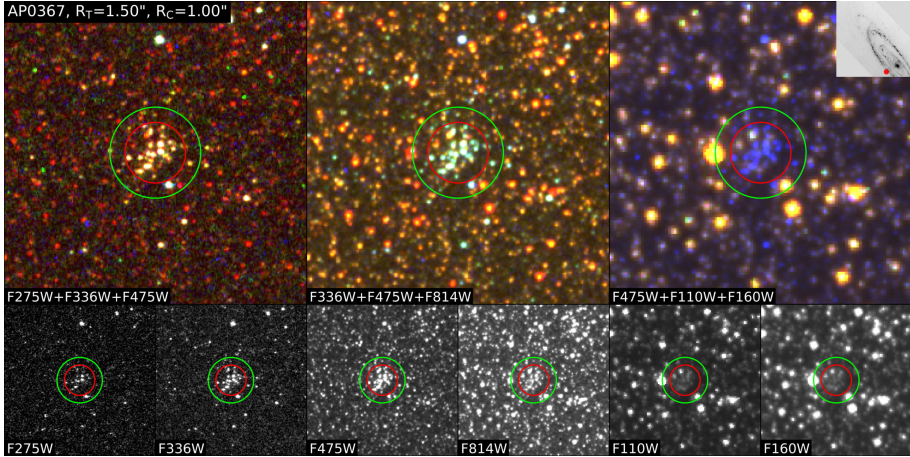


**Figure 4.6.** Same as in Fig. 2.2, but for cluster AP0367, which is affected by differential extinction visible in all colour images.

they are more likely to be disrupted due to tidal interactions, as they have smaller gravitational potentials and lower stellar densities (mass-dependant disruption, Krumholz et al. 2019). While low-mass clusters are indeed more vulnerable to tidal disruption, the observed decrease in their numbers is more likely dominated by selection effects, such as photometric incompleteness, especially at older ages and lower luminosities. The general absence of star clusters with  $\log_{10}(M/M_\odot) > 4.5$  is due to our sample selection. We selected clusters younger than 800 Myr and excluded most massive, and typically older, globular-like clusters. However, the completeness at the  $\sim 2000 M_\odot$  mass (Fig. 4.5a) is suitable for reliable statistical studies, even considering the stochastic nature of stellar mass distribution in clusters of this mass (Daugevičius et al. 2025). Therefore, the observed decline in the number of clusters per logarithmic mass interval in the high-mass range is likely real and well represented for fitting the cluster mass function (CMF). It should be noted that young ( $\lesssim 100$  Myr) and massive ( $\gtrsim 10\,000 M_\odot$ ) objects are mostly stellar associations rather than typical star clusters. However, there are only few of these objects and we did not exclude them from the further analysis.

The colour excess histogram shows a wide distribution (Fig. 4.5b), suggesting that studied clusters are located above, within, or even behind the M 31 disc. The median colour excess of star clusters in our sample is  $E(B-V) = 0.24$ , which is consistent with the value of 0.25 derived for the south-western part of the galaxy (Vansevičius et al. 2009). Seven clusters exhibit high colour excess values,  $E(B-V) > 0.7$  (Fig. 4.5b). Six of these objects, younger than 100 Myr, are located within the star-forming regions of M 31. In some cases, especially for young clusters embedded in strongly inhomogeneous dust clouds, differential extinction (i.e., spatial variations in dust absorption across the cluster) could distort the derived parameters. Fig. 4.6 shows an example of star cluster AP0367, which is located within the star-forming region. It is evident that the cluster is affected by differential extinction, which can be clearly observed in all colour images. It is worth noting that strong differential extinction effects are observed within a relatively small field of view. Moreover, a few older ( $> 100$  Myr) clusters also have enhanced extinction ( $E(B-V) \gtrsim 0.6$ ). This can be attributed to their position

behind a layer of diffuse interstellar matter on the far side of the M 31 disc. We note that  $E(B - V)$  versus projected distance from the M 31 centre does not show any tight correlation.  $E(B - V)$  of an individual cluster seems to be more strongly dependent on the local interstellar matter environment than on the radial distance from the M 31 centre.

Moreover, as noted by Čeponis et al. (2024), differential extinction affecting individual cluster stars is not yet resolved or properly accounted for. In some extreme cases, this could distort the estimated cluster parameters. Also, deviations of the M 31 extinction law (Wang et al. 2025) from the standard Milky Way's law ( $R_V = 3.1$ ), which is assumed in this study, could significantly alter the derived cluster parameters.

## 4.4 Cluster mass function

The observed cluster mass function, i.e. a power-law with an exponential cut-off at the high mass end, is reasonably well-represented by Schechter mass function (Schechter 1976; Gieles 2009):

$$\frac{dN}{dM_i} = AM_i^{-\alpha} \exp\left(-\frac{M_i}{M_C}\right), \quad (4.3)$$

where  $M_C$  – the characteristic mass where the exponential decline occurs,  $A$  – a scaling constant proportional to the cluster formation rate, and  $\alpha$  corresponds to the power-law slope that determines the relative abundance of low-mass clusters. Krumholz et al. (2019) demonstrated that CMF is best parametrised by a power-law slope of  $\alpha = 2 \pm 0.2$ . Therefore, an index of 2 was selected, as this form is also supported by numerous studies (Zhang & Fall 1999; Gieles et al. 2006; Larsen 2009; Portegies Zwart et al. 2010; Fall & Chandar 2012). This value is likely set by the organisation of the interstellar medium shaped by turbulence (Fujii & Portegies Zwart 2015) and the efficiency of cluster formation (Renaud 2018).

To have a better understanding about the origins of the characteristic mass,  $M_C$ , several theoretical models have been proposed (see Adamo et al. 2020). Kruijssen (2014) suggested that the maximum mass of molecular cloud and the characteristic star cluster mass might share a common origin, potentially corresponding to the Toomre mass. This mass-scale parameter represents the maximum mass below which the self-gravity of GMCs can overcome the effects of galactic differential rotation in an equilibrium disc (Toomre 1964; Kruijssen 2014). The proposed model was further refined by Reina-Campos & Kruijssen (2017), who incorporated the effects of stellar feedback. In their model, if the feedback timescale (i.e., the time required for young stars to disrupt their natal gas cloud) is shorter than the free-fall time of the shear-limited region, then the resulting collapsed mass will be lower than the theoretical Toomre mass. A shear-limited region is one where the galactic shear (caused by the rotation of the galaxy) prevents the molecular cloud from collapsing under its own gravity unless the cloud is massive enough to overcome this shear. Proposed model that combines shear and feedback regulation successfully explains observed trend of maximum GMC mass, maximum cluster mass as a function of galactocentric distance in M 31, the radial decline observed in M 83 (Adamo et al. 2015; Freeman et al. 2017), and relatively flat radial profile seen in M 51 (Messa et al. 2018). Therefore,  $M_C$  likely results from a combination of factors, including the Toomre mass, galactic

shear, and stellar feedback, which together regulate the formation and maximum mass of molecular clouds.

In order to derive global  $M_C$  value for the M 31 galaxy, we selected objects more massive than  $\sim 2500 \text{ M}_\odot$  and fitted the Schechter function (Fig. 4.7). The decrease in the number of clusters in the low-mass range is likely not physical, but rather arises from selection effects. In contrast, the decrease observed in the high-mass range is expected to be real. Our results indicate a turnover mass of  $M_C = (13.3^{+1.3}_{-2.6}) \cdot 10^3 \text{ M}_\odot$ . This result is larger than the value obtained by Johnson et al. (2017), who reported  $M_C = (8.5^{+2.8}_{-1.8}) \cdot 10^3 \text{ M}_\odot$ . Nevertheless, our result supports their conclusion regarding the truncated nature of the M 31 cluster mass function derived for young ( $\leq 300$  Myr) star clusters. The difference of the  $M_C$  values may arise due to differences in cluster ages of studied samples – in the present study we use older clusters ( $\leq 800$  Myr). To verify this assumption, we derived  $M_C$  for a subsample of younger clusters ( $\leq 300$  Myr),  $M_C = (12.3^{+2.4}_{-1.9}) \cdot 10^3 \text{ M}_\odot$  (Fig. 4.8). Therefore, only a small difference ( $< 1.5\sigma$ ) in  $M_C$  remains compared to the value derived by Johnson et al. (2017). In addition, our derived  $M_C$  value is among the lowest reported to date. Previous studies, based on extragalactic systems other than M 31, have found  $M_C$  values ranging from  $0.5 \cdot 10^5 \text{ M}_\odot$  to  $10 \cdot 10^5 \text{ M}_\odot$  (Krijssen 2014). However, it is worth noting that low-mass clusters in galaxies other than M 31 may not be detected with high completeness.

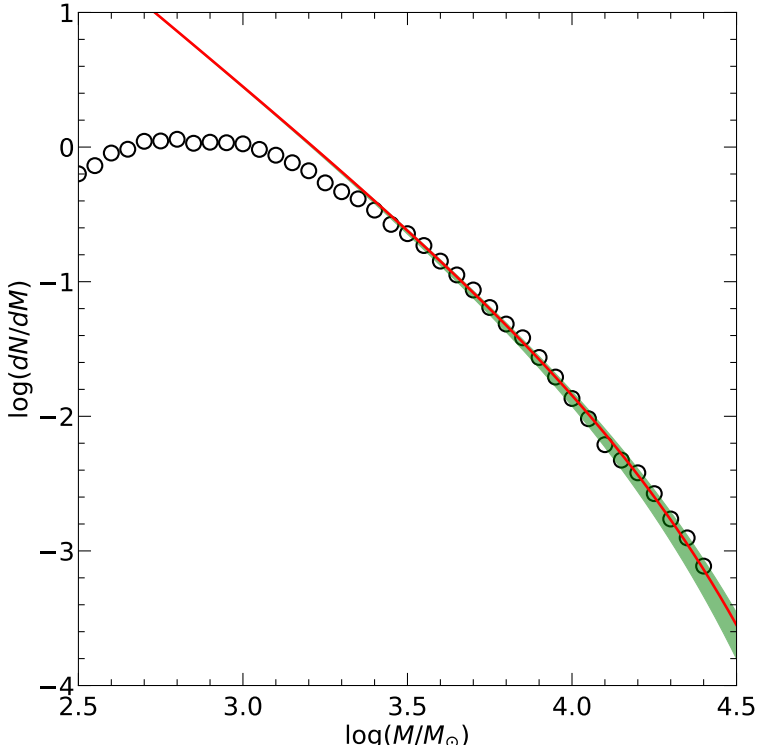


**Figure 4.7.** Differential distribution of cluster masses per mass interval. The solid red line shows the Schechter function fitted to the present cluster sample, with a turnover mass of  $M_C = (13.3^{+1.3}_{-2.6}) \cdot 10^3 \text{ M}_\odot$ . A green shaded area denotes the uncertainty region of the fitted function.

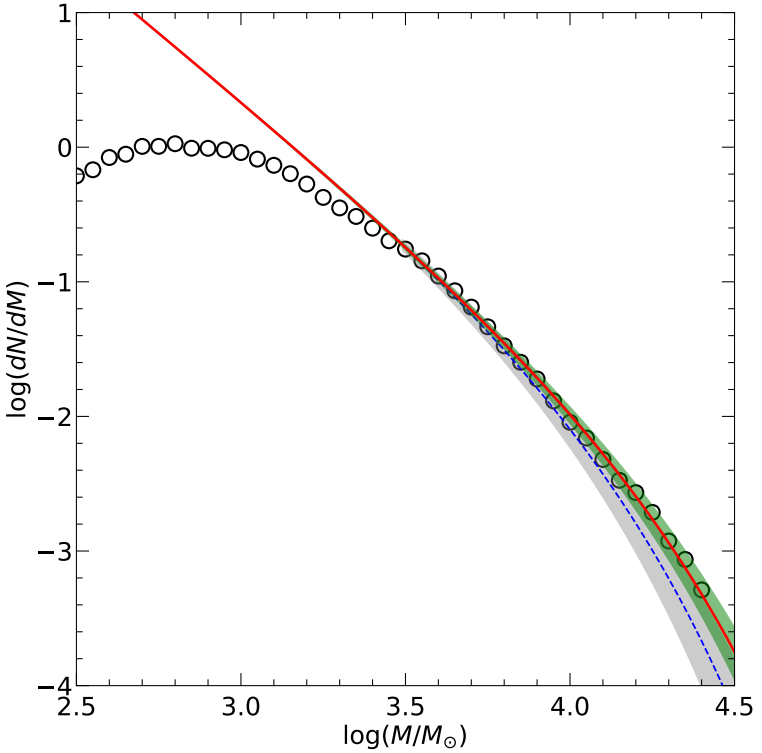


**Figure 4.8.** Same as Fig. 4.7, but for young clusters ( $\leq 300$  Myr). The solid red line shows the Schechter function with  $M_C = (12.3^{+2.4}) \cdot 10^3 M_{\odot}$ . A blue dashed line indicates the case of  $M_C = (8.5^{+2.8}) \cdot 10^3 M_{\odot}$ , with the grey shaded shaded area indicating the uncertainty region (Johnson et al. 2017).

By studying the star cluster population in M 31, we can also investigate the properties of the CMF in a galaxy with low average star formation rate (Barmby et al. 2006; Johnson et al. 2017) and explore how it varies across different environments. Previous studies have primarily focused on galaxies with moderate star formation activity, such as M 51 and M 83 (Gieles 2009; Adamo et al. 2015), or on intense starburst mergers like the Antennae (Zhang & Fall 1999; Whitmore et al. 2010). Therefore, to explore radial variations in  $M_C$  values, we fitted the Schechter function within a set of overlapping radial bins. Each bin (annulus) had a fixed width of 4 kpc, with successive bin offset by 2 kpc, covering galactocentric distances from 4 to 20 kpc. As suggested by Daugevičius et al. (2025), careful consideration of catalogue completeness is essential when investigating the radial or environmental dependencies of the CMF. To ensure a robust analysis, we limited our sample to clusters more massive than  $\sim 2500 M_{\odot}$  and fitted the Schechter function (Eq. 4.3) within each bin (Fig. 4.9).

The resulting  $M_C$  values reveal that the characteristic mass is shaped by the local galactic environment (Fig. 4.10). This environmental effect is consistent with observations in other galaxies, such as M 83, where Adamo et al. (2015) demonstrated that variations in gas density can affect the upper mass limit of the CMF. The region between 10-14 kpc is characterized by higher gas densities due to star-forming ring in that area, which may account for elevated  $M_C$  values. In contrast, weaker disruptive

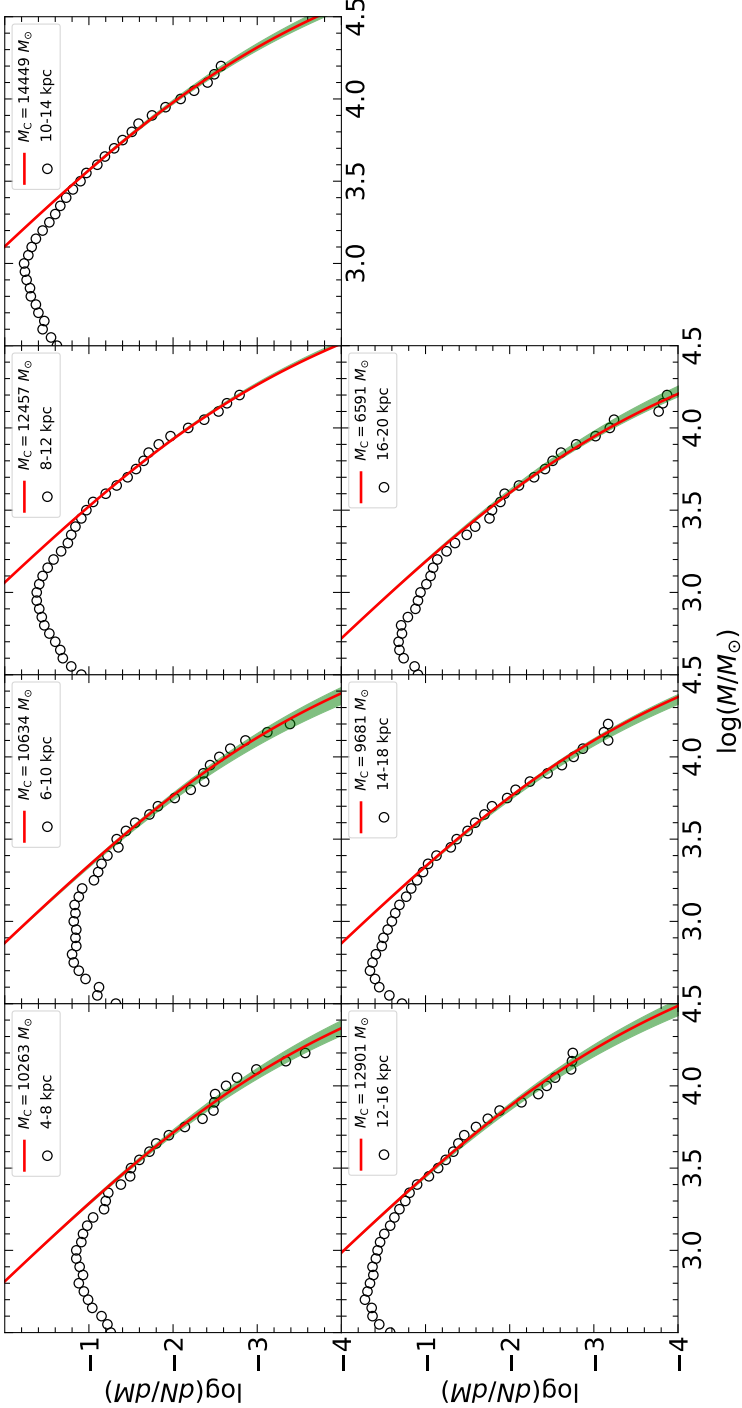


**Figure 4.9.** Differential distributions of cluster masses per mass interval for each analysed radial segment of 4 kpc width. The solid red lines show the Schechter function fitted to the differential distributions of cluster masses. The  $M_C$  values for each segment are provided in the legend. A green shaded area denotes the uncertainty region of the fitted function.

forces in the outer regions allow lower mass clusters to survive longer, potentially contributing to the lower observed  $M_C$  value in the 16-20 kpc segment. It has also been suggested that the  $M_C$  varies with the galactic environment on a global scale, with higher  $M_C$  values observed in galaxies undergoing elevated star formation activity (Adamo et al. 2020), such as the Antennae galaxies (Larsen 2009), reinforcing the idea that interstellar medium pressure may be a key driver of variations in the characteristic mass. Furthermore, Johnson et al. (2017) have demonstrated that there is a systematic correlation between the truncation mass of the CMF and the star formation environment, quantified by the star formation rate surface density ( $\Sigma_{SFR}$ ). The  $M_C$  increases with star formation intensity, following the scaling relation  $M_C \propto \langle \Sigma_{SFR} \rangle^{-1.1}$ .

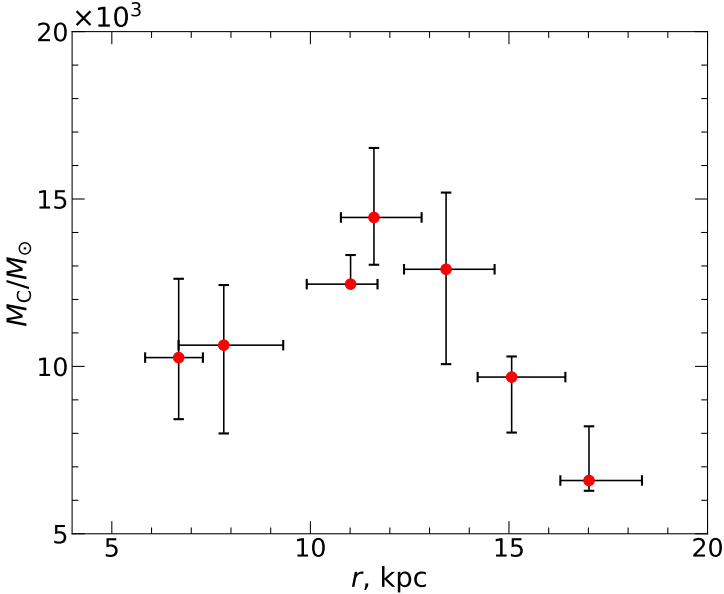


**Figure 4.10.** The characteristic mass ( $M_C/M_\odot$ ) of star clusters versus radial distance from the centre of M 31. The Y-axis values are scaled by  $10^3$ . Vertical error bars represent min-max limits of the fitted  $M_C$  values. Horizontal error bars mark 16th-84th percentile ranges. In each case, the mass function was fitted using data from overlapping annuli of 4 kpc width, with a step of 2 kpc, covering a range from 4 to 20 kpc (see Fig. 4.9).

In Fig. 4.11, we illustrate the number of clusters per 0.2 dex mass interval as a function of mass. We grouped clusters into three radial bins (4-7 kpc, 9-12 kpc, 14-17 kpc) and plotted their distribution for different age intervals. The 9-12 kpc region shows the highest cluster counts in the age interval of 100-300 Myr. This is expected as the 11 kpc star-forming ring is the main site of recent and ongoing cluster formation. The inner 4-7 kpc region shows the lowest cluster numbers and relatively broad distribution, indicating suppressed formation activity or enhanced disruption and extinction. In the outer 14-17 kpc region, 100-300 Myr cluster population exhibits a bimodal pattern with two peaks at  $\sim 500 M_\odot$  and  $\sim 1300 M_\odot$ . This bimodal distribution may result from various factors, such as cluster fading, disruption effects, and selection biases. Also, at this age, the 16 kpc ring partially merges with the 11 kpc

ring (see Section 4.6) in the azimuthal segment from  $45^\circ$  to  $90^\circ$ . Therefore, the second peak could be affected by more massive clusters originating from the 11 kpc ring. These trends point a clear radial dependence in the cluster population, shaped by both star formation history and environmental effects across the disc of M 31.

## 4.5 Cluster formation history

If star clusters form continuously at a constant rate and follow a power-law of cluster initial mass function, the number of clusters should increase over time in a mass-age diagram. As a result, the most massive clusters in older logarithmic age bins should appear more massive due to a statistical sampling effect. However, our data show a noticeable absence of massive clusters with  $\log_{10}(M/M_\odot) > 4$  (Fig. 4.5a), suggesting that the cluster formation history may not have been constant. To investigate this further, we analyse the observed distribution of cluster age to estimate their formation and disruption rates, applying the method outlined by Boutloukos & Lamers (2003).

The differential age distribution of clusters is displayed in Fig. 4.12. We used objects more massive than  $1000 M_\odot$  in order to mitigate uneven selection effects over a wide range of considered ages. The age distribution is reasonably well represented by an evolutionary fading and disruption lines. The first slope is interpreted as the natural fading of magnitudes caused by stellar evolution, while the second slope reflects cluster disruption due to the galaxy tidal field or interactions with giant molecular clouds. We used the evolutionary fading and disruption equations proposed by Boutloukos & Lamers (2003), which are defined as  $\zeta(1 - \alpha)$  and  $(1 - \alpha)/\gamma$ , respectively. The parameters were taken from Vansevičius et al. (2009):  $\alpha = 2.0$ ,  $\zeta = 0.69$ ,  $\gamma = 0.62$ , and only vertical adjustment to the observed distribution was applied. In this context,  $\alpha$  is the slope value of the cluster initial mass function  $N(M) \propto M^{-\alpha}$ , while  $\zeta$  and  $\gamma$  represent the slopes from cluster evolution and disruption models, respectively.

The cluster number distribution,  $dN/dt$  (Fig. 4.12), in general follows the evolutionary fading line, indicating that cluster formation rate (CFR) over the last  $\sim 100$  Myr was rather constant. Adamo et al. (2015) emphasized that in most observational studies the age function of clusters shows nearly constant age distribution before  $\sim 100$  Myr and a drastic decrease above this age due to combination of cluster disruption and sample incompleteness. They also noted that this agrees with theoretical expectations, which rule out rapid cluster disruption for ages younger than 100 Myr in most galaxies. On the other hand, around ages of  $\sim 300$  Myr, the effects of cluster disruption become dominant (Boutloukos & Lamers 2003; Fouesneau et al. 2014; Johnson et al. 2017).

Around 130 Myr, the number of clusters increases, likely reflecting a higher CFR at that epoch. The decline in differential cluster number distribution at ages older than 300 Myr (Fig. 4.12) suggests that the characteristic cluster disruption time in the north-eastern part of the M 31 disc might be larger than 500 Myr. This finding is broadly consistent with studies by Vansevičius et al. (2009); de Meulenaer et al. (2017). However, because of the enhanced cluster formation and disruption at these ages, the time when cluster disruption starts to dominate over fading can be estimated only roughly. For comparison, Lamers et al. (2005) reported the following characteristic disruption timescales in other galaxies:  $\sim 70$  Myr in the central region of M 51,  $\sim 630$  Myr in M 33,  $\sim 560$  Myr in the MW solar neighbourhood, and  $\sim 8$  Gyr in the Small Magellanic Cloud.

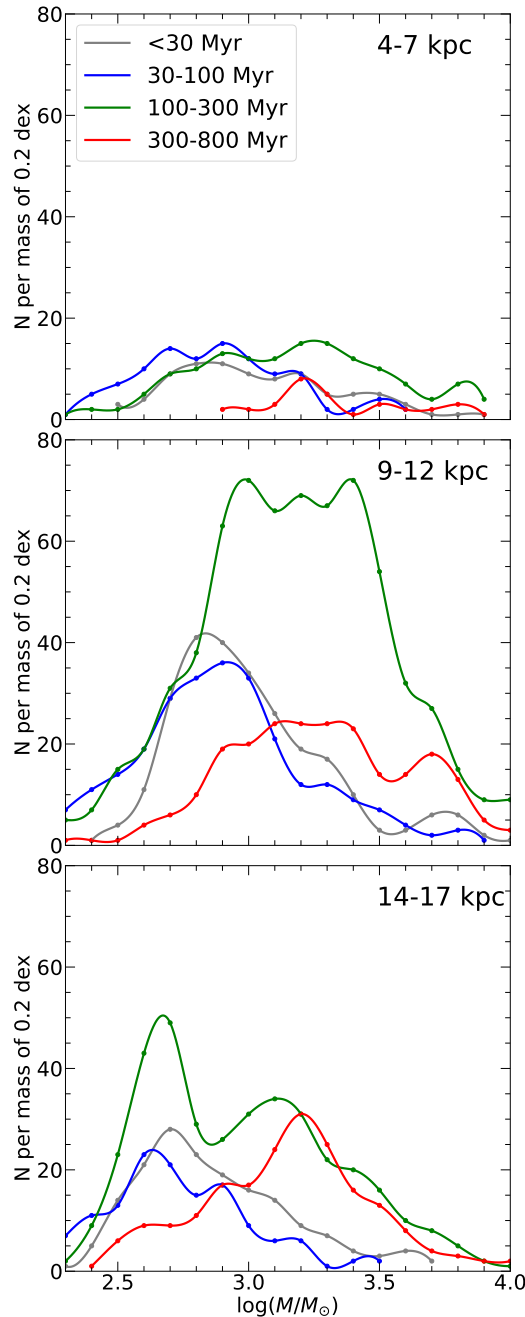


**Figure 4.11.** Number of clusters per 0.2 dex mass interval as a function of mass. From top to bottom, we analysed star clusters within the radial intervals of 4-7 kpc, 9-12 kpc, and 14-17 kpc.

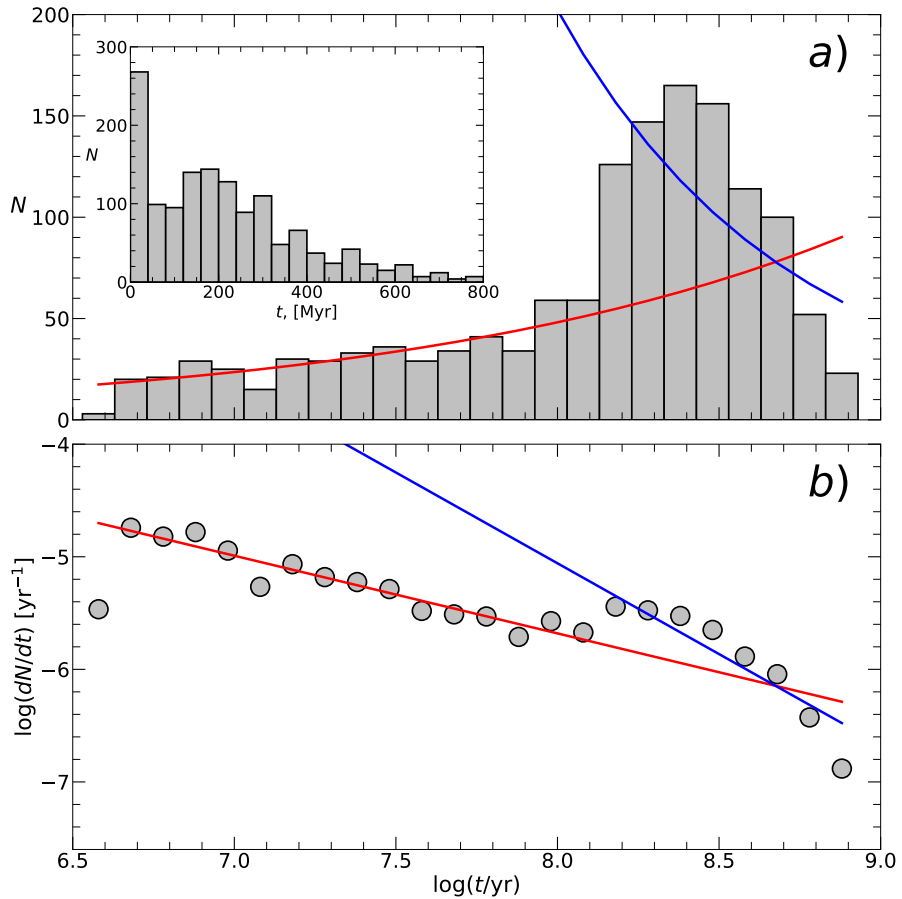


**Figure 4.12.** Top: the distribution of the derived ages of clusters more massive than  $1000 M_{\odot}$ . The inset shows the same cluster distribution versus the linear age scale (on X-axis). Bottom: the differential age distribution of cluster ages (the same sample as above). In both panels, the red and blue lines show the cluster evolutionary fading and disruption functions, respectively. The parameters of lines are taken from Vansevičius et al. (2009).

A notable feature in the cluster age distribution is a peak at  $\sim 200$  Myr, indicating an episode ( $\sim 150$ - $250$  Myr) of enhanced CFR. This episode could have been triggered by an encounter with the M 32 galaxy (Gordon et al. 2006; Block et al. 2006; Dierickx et al. 2014). Gordon et al. (2006) and Dierickx et al. (2014) proposed that the collision happened  $\sim 20$  Myr and  $\sim 800$  Myr ago, respectively. However, Block et al. (2006) suggested that M 32 passed through the centre of M 31 about 210 Myr ago, leading to the formation of the ring- and spiral-like structures observed in the disc. Additionally, Vansevičius et al. (2009) found a prominent peak of cluster formation in the south-western part  $\sim 70$  Myr ago, which could have been triggered by the secondary passage of M 32 in this scenario. Furthermore, studies by Lewis et al. (2015) and Williams et al. (2017) suggest that ring structure is long-lived, older than  $\sim 500$  Myr, implying

that its origin cannot be explained solely by a recent impact event. Following Lewis et al. (2015), who proposed that morphological features observed in the M 31 disc might be the result from a combination of collision event and resonance rings due to rotating bar (see Section 4.6), we suggest that CFR enhancement  $\sim$ 200 Myr ago could still have been triggered by an interaction with M 32, according to the scenario similar to that proposed by Block et al. (2006), while ring-like structure was already present by the time of collision. We expect that future analyses of PHAST survey (Chen et al. 2025) will provide further insights into whether M 32 was indeed responsible for the elevated CFR.

## 4.6 Spatial distribution

We applied a positional angle (from north to east) of the major axis of  $37.7^\circ$  (Chemin et al. 2009) and an inclination of the disc of  $77.5^\circ$  (van der Marel et al. 2019) to deproject the M 31 disc. The radial profile of star cluster surface number density is shown in Fig. 4.13. It is calculated for four age groups within the azimuthal segment of  $60^\circ$  (from  $-25^\circ$  to  $+35^\circ$  around the major axis). The azimuthal range is limited due to the narrow PHAT survey mapping and our attempt to have a complete coverage of the observed field up to a  $\sim$ 20 kpc distance. The present-day star-forming rings are located at radial distances of  $\sim$ 6 kpc,  $\sim$ 11 kpc, and  $\sim$ 16 kpc from the galaxy's centre, as estimated from the radial distribution of massive ( $\geq 1000 M_\odot$ ) star clusters (Fig. 4.13). The outer 16 kpc ring appears to partially merge with the 11 kpc ring (Figs. 4.14, 4.15), likely due to a combination of projection effects and the presence of a warp in the disc, as observed in HI studies (Brinks & Burton 1984; Chemin et al. 2009). In addition, the peak of 11 kpc ring is consistent with De Somma et al. (2025), who confirmed the presence of the well-known ring at  $\sim$ 11 kpc through observations of Classical Cepheids. Moreover, we find that the star-forming ring at 16 kpc is visible only as a concentration of younger ( $< 40$  Myr) clusters. Number densities of older cluster populations are  $\sim$ 4 times lower, indicating that stronger cluster formation in the 16 kpc ring was induced only recently (Figs. 4.13 and 4.14a). This region, with elevated CFR compared to its surroundings, was also identified as OB 102 by Efremov et al. (1987); Williams (2003).

Possible explanations for the formation of the 11 kpc ring are extensively discussed in Block et al. (2006); Gordon et al. (2006); Dierickx et al. (2014); Lewis et al. (2015), and can be broadly classified into two main scenarios: (i) a resonance ring induced by the presence of a central bar, or (ii) a collisional ring formed as a result of satellite galaxy passing through the disc of M 31. There is evidence supporting the presence of a bar in M 31, as indicated by its boxy bulge observed in infrared imaging (Athanassoula & Beaton 2006; Beaton et al. 2007). However, if the 11 kpc ring is associated with a bar, it is unlikely to be a nuclear or inner ring, which typically form within the bar or at the end of it, respectively. If the ring is a consequence of bar dynamics, it would most likely be an outer ring formed near the outer Lindblad resonance (OLR), which occurs when the orbital frequency of stars or gas in the disc resonates with the pattern speed of a bar or spiral density wave (Binney & Tremaine 2008). This interaction can lead to orbital crowding and the accumulation of gas, often resulting in the formation of ring-like structures. Athanassoula & Beaton (2006) demonstrated that, based on comparisons between observations of M 31 and *N*-body simulations, the OLR lies at  $\sim 45 \pm 4$  arcmin, which corresponds to  $\sim$ 10 kpc at the dis-

tance of M 31. The main disadvantage of this scenario is that bar-driven framework alone cannot reproduce features such as the offset centres of the 6, 11 kpc rings, and the central hole in the 11 kpc ring (Lewis et al. 2015).

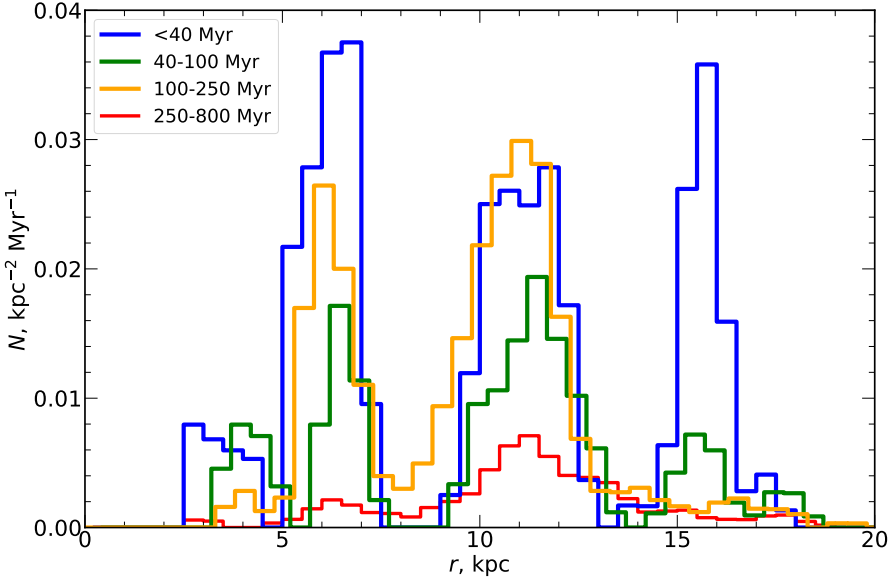


**Figure 4.13.** The radial profiles of surface number density (calculated per Myr) for massive ( $\geq 1000 M_{\odot}$ ) star clusters in four age ranges within the azimuthal segment of  $60^{\circ}$  (from  $-25^{\circ}$  to  $+35^{\circ}$ ). Some histograms are slightly offset along the X-axis for visual clarity. The age ranges of the cluster groups are indicated in the legend.

Another widely discussed scenario is that the ring formed as a result of past interaction with the satellite galaxy M 32. While nearly circular in shape, the ring shows a clear split near the location of M 32. Additionally, the spiral structure of M 31 appears weak and fragmented, suggesting that it may have been shaped by external perturbations rather than internal processes. Block et al. (2006) and Gordon et al. (2006) performed dynamical simulations to investigate whether a close passage of M 32 through M 31 disc could have triggered the formation of the ring. Modelling results demonstrated that such encounter could produce a density wave, compressing gas into a ring-like structure and triggering star formation at a radius of  $\sim 10$  kpc. Also, Block et al. (2006) and Gordon et al. (2006) successfully reproduced both the offset and the observed split in the ring, providing strong support for the hypothesis that M 32 gravitational influence was a key factor. However, such collisional models face significant uncertainties, especially in the mass and orbital parameters of M 32, both of which play a crucial role in shaping the interaction and the resulting morphology. Furthermore, Williams et al. (2015) identified that recent major event of star formation in M 31 occurred 2-4 Gyr ago. These ages exceed the timescales proposed by Gordon et al. (2006) and Block et al. (2006). Therefore, it remains possible that the observed ring morphology results from a combination of both scenarios. A more detailed understanding is required to further investigate the 11 kpc ring origins. The next step would be to perform simulations capable of following the ring's formation and

evolution over timescales of at least few Gyrs. These simulations should include scenarios such as: satellite-induced collision, bar-driven resonances, and possible hybrid interactions between the two.

The origin of the 16 kpc ring remains uncertain, as no current models have attempted to account for the presence of this ring. The offset ring could be formed due to internal resonances, which can produce three different types of rings: nuclear, inner, and outer. It could also be linked to the outer Lindblad resonance or corotation radius. Specifically, the OLR lies beyond the corotation radius and is commonly associated with the formation of outer rings. The corotation radius marks the location where angular velocity of the stars or gas matches the pattern speed of the spiral arms or bar. At this radius, material co-rotates with the spiral pattern, which can significantly influence the distribution of gas and star formation (Braun 1991; Binney & Tremaine 2008).

In Figs. 4.14, 4.15 we show the spatial distribution of star clusters in six age intervals. Each cluster is represented as a 2D Gaussian, where  $\sigma = 0.1$  kpc is used for clusters with half-light radii up to  $1''$ . For clusters with larger half-light radii,  $\sigma$  is scaled proportionally by multiplying fixed  $\sigma$  value by the half-light radius. The intensity of each Gaussian is scaled by the cluster mass and normalized within each panel. Our results show that young clusters ( $\leq 170$  Myr) are located in narrower star-forming rings compared to older cluster population ( $> 170$  Myr). This suggests that clusters initially form in dense star-forming regions and gradually disperse into the galaxy. In the 6 kpc ring, star formation was active for 170 Myr, after which the ring feature started to dissipate. If we assume a rotational velocity of 220 km/s at the 6 kpc ring in M 31 (Chemin et al. 2009), and we define the dynamical time at a given radius as:  $t_{\text{dyn}} = 2\pi r/v_r$ , the resulting dynamical timescale at this radius is  $\sim 170$  Myr. Therefore, it takes approximately one dynamical timescale for clusters to disperse from the inner M 31 ring. In contrast, the 11 kpc ring is long-lived and relatively stationary, producing stars over the past 400 Myr. This implies that star formation within the ring has persisted for at least 1.5 dynamical times. In addition, Dalcanton et al. (2012) reported an over-density of stars older than 1 Gyr within the ring, further supporting the long-lived nature of this structure.

By analysing the spatial distribution of younger and older cluster populations within the 11 kpc star-forming ring, we estimated an upper limit for the radial spread of cluster groups to be less than 0.5 kpc over  $\sim 400$  Myr. This corresponds to a radial velocity dispersion of less than  $\sim 2$  km/s, which is substantially lower than average stellar random velocity of 10 km/s (Lewis et al. 2015). Thus, we have low velocity dispersion for cluster groups relative to their birthplaces, implying that the actual radial velocities and the dispersal timescales must be much lower and longer, respectively. Consequently, star clusters serve as highly reliable long-lasting tracers of star-forming region morphology in disc galaxies.

Additionally, Fig. 4.15 shows that older clusters ( $> 400$  Myr) exhibit a more spread-out distribution. This could be due to: (i) star formation within the ring becoming increasingly concentrated over time, occurring in a narrower region that likely follows the distribution of gas within the ring; or (ii) star formation consistently occurring near the centre of the ring, and the observed broadening at older ages reflecting the subsequent dispersion of stars. The latter explanation is more likely, given that most stars form in clusters which eventually disperse into the surrounding environment, contributing to the broader stellar background (Bastian et al. 2009; Lewis et al. 2015).

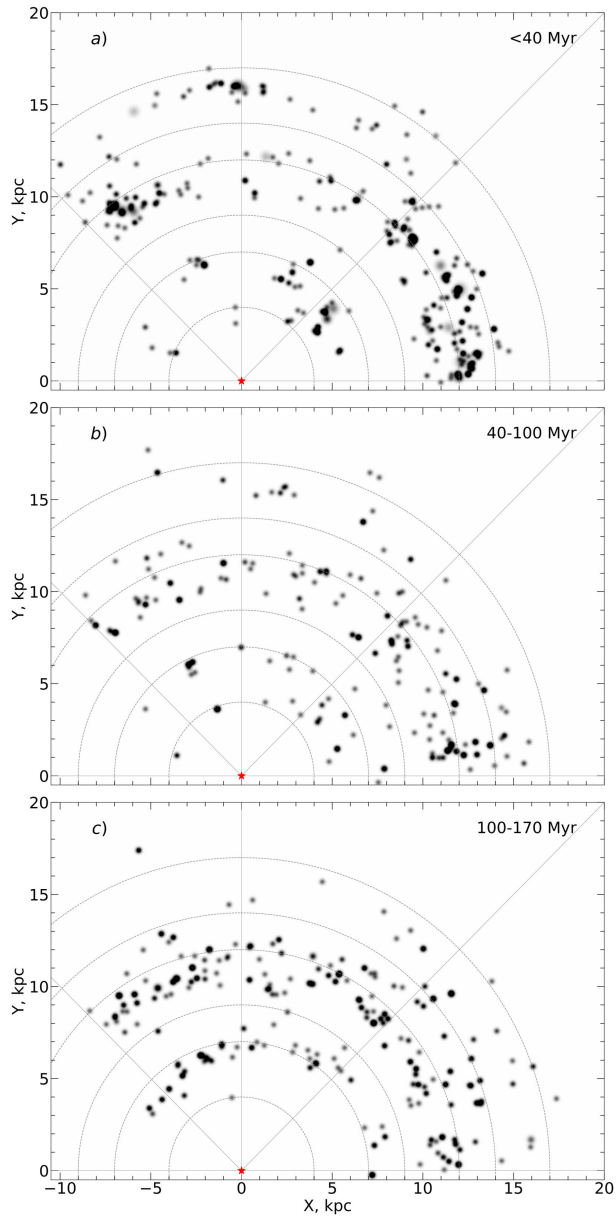


**Figure 4.14.** Deprojected positions of massive ( $\geq 1000 M_{\odot}$ ) star clusters in the galaxy disc. The vertical coordinate at  $X = 0$  corresponds to the major axis of M 31. Clusters located in the disc part closer to us have negative X coordinates, clusters residing on the more distant disc part – positive X coordinates. The circles indicate 4, 7, 9, 12, 14, and 17 kpc distances from the galaxy centre.

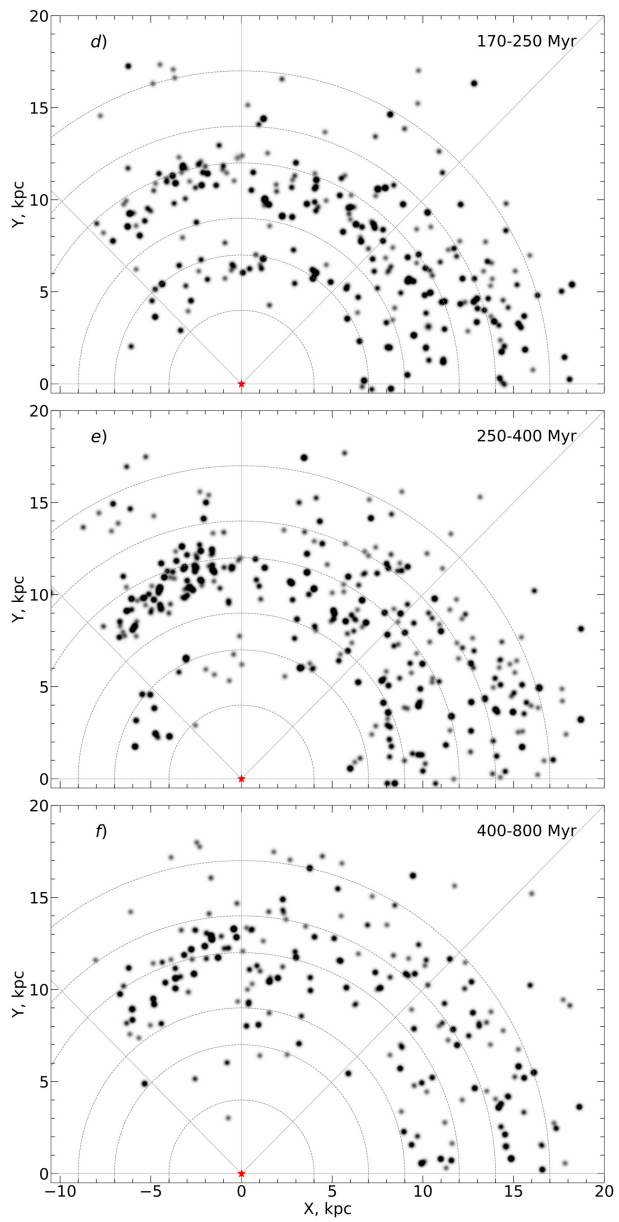


**Figure 4.15.** Continuation of the map from Figure 4.14.

Notably, the CFR has also decreased significantly in the azimuthal segment from  $45^\circ$  to  $90^\circ$ , as the number of clusters in this segment is lower compared to younger intervals. In contrast, the azimuthal segment from  $-45^\circ$  to  $0^\circ$  contains a higher number of star clusters, even after 400 Myr. Meanwhile, in the inner disc of M 31, we observe less older clusters (Fig. 4.15), suggesting either lower formation rates or higher disruption rates.

## 4.7 Structural cluster parameters

We derived the half-light radius,  $R_{50}$ , and  $R_{30}$ ,  $R_{80}$  parameters from growth curves in the  $F475W$  passband for all 1922 studied clusters. The  $R_{50}$  of clusters is plotted versus age,  $\log_{10}(t/\text{yr})$ , in Fig. 4.16a. The  $R_{50}$  values, ranging from  $\sim 0.4$  pc to  $\sim 8$  pc, are distributed across a wide age range, showing no clear evolution of the  $R_{50}$  with cluster age. The decline of small-size clusters with increasing age can be attributed to the selection effects. In contrast, large ( $R_{50} > 5$  pc) and young ( $\log_{10}(t/\text{yr}) < 7.5$ ) objects are stellar associations.

The  $R_{50}$  of clusters versus their mass,  $\log_{10}(M/M_\odot)$ , is shown in Fig. 4.16b, overplotted with seven lines of constant half-mass density,  $\rho_{50} = 3M/8\pi R_{50}^3$ , ranging from 1 to  $10^4 M_\odot \text{ pc}^{-3}$ . The majority of PHAT clusters in the north-eastern field of M 31 are compact ( $R_{50} \sim 1.7$  pc), dense ( $\rho_{50} \sim 30 M_\odot \text{ pc}^{-3}$ ), and of intermediate mass ( $M \sim 1500 M_\odot$ ). Characteristic cluster parameter values in the south-western field are  $R_{50} \sim 1.5$  pc,  $M \sim 4000 M_\odot$ ,  $t \sim 100$  Myr (Kodaira et al. 2004; Narbutis et al. 2008; Vansevičius et al. 2009). The characteristic age and mass values of the present sample differ due to a bias in cluster selection: ground-based observations restricted detections to younger and more massive objects, compared to HST data. However, the  $R_{50}$  values remain similar across the M 31 galaxy, suggesting that cluster compactness is inherent across the M 31 galaxy, despite a roughly tenfold difference in the spatial resolution of observations.

In addition, we highlight one particularly interesting cluster (red circle in Fig. 4.16) – AP0226 (other name B380-G313) – which is relatively young ( $t \sim 450$  Myr), large ( $R_{50} \sim 7.1$  pc), and massive ( $M \sim 63\,000 M_\odot$ ). In comparison, Caldwell et al. (2009) derived age and mass estimates for this object of  $t \sim 400$  Myr and  $M \sim 28\,000 M_\odot$ . Although our mass estimates are larger, this confirms the conclusion by Caldwell et al. (2009) that the AP0226 disc cluster is indeed exceptional in being both young and massive (Fig. 4.17).

In Fig. 4.18, we show distributions of clusters in the parameter space of  $R_{50}/R_{80}$  versus  $R_{30}/R_{50}$ , depending on their mass and age. The  $R_{30}/R_{50}$  ratio provides information about the concentration and dominance of the core region in star clusters. The  $R_{50}/R_{80}$  ratio offers insights into the concentration and compactness of the outer regions of the cluster. In most cases, there is significant scatter – clusters cover a wide range of the parameter space without a clear concentration. This feature is prominent for clusters with  $\log_{10}(t/\text{yr}) \leq 8$  throughout the entire mass range. At higher masses ( $M > 10^4 M_\odot$ ), the sample contains only a few young objects. Some young clusters have high  $R$  parameter ratios close to 1.0 in the parameter space of  $R_{50}/R_{80}$  versus  $R_{30}/R_{50}$ . This observation suggests that a single star dominates the clusters' light, as  $R_{30}$ ,  $R_{50}$ , and  $R_{80}$  are nearly equal. Star clusters ( $t > 100$  Myr) in the mass interval  $3.0 < \log_{10}(M/M_\odot) \leq 3.5$  show well-defined and concentrated distribution in the parameter space of  $R_{50}/R_{80}$  versus  $R_{30}/R_{50}$ . This implies that aperture-photometry-

based structural parameters for such clusters can be estimated with a reasonable accuracy (Daugevičius et al. 2024). Furthermore, we compare the centroid positions of observational data (red symbols) with star cluster models (black symbols), which are generated using the prescription presented in Section 3.5. The centroid distribution of observational data in each panel remains consistent regardless of age or mass. However, there are some discrepancies in the  $R_{50}/R_{80}$  parameters, when comparing observational and model centroids. The reason for such difference is that the model clusters were generated without accounting for the sky background and can therefore exhibit overly extended profiles. In contrast, real star clusters have smaller  $R_{80}$  values due to the subtraction of the sky background.

## 4.8 Summary

We used the multicolour Panchromatic Andromeda Treasury (PHAT) survey catalogues (Johnson et al. 2015; Naujalis et al. 2021; Kriščiūnas et al. 2023) to derive parameters (age, mass, and colour excess) for 1922 star clusters younger than 800 Myr in the M 31 galaxy. A subset of physical parameters for clusters are presented in Table 4.1. The derived parameters are in consistent agreement with those reported in previous studies of the same clusters by Caldwell & Romanowsky (2016); Johnson et al. (2022).

The determined ages of clusters indicate that the cluster formation rate in the M 31 galaxy was rather constant during the last  $\sim$ 130 Myr. However, at least one active star-forming episode occurred  $\sim(200 \pm 50)$  Myr ago. It might have been induced by the passage of the M 32 galaxy through the M 31 disc  $\sim$ 210 Myr ago (Block et al. 2006). In addition, we found that enhanced star cluster formation in the 16 kpc spiral arm occurred only recently ( $<40$  Myr).

We estimated a characteristic mass of the Schechter function to be  $M_C = (13.3^{+1.3}_{-2.6}) \cdot 10^3 M_\odot$ . This value supports the finding of the truncated mass function by Johnson et al. (2017). We have demonstrated that  $M_C$  depends on the local galactic environment.

Younger and older cluster populations remain concentrated in the same regions of the galaxy for extended periods, indicating a relatively slow dispersion from their birthplaces. As a result, clusters are reliable long-lasting tracers of both recent star formation history and the morphology of star-forming regions in disc galaxies.

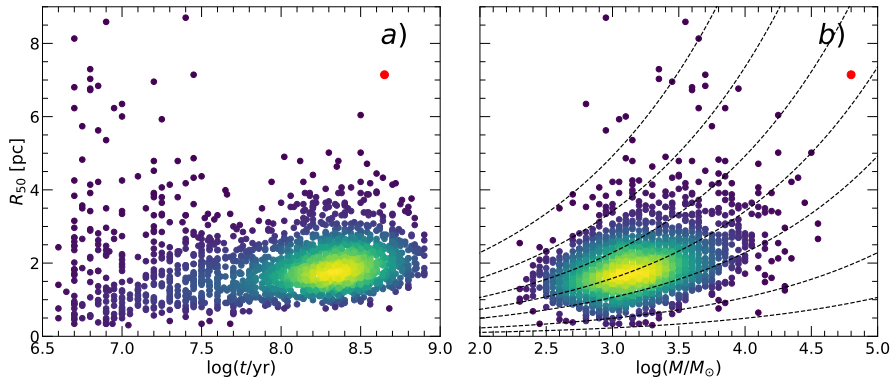


**Figure 4.16.** Panel (a): half-light radius,  $R_{50}$ , plotted versus age,  $\log_{10}(t/\text{yr})$ . Panel (b):  $R_{50}$  is shown versus mass,  $\log_{10}(M/M_\odot)$ , and overplotted with lines of a constant half-mass density,  $\rho_h = 1, 3, 10, 30, 10^2, 10^3, 10^4 M_\odot \text{ pc}^{-3}$ , from top to bottom, respectively. The red circle marks cluster – AP0226. The colours of dots indicate the local point density.

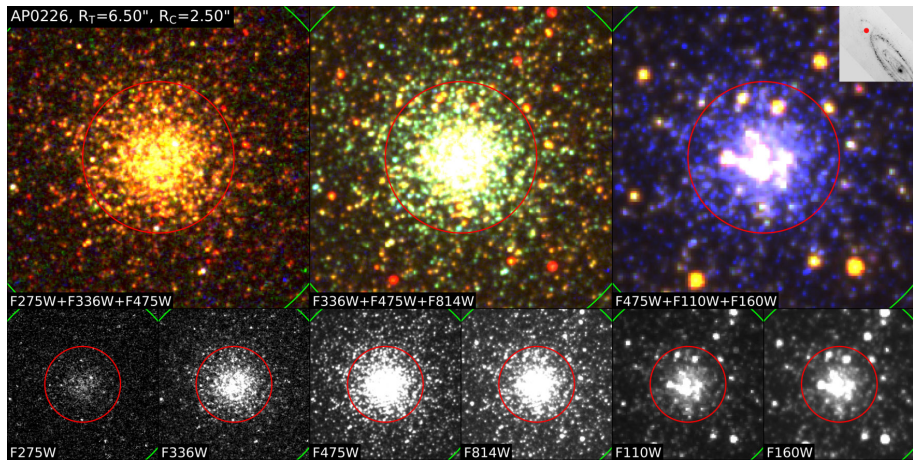


**Figure 4.17.** Same as in Fig. 2.2, but for cluster AP0226 (B380-G313, Caldwell et al. 2009). This object is exceptional due to relatively young age ( $t \sim 450$  Myr), size ( $R_{50} \sim 7.1$  pc), and mass ( $M \sim 63\,000 M_\odot$ ).

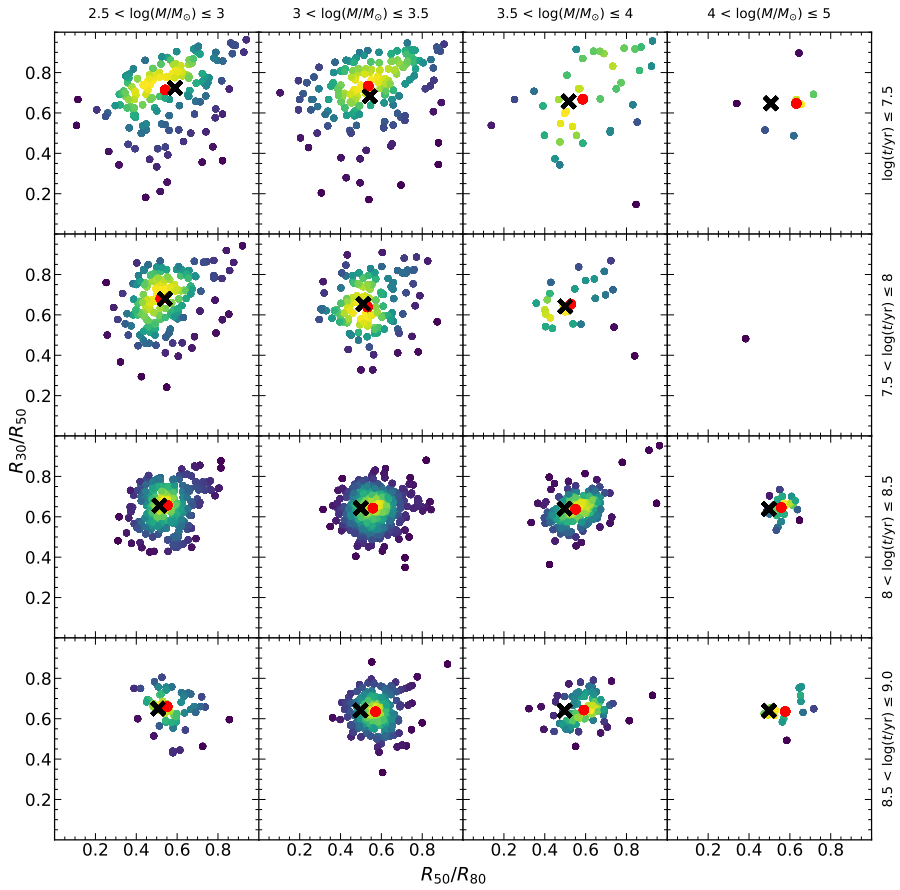


**Figure 4.18.** Star cluster structural parameter,  $R_{50}/R_{80}$  versus  $R_{30}/R_{50}$ , dependency on cluster mass and age. Red symbols represent the centroids of each distribution, while black symbols indicate the centroids of the corresponding cluster models for the same age and mass. In both cases, structural parameters are measured in the  $F475W$  passband. The colours of dots indicate the local point density.

## Appendix: Star cluster parameter derivation examples and excluded objects

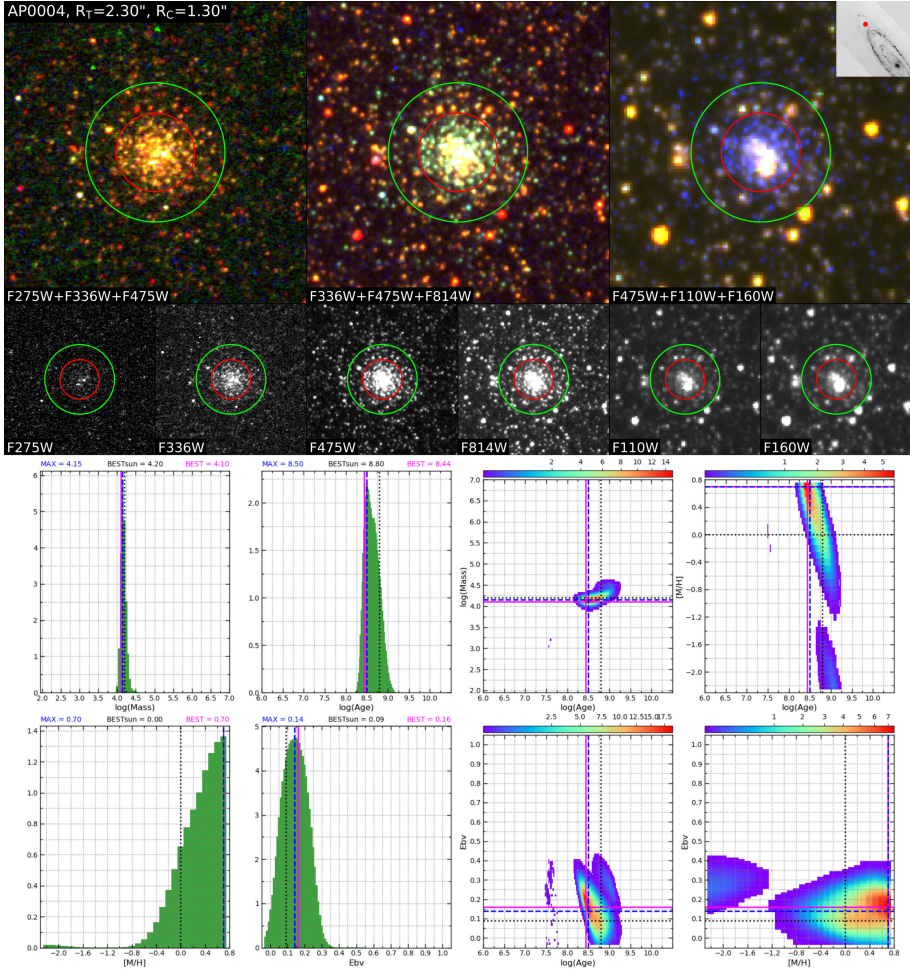


**Figure B1.** Same as in Fig. 4.1, but for cluster AP0004. Derived parameters for the cluster are: age –  $\log_{10}(t/\text{yr}) = 8.78$ , mass –  $\log_{10}(M/M_\odot) = 4.20$ , colour excess –  $E(B - V) = 0.09$ , metallicity –  $[M/H] = 0.0$ . The cluster is located between star-forming rings, making it less contaminated by field stars. For parameter derivation, we selected the C aperture, focusing on the central region of the cluster and excluding several bright stars visible in the  $F814W$ ,  $F110W$ , and  $F160W$  passbands.

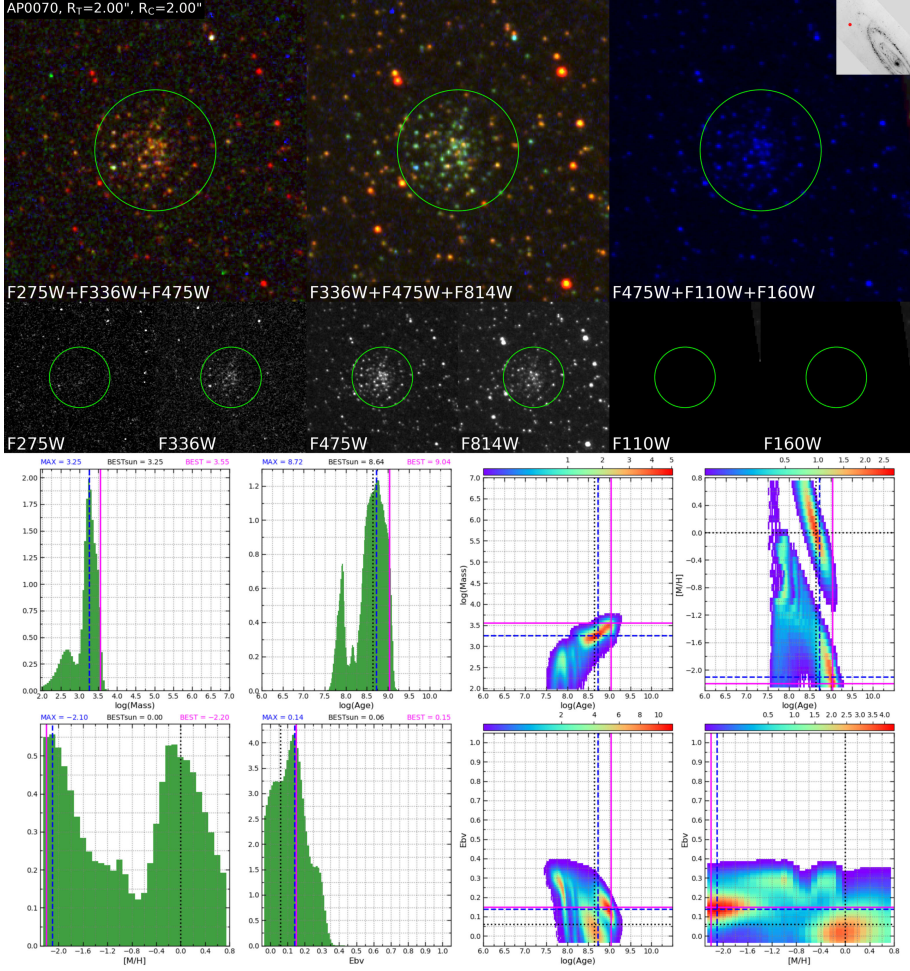


**Figure B2.** Same as in Fig. 4.1, but for cluster AP0070. Derived parameters for the cluster are: age –  $\log_{10}(t/\text{yr}) = 8.64$ , mass –  $\log_{10}(M/M_\odot) = 3.25$ , colour excess –  $E(B - V) = 0.06$ , metallicity –  $[\text{M}/\text{H}] = 0.0$ . The cluster is located on the outskirts of the M 31 galaxy, and there is no available data in the  $F110\text{W}$  and  $F160\text{W}$  passbands. As a result, the C and T apertures are equal in size, yielding consistent parameter estimates.

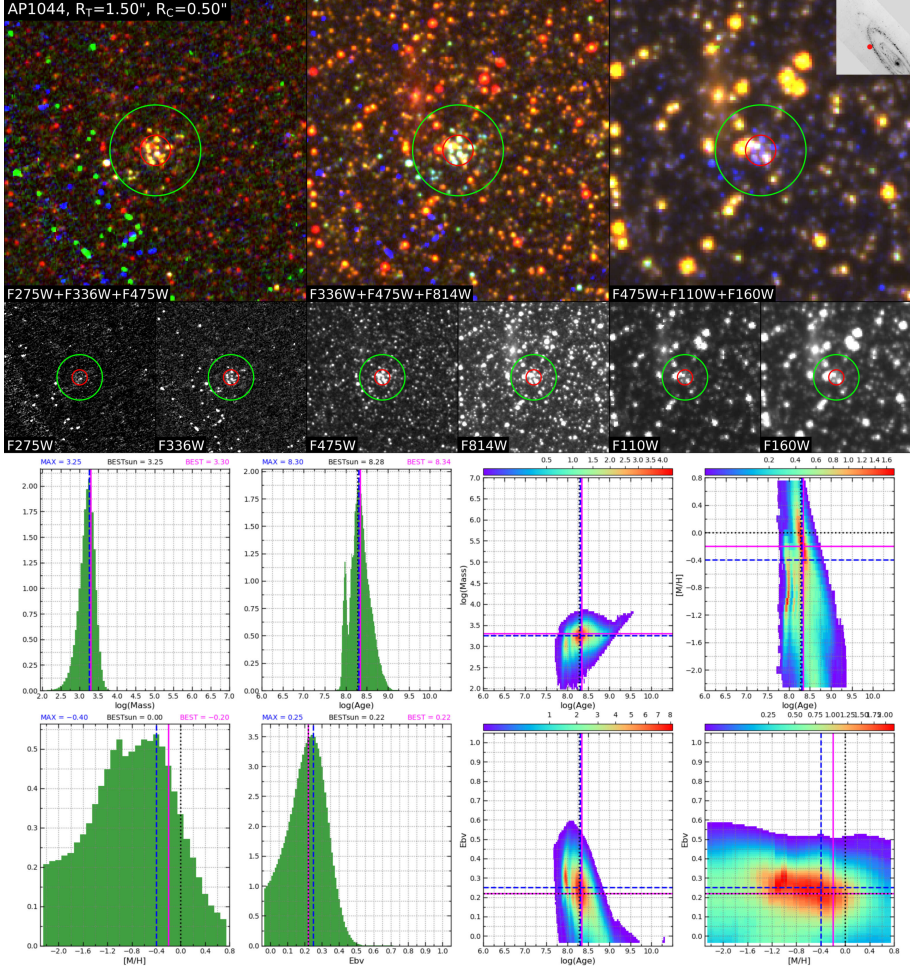


**Figure B3.** Same as in Fig. 4.1, but for cluster AP1044. Derived parameters for the cluster are: age –  $\log_{10}(t/\text{yr}) = 8.28$ , mass –  $\log_{10}(M/M_\odot) = 3.25$ , colour excess –  $E(B-V) = 0.22$ , metallicity –  $[M/H] = 0.0$ . Due to the projection of a bright star onto the T aperture, we opted to use the parameter results derived from the C aperture.

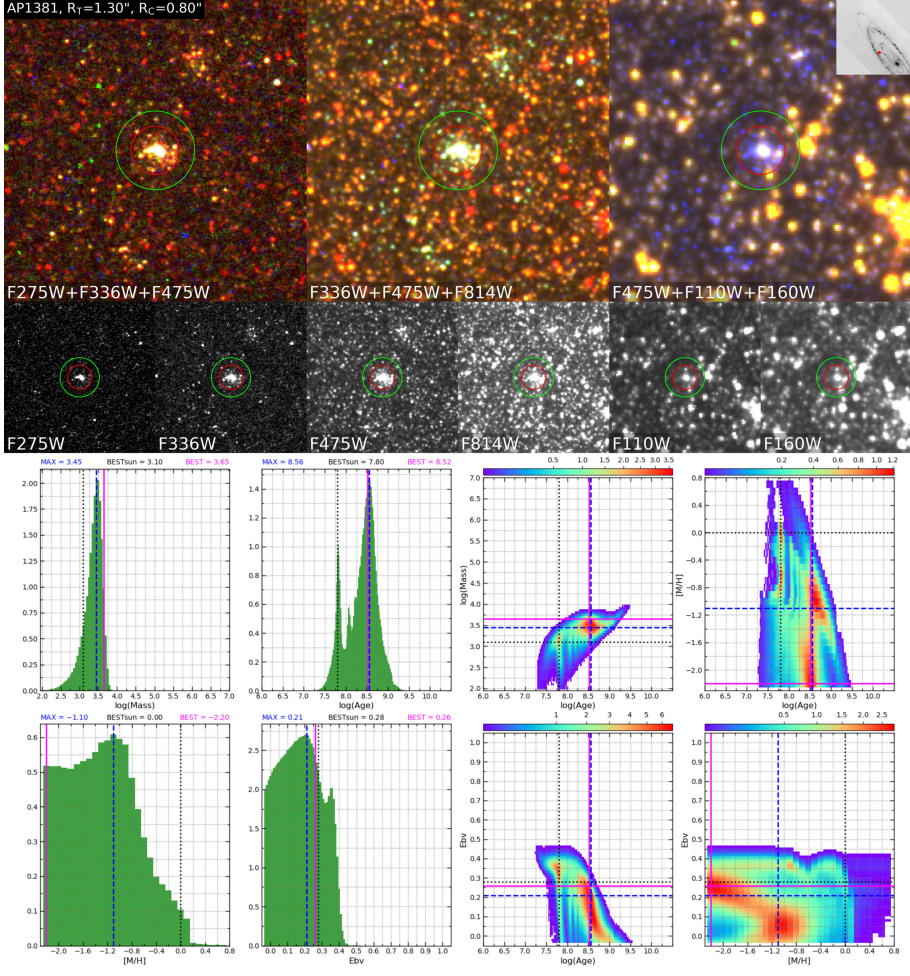


**Figure B4.** Same as in Fig. 4.1, but for cluster AP1381. Derived parameters for the cluster are: age –  $\log_{10}(t/\text{yr}) = 7.80$ , mass –  $\log_{10}(M/M_\odot) = 3.10$ , colour excess –  $E(B - V) = 0.28$ , metallicity –  $[\text{M}/\text{H}] = 0.0$ . The object exhibits two strong peaks in the age probability histogram. Due to the presence of bright field star in the  $F110W$ ,  $F160W$  passbands, we chose the C aperture parameters.

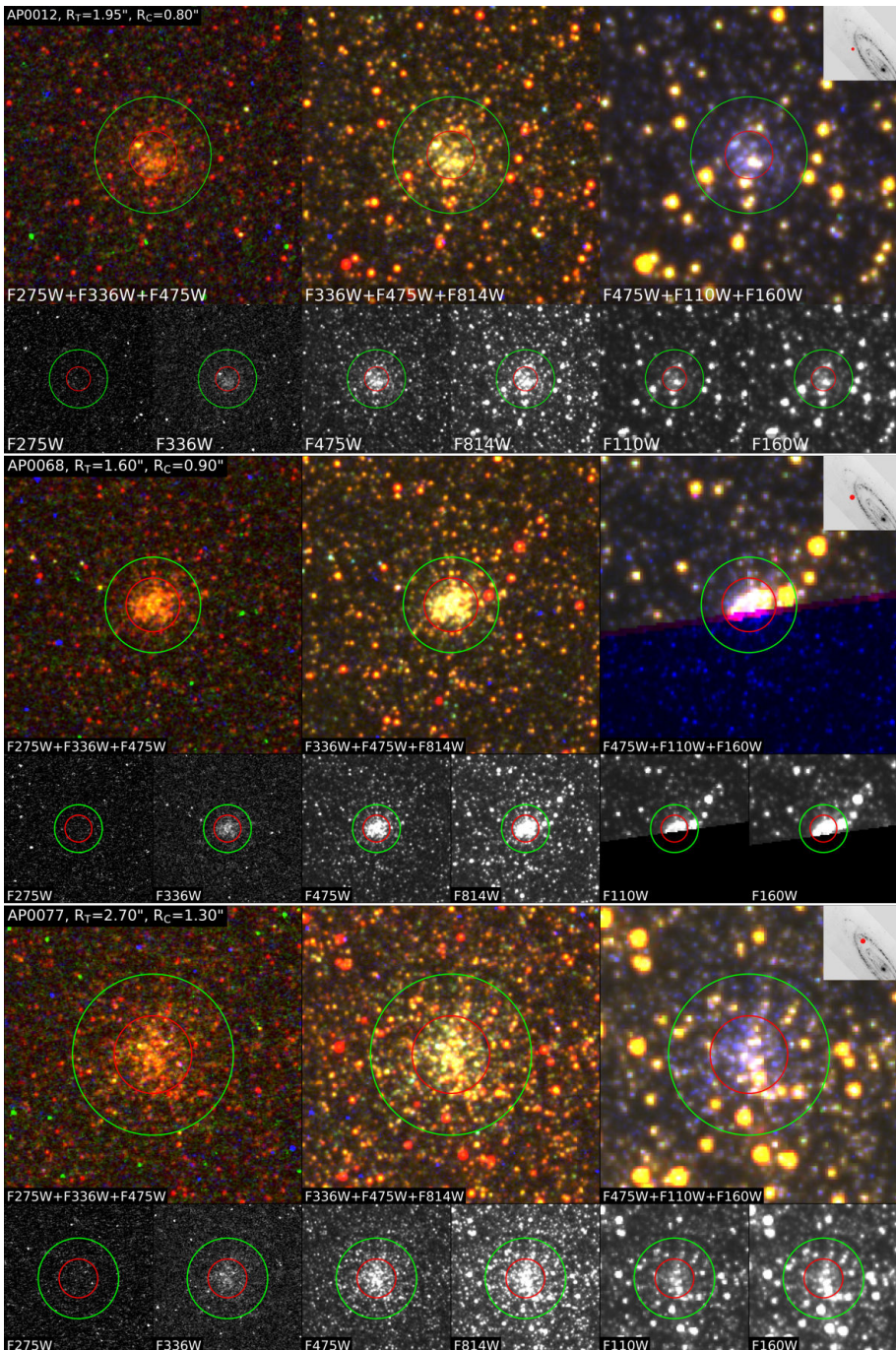


**Figure C1.** Same as in Fig. 2.2, but for clusters AP0012, AP0068, and AP0077. These objects are too old (>800 Myr) to assume solar metallicity and were excluded from our analysis.

# Conclusions

Star formation occurs in a clustered manner and raises important questions about star cluster formation history and their mass function. Unfortunately, studying such processes within the Milky Way is challenging due to observational limitations. Therefore, as the nearest stellar system similar to the Milky Way, the M 31 provides the best opportunity to explore the formation and evolution of star clusters on a broader scale.

We performed multicolour aperture photometry of 1477 star clusters in the M 31 galaxy using data from the Panchromatic Andromeda Treasury (PHAT) survey (Dalcanton et al. 2012; Johnson et al. 2012, 2015). For each object, we applied two different sets of apertures: a larger, standard (T) aperture to measure the total cluster magnitude; a smaller, adaptive (C) aperture to measure the cluster colour while minimizing contamination from bright field objects. In addition, we interactively measured the background levels for each cluster in their respective passbands to ensure accurate photometry. Excerpts from the resulting photometric catalogues are presented in Tables 3.2 (T – aperture) and 3.3 (C – aperture).

We merged the photometric measurements presented in this study with those from Naujalis et al. (2021), resulting in a combined sample of 2658 clusters with homogeneous adaptive aperture photometry. We demonstrated that our results align well with stochastic cluster models and the T photometry results differ significantly compared with the C photometry results, highlighting the importance of aperture choice in crowded field photometry.

It is worth noting that high-precision photometry in crowded disc regions is limited by uncertainty in sky background estimation and contamination from projected field stars within the photometric aperture. We demonstrate that accounting for both effects is essential for reliable flux and colour measurements. Moreover, clusters containing post main-sequence (PMS) stars show larger scatter and higher uncertainties in their photometry compared to objects without PMS stars. Our findings are in agreement with Beerman et al. (2012), showing that the absence of PMS stars results in much more consistent and well-defined cluster photometric parameters, which in turn lead to a more reliable derivation of physical parameters.

Based on photometric measurements from the catalogues of Naujalis et al. (2021); Kriščiūnas et al. (2023), we derived physical parameters – age, mass, and colour excess – for 1922 star clusters younger than 800 Myr. Excerpt from the resulting parameter catalogue is presented in Table 4.1. Most clusters are young ( $t \lesssim 300$  Myr), compact ( $R_{50} \sim 1.7$  pc), dense ( $\rho_{50} \sim 30 M_\odot \text{ pc}^{-3}$ ), and of an intermediate mass of  $M \sim 1500 M_\odot$ . The derived ages reveal that the cluster formation rate in the M 31 galaxy was rather constant during the last  $\sim 130$  Myr. However, a period of enhanced cluster-forming occurred  $\sim(200 \pm 50)$  Myr ago, which might have been triggered by

the passage of the M 32 galaxy through the M 31 disc  $\sim$ 210 Myr ago (Block et al. 2006). In addition, we detect a localized burst of cluster formation within the 16 kpc spiral arm in the last 40 Myr.

We determined a characteristic mass of the Schechter-type cluster mass function,  $M_C = (13.3^{+1.3}_{-2.6}) \cdot 10^3 M_\odot$ . This value is broadly consistent with the truncated cluster mass function found by Johnson et al. (2017). This characteristic mass value is one of the lowest observed for a star cluster population, providing clear evidence for a physical upper mass limit to cluster formation in M 31. Moreover, we have demonstrated that  $M_C$  depends on the local galactic environment, with higher  $M_C$  values concentrated in the star-forming ring and lower values found in the outskirts of the M 31 galaxy.

Our results show that both younger and older cluster populations remain spatially concentrated over extended timescales, suggesting slow dispersion from their birthplaces. This makes star clusters reliable long-term tracers of recent star formation history and the large-scale structure of star-forming regions in disc galaxies.

A global high-resolution multicolour photometric survey of the entire M 31 disc cluster population would be highly valuable for understanding the detailed evolution of galaxy discs. Supplementing such survey with spectroscopic observations and realistic stochastic models of star clusters would provide strong constraints on the evolutionary history of the Andromeda and other disc galaxies.

# Bibliography

- Adamo, A. & Bastian, N. 2015, arXiv:1511.08212
- Adamo, A., Kruijssen, J. M. D., Bastian, N., Silva-Villa, E., & Ryon, J. 2015, 452, 246
- Adamo, A., Zeidler, P., Kruijssen, J. M. D., et al. 2020, 216, 69
- Athanassoula, E. & Beaton, R. L. 2006, 370, 1499
- Barmby, P., Ashby, M. L. N., Bianchi, L., et al. 2006, 650, L45
- Barmby, P., Holland, S., & Huchra, J. P. 2002, 123, 1937
- Barmby, P. & Huchra, J. P. 2001, 122, 2458
- Barmby, P., Huchra, J. P., Brodie, J. P., et al. 2000, 119, 727
- Barmby, P., McLaughlin, D. E., Harris, W. E., Harris, G. L. H., & Forbes, D. A. 2007, 133, 2764
- Barmby, P., Perina, S., Bellazzini, M., et al. 2009, 138, 1667
- Bastian, N., Gieles, M., Ercolano, B., & Gutermuth, R. 2009, 392, 868
- Bastian, N. & Lardo, C. 2018, 56, 83
- Beasley, M. A., Brodie, J. P., Strader, J., et al. 2004, 128, 1623
- Beaton, R. L., Majewski, S. R., Guhathakurta, P., et al. 2007, 658, L91
- Beerman, L. C., Johnson, L. C., Fouesneau, M., et al. 2012, 760, 104
- Bialopetravičius, J., Narbutis, D., & Vansevičius, V. 2019, 621, A103
- Binney, J. & Tremaine, S. 2008, Galactic Dynamics: Second Edition
- Blaauw, A. 1964, 2, 213
- Block, D. L., Bournaud, F., Combes, F., et al. 2006, 443, 832
- Boutloukos, S. G. & Lamers, H. J. G. L. M. 2003, 338, 717
- Braun, R. 1991, 372, 54
- Bridžius, A., Narbutis, D., Stonkutė, R., Deveikis, V., & Vansevičius, V. 2008, 17, 337

- Brinks, E. & Burton, W. B. 1984, 141, 195
- Brodie, J. P. & Strader, J. 2006, 44, 193
- Caldwell, N., Harding, P., Morrison, H., et al. 2009, 137, 94
- Caldwell, N. & Romanowsky, A. J. 2016, 824, 42
- Caldwell, N., Schiavon, R., Morrison, H., Rose, J. A., & Harding, P. 2011, 141, 61
- Carretta, E., Bragaglia, A., Gratton, R. G., et al. 2010, 516, A55
- Chemin, L., Carignan, C., & Foster, T. 2009, 705, 1395
- Chen, Z., Williams, B., Lang, D., et al. 2025, 979, 35
- Dalcanton, J. J., Williams, B. F., Lang, D., et al. 2012, 200, 18
- Daugevičius, K., Kriščiūnas, E., Cicėnas, E., Stonkutė, R., & Vansevičius, V. 2024, 688, A131
- Daugevičius, K., Stonkutė, R., Kriščiūnas, E., Cicėnas, E., & Vansevičius, V. 2025
- de Meulenaer, P., Narbutis, D., Mineikis, T., & Vansevičius, V. 2013, 550, A20
- de Meulenaer, P., Narbutis, D., Mineikis, T., & Vansevičius, V. 2014, 569, A4
- de Meulenaer, P., Stonkutė, R., & Vansevičius, V. 2017, 602, A112
- De Somma, G., Marconi, M., Ripepi, V., et al. 2025, arXiv:2504.12638
- Deveikis, V., Narbutis, D., Stonkutė, R., Bridžius, A., & Vansevičius, V. 2008, 17, 351
- Di Matteo, P., Combes, F., Melchior, A. L., & Semelin, B. 2007, 468, 61
- Dierickx, M., Blecha, L., & Loeb, A. 2014, 788, L38
- Efremov, I. N., Ivanov, G. R., & Nikolov, N. S. 1987, 135, 119
- Fall, S. M. & Chandar, R. 2012, 752, 96
- Fitzpatrick, E. L. 1999, 111, 63
- Fouesneau, M., Johnson, L. C., Weisz, D. R., et al. 2014, 786, 117
- Fouesneau, M. & Lançon, A. 2010, 521, A22
- Freeman, P., Rosolowsky, E., Kruijssen, J. M. D., Bastian, N., & Adamo, A. 2017, 468, 1769
- Fujii, M. S. & Portegies Zwart, S. 2015, 449, 726
- Galletti, S., Federici, L., Bellazzini, M., Fusi Pecci, F., & Macrina, S. 2004, 416, 917
- Gieles, M. 2009, 394, 2113
- Gieles, M., Heggie, D. C., & Zhao, H. 2011, 413, 2509

- Gieles, M. & Portegies Zwart, S. F. 2011, 410, L6
- Gieles, M., Portegies Zwart, S. F., Baumgardt, H., et al. 2006, 371, 793
- Gordon, K. D., Bailin, J., Engelbracht, C. W., et al. 2006, 638, L87
- Gregersen, D., Seth, A. C., Williams, B. F., et al. 2015, 150, 189
- Hammer, F., Yang, Y. B., Amram, P., et al. 2025, 694, A16
- Hammer, F., Yang, Y. B., Wang, J. L., et al. 2018, 475, 2754
- Hidalgo, S. L., Pietrinferni, A., Cassisi, S., et al. 2018, 856, 125
- Hodge, P. W. 1979, 84, 744
- Hodge, P. W., Krienke, O. K., Bellazzini, M., et al. 2009, 138, 770
- Hodge, P. W., Mateo, M., Lee, M. G., & Geisler, D. 1987, 99, 173
- Hubble, E. P. 1929, 69, 103
- Jarrett, T. H., Chester, T., Cutri, R., Schneider, S. E., & Huchra, J. P. 2003, 125, 525
- Johnson, L. C., Seth, A. C., Dalcanton, J. J., et al. 2016, 827, 33
- Johnson, L. C., Seth, A. C., Dalcanton, J. J., et al. 2017, 839, 78
- Johnson, L. C., Seth, A. C., Dalcanton, J. J., et al. 2012, 752, 95
- Johnson, L. C., Seth, A. C., Dalcanton, J. J., et al. 2015, 802, 127
- Johnson, L. C., Wainer, T. M., Torresvillanueva, E. E., et al. 2022, 938, 81
- Joye, W. A. & Mandel, E. 2003, in Astronomical Society of the Pacific Conference Series, Vol. 295, Astronomical Data Analysis Software and Systems XII, ed. H. E. Payne, R. I. Jedrzejewski, & R. N. Hook, 489
- Kang, Y., Rey, S.-C., Bianchi, L., et al. 2012, 199, 37
- Kharchenko, N. V., Piskunov, A. E., Schilbach, E., Röser, S., & Scholz, R. D. 2013, 558, A53
- Kim, S. C., Lee, M. G., Geisler, D., et al. 2007, 134, 706
- Kodaira, K., Vansevičius, V., Bridzius, A., et al. 2004, 56, 1025
- Krause, M. G. H., Offner, S. S. R., Charbonnel, C., et al. 2020, 216, 64
- Krienke, O. K. & Hodge, P. W. 2007a, 119, 7
- Krienke, O. K. & Hodge, P. W. 2007b, 119, 7
- Krienke, O. K. & Hodge, P. W. 2008, 120, 1
- Kriščiūnas, E., Daugevičius, K., Stonkutė, R., & Vansevičius, V. 2023, 677, A100
- Kroupa, P. 2001, 322, 231

- Kruijssen, J. M. D. 2014, 31, 244006
- Kruijssen, J. M. D., Pfeffer, J. L., Reina-Campos, M., Crain, R. A., & Bastian, N. 2019, 486, 3180
- Krumholz, M. R., Fumagalli, M., da Silva, R. L., Rendahl, T., & Parra, J. 2015, 452, 1447
- Krumholz, M. R., McKee, C. F., & Bland-Hawthorn, J. 2019, 57, 227
- Lada, C. J. & Lada, E. A. 2003, 41, 57
- Lamers, H. J. G. L. M., Gieles, M., & Portegies Zwart, S. F. 2005, 429, 173
- Larsen, S. S. 2009, 494, 539
- Larsen, S. S. & Richtler, T. 2000, 354, 836
- Lewis, A. R., Dolphin, A. E., Dalcanton, J. J., et al. 2015, 805, 183
- Marigo, P., Girardi, L., Bressan, A., et al. 2017, 835, 77
- McConnachie, A. W., Irwin, M. J., Ferguson, A. M. N., et al. 2005, 356, 979
- Messa, M., Adamo, A., Östlin, G., et al. 2018, 473, 996
- Narbutis, D., Vansevičius, V., Kodaira, K., Bridžius, A., & Stonkutė, R. 2007, 16, 409
- Narbutis, D., Vansevičius, V., Kodaira, K., Bridžius, A., & Stonkutė, R. 2008, 177, 174
- Naujalis, R., Stonkutė, R., & Vansevičius, V. 2021, 654, A6 (Paper I)
- Peñarrubia, J., Gómez, F. A., Besla, G., Erkal, D., & Ma, Y.-Z. 2016, 456, L54
- Perina, S., Cohen, J. G., Barmby, P., et al. 2010, 511, A23
- Portegies Zwart, S. F., McMillan, S. L. W., & Gieles, M. 2010, 48, 431
- Puzia, T. H., Perrett, K. M., & Bridges, T. J. 2005, 434, 909
- Racine, R. 1980, in IAU Symposium, Vol. 85, Star Clusters, ed. J. E. Hesser, 369–380
- Reina-Campos, M. & Kruijssen, J. M. D. 2017, 469, 1282
- Renaud, F. 2018, 81, 1
- Schechter, P. 1976, 203, 297
- Smith, R., Goodwin, S., Fellhauer, M., & Assmann, P. 2013, 428, 1303
- Spitzer, Lyman, J. 1958, 127, 17
- Tody, D. 1986, in Society of Photo-Optical Instrumentation Engineers (SPIE) Conference Series, Vol. 627, Instrumentation in astronomy VI, ed. D. L. Crawford, 733
- Toomre, A. 1964, 139, 1217

- Trumpler, R. J. 1930, 420, 154
- van den Bergh, S. 1964, 9, 65
- van den Bergh, S. 1967, 72, 70
- van der Marel, R. P., Fardal, M. A., Sohn, S. T., et al. 2019, 872, 24
- Vansevičius, V., Kodaira, K., Narbutis, D., et al. 2009, 703, 1872
- Vazdekis, A., Sánchez-Blázquez, P., Falcón-Barroso, J., et al. 2010, 404, 1639
- Čeponis, M., Stonkutė, R., & Vansevičius, V. 2024, 64
- Vetešnik, M. 1962, 13, 180
- Wainer, T. M., Johnson, L. C., Seth, A. C., et al. 2022, 928, 15
- Wang, Y., Gao, J., Ren, Y., & Chen, B. 2025, 169, 250
- Weisz, D. R., Johnson, L. C., Foreman-Mackey, D., et al. 2015, 806, 198
- Whitmore, B. C., Chandar, R., Schweizer, F., et al. 2010, 140, 75
- Williams, B. F. 2003, 340, 143
- Williams, B. F., Dalcanton, J. J., Dolphin, A. E., et al. 2015, 806, 48
- Williams, B. F., Dolphin, A. E., Dalcanton, J. J., et al. 2017, 846, 145
- Williams, B. F., Durbin, M. J., Dalcanton, J. J., et al. 2021, 253, 53
- Williams, B. F. & Hodge, P. W. 2001a, 559, 851
- Williams, B. F. & Hodge, P. W. 2001b, 548, 190
- Worthey, G. 1994, 95, 107
- Yin, J., Hou, J. L., Prantzos, N., et al. 2009, 505, 497
- Zhang, Q. & Fall, S. M. 1999, 527, L81

# Santrauka

## Ivadas

Galaktikų formavimasis ir evoliucija yra viena pagrindinių šiuolaikinės astrofizikos problemų. Kadangi didžioji dalis galaktikose esančių žvaigždžių formuojasi žvaigždžių spieciuose, būtent šie objektai yra plačiai taikomi norint išspręsti minėtas problemas. Žvaigždžių spiečius – gravitaciškai susietų žvaigždžių grupė, kurioje nedominuoja tamsioji materija. Detalūs spiečių stebėjimai Paukščių Take (toliau – Galaktika) yra apriboti, nes spiečių aptikimą Galaktikos plokštumoje komplikuoja didelė tarpžvaigždinė ekstinkcija ir ribinis stebėjimų tūris. Patikimi duomenys apie spiečius Galaktikoje gaunami tik iki  $\sim 2$  kpc spindulio (Kharchenko et al. 2013) ap link Saulė. Todėl siekiant detalesnės ir globalios žvaigždėdaros procesų dėsningumų sampratos, žvaigždžių spiečiai yra stebimi morfologiškai panašiose sistemose į mūsų Galaktiką. Šiam tikslui puikiai tinkta artimiausia ir didžiausia diskinė galaktika – Andromeda (M 31). Dėl nedidelio atstumo iki M 31 mes galime išskirti atskiras šios galaktikos struktūras kaip spiralines vijas ir žvaigždėdaros regionus, kurių stebėjimai leidžia nustatyti žvaigždėdaros procesus priežastis, pasekmes, bei jų poveikį galaktikos žvaigždžių populiaciją raidai. Žvaigždžių spiečiai yra patikimi objektai M 31 struktūrų nagrinėjimui, kadangi jie turi vienodo amžiaus ir metalingumo žvaigždžių populiaciją. Taip pat, spiečių savybes mes galime modeliuoti įvairiuose evoliucijos etapuose, kuriuos mes galime palyginti su realiais stebėjimų duomenimis.

Patikimi žvaigždžių spiečių stebėjimai M 31 atliekami *Hubble* kosminiu teleskopu (HST). Tačiau dauguma tyrimų koncentruojasi į kamuolinius spiečius, esančius M 31 hale (Barmby et al. 2002, 2007; Caldwell et al. 2009). Išsamūs disko žvaigždžių spiečių tyrimai prasidėjo su PHAT (angl. Panchromatic *Hubble* Andromeda Treasury, Dalcanton et al. 2012) apžvalga, kuri aprėpė šiaurės rytų regioną, einant nuo M 31 centro iki galaktikos pakraščių. HST PHAT apžvalga įgalino identifikuoti žvaigždžių spiečius, kurie prieš tai nebuvo matomi antžeminiais teleskopais. Taip pat PHAT stebėjimų duomenys suteikia aukštostos kokybės informaciją kuri yra reikalinga spiečių parametru (amžius, masė, metalingumas, ekstinkcija) nustatymui. Vis dėlto, susiduriame ir su neapibrėžtumais kurie komplikuoja parametrų nustatymą. Pagrindinis duomenų neapibrėžtumo šaltinis yra amžiaus ir ekstinkcijos išsigimimas, kai jaunas spiečius su ekstinkcija gali turėti tokią pačią spalvą kaip ir senas spiečius be ekstinkcijos (de Meulenaer et al. 2013, 2014).

Norėdami kuo tiksliau nustatyti fizinius spiečių parametrus, kurių tikslumas tiesiogiai priklauso nuo stebėjimų kokybės, pirma atlikome stebėjimo duomenų korekcijas. Johnson et al. (2012, 2015) PHAT apžvalgos žvaigždžių spiečiams pritaikė integralinę apertūrinę fotometriją, tačiau besiprojektuojančios lauko žvaigždės į spiečiaus apertūrą

gali iškraipyti tikrąsias spiečiaus spalvas, kas reikšmingai paveikia nustatytus fizinius parametrus, kurie yra itin jautrūs spalvų pokyčiams. Beerman et al. (2012) padėdė, kad spiečių parametrai gali būti nustatomi tiksliau, jeigu iš analizės pašalinamos ryškios, raudonos RGB žvaigždės. Todėl, siekdami tiksliau įvertinti spiečių spalvas, pritaikėme adaptyvios apertūrinės fotometrijos metodą (Naujalis et al. 2021). Šis metodas remiasi dviem apertūromis: viena skirta matuoti visą spiečiaus srautą, o kita mažesnė apertūra, kuri apima tik centrinę spiečiaus dalį yra skirta pašalinti ryškias lauko žvaigždes. Šis dvių apertūrų metodas padeda sumažinti užterštumą ir leidžia tiksliau išmatuoti spiečiaus spalvas. Tuomet, remdamiesi PHAT stebėjimų fotometrijos katalogais (Naujalis et al. 2021; Kriščiūnas et al. 2023), nustatėme spiečių fizinius parametrus – amžių, masę ir ekstinkciją – naudodami stochastinių modelių tinklelių, bei atlikome žvaigždžių spiečių evoliucijos analizę M 31 diske.

## Darbo tikslas

Ištirti jaunų žvaigždžių spiečių populiaciją Andromedos galaktikoje (M 31).

## Uždaviniai

- Atlikti M 31 galaktikos žvaigždžių spiečių daugiaspalvę apertūrinę fotometriją.
- Nustatyti M 31 galaktikos žvaigždžių spiečių parametrus: amžius, masė ir tarpžvaigždinė ekstinkcija.
- Ištirti M 31 galaktikos diskų žvaigždžių spiečių populiacijos savybes.

## Rezultatai ir ginamieji teiginiai

1. Atlikta 1477 M 31 žvaigždžių spiečių apertūrinė šešių spalvų fotometrija.
2. Nustatyti 1922 M 31 žvaigždžių spiečių parametrai: amžius, masė ir tarpžvaigždinė ekstinkcija.
3. M 31 galaktikos šių dienų diskų šiaurės-rytų dalyje paskutinis žvaigždžių spiečių formavimasis suaktyvėjimas įvyko prieš  $\sim(200 \pm 50)$  mln. m.
4. M 31 galaktikos išoriniame 16 kpc žvaigždėdaros žiede aktyvus spiečių formavimasis vyko tik pastaruosius  $\sim 40$  mln. m.
5. M 31 galaktikos žvaigždžių spiečių masės skirstinys gerai aprašomas Schechter'o tipo funkcija, kurios charakteringa masė,  $M_C = (13,3_{-2,6}^{+1,3}) \cdot 10^3 M_\odot$ .

## Autoriaus indėlis

Autorius nustatė spiečių centrų koordinates, pašalino nuotraukų defektus, parinko apertūrų dydžius ir interaktyviai nustatė fono lygius. Kartu su bendraautoriais nustatė žvaigždžių spiečių fizinius parametrus (amžius, masė ir ekstinkcija), išanalizavo spiečių populiacijos savybes ir parengė apertūrinės fotometrijos bei spiečių parametrų katalogus.

# Skyrius 1

## Andromedos (M 31) galaktika

**1.1 lentelė.** M 31 galaktikos parametrai.

Parametras	Vertė	Šaltinis
<i>Hubble</i> tipas	SA(s)b	Jarrett et al. (2003)
$\alpha$ (J2000); $\delta$ (J2000)	$00^{\text{h}} 42^{\text{m}} 44,3^{\text{s}}$ ; $+41^{\circ} 16' 9''$	McConnachie et al. (2005)
P.A.	$37,7^{\circ}$	Chemin et al. (2009)
Incl.	$77,5^{\circ}$	van der Marel et al. (2019)
Atstumas	$785 \pm 25$ kpc	McConnachie et al. (2005)
$(m - M)_0$	24,47 mag	McConnachie et al. (2005)
$E(B - V)$	0,06 mag	McConnachie et al. (2005)
$V_{\text{rot}}$	$\sim 250$ km/s	Chemin et al. (2009)
Dinaminė masė	$4,5 \cdot 10^{11} M_{\odot}$	Hammer et al. (2025)

$\alpha$ (J2000) ir  $\delta$ (J2000) – galaktikos centro pusiaujinės koordinatės (atitinkamai rektascencija ir deklinacija); P.A. – didžiosios ašies pozicinės kampas; Incl. – polinkio kampas;  $(m - M)_0$  – atstumo modulis;  $E(B - V)$  – tarpžvaigždinė ekstinkcija stebėjimo kryptimi;  $V_{\text{rot}}$  – sukimosi greitis ties 10 kpc atstumu nuo M 31 centro.

Andromeda (M 31) yra artimiausia diskinė galaktika Vietinėje galaktikų grupėje, nutolusi  $\sim 785$  kpc atstumu (McConnachie et al. 2005) nuo Paukščių Tako ( $1'' = 3,8$  pc; Vansevičius et al. 2009). Šiek tiek masyvesnė nei mūsų Galaktika (Peñarrubia et al. 2016; Hammer et al. 2025), M 31 pasižymi skirtinė evoliucijos raida, kurią formavo daugybė didelių susijungimų su mažesnėmis galaktikomis per pastaruosius 4 mlrd. m. (Williams et al. 2015; Hammer et al. 2018). Šios galaktikų tarpusavio sąveikos greičiausiai turėjo didelės įtakos formuojant Andromedos struktūrą, žvaigždėdaros žiedus ir nuo jų priklausė žvaigždėdaros aktyvumas. Detalius M 31 struktūrinius tyrinėjimus apsunkina didelis polinkio kampus ( $\sim 77,5^{\circ}$ , van der Marel et al. 2019), taip pat nėra aiškaus susitarimo dėl spiralinių vių išsidėstymo. Viena iš pagrindinių M 31 galaktikos struktūrų yra gerai žinomas 10 kpc žvaigždėdaros žiedas (Gordon et al. 2006; Kang et al. 2012; Lewis et al. 2015; De Somma et al. 2025), kuris yra iškreiptas dėl sąveikos su kaimynine galaktika prieš kelias dešimtis ar šimtus milijonus metų (Gordon et al. 2006; Block et al. 2006; Dierickx et al. 2014). Disertacijoje naudojami M 31 parametrai yra pateikti 1.1 lentelėje.

Andromedos galaktikos žvaigždžių spiečių tyrimai yra vykdomi jau nuo praeito

amžiaus septintojo dešimtmečio kur van den Bergh (1964) stebėjo 188 žvaigždžių asociacijas. Vėliau Hodge (1979) atliko M 31 disko apžvalgą pasitelkiant "Kitt Peak National Observatory" 4-m teleskopą. Šio tyrimo metu buvo sudarytas 403 disko žvaigždžių spiečių katalogas, kuriame daugiausia buvo jauni ir ryškiausi objektais. Tačiau HST vaizdų analizė atskleidė, kad ši imtis buvo užteršta, nes iš jų pateko OB asociacijos ir asterizmai (Williams & Hodge 2001b). Asterizmas – žvaigždžių grupė, kuri dangaus skliaute atrodo sutankėjusi, tačiau, priešingai nei tikri žvaigždžių spiečiai, nebūtinai yra gravitaciškai susieta. Toliau, šio amžiaus pradžioje Williams & Hodge (2001b) pasitelkė HST WFPC2 vaizdus, kad sudarytų keturių jaunuų spiečių spalvos-ryškio diagramas (CMD). Šių spiečių analizė parodė, kad objektų amžius kinta 60-150 mln. m. intervale, todėl jie ženkliai skiriasi nuo tradicinių Galaktikos kamuolinių spiečių, kurie yra gerokai senesni (Krienke & Hodge 2007a). Šis rezultatas taip pat prieštarauja ankstesniems tyrimams (Vetešnik 1962; van den Bergh 1967), kuriuose šie spiečiai buvo klasifikuoti kaip kamuoliniai, remiantis jų spalvų matavimais.

Per pastaruosius du dešimtmečius buvo publikuoti įvairūs M 31 žvaigždžių spiečių katalogai (Barmby et al. 2000; Galletti et al. 2004; Kim et al. 2007; Caldwell et al. 2009, 2011). Barmby et al. (2000) pristatė 435 spiečių ir kandidatų UBVRI bei JHK fotometrija. Tačiau tik 268 objektams yra prieinama optinė fotometrija keturiose ar daugiau juostų, o 224 turi tik infraraudoną (IR) fotometriją. Galletti et al. (2004) pasinaudojo "2 Micron All Sky Survey" duomenų baze ir identifikavo 693 žinomus bei kandidatus į kamuolinius spiečius M 31 galaktikoje, pristatydami "Atnaujintą Bolonijos katalogą". Kim et al. (2007) atliko plataus lauko stebėjimus ir atrado 113 nauju žvaigždžių spiečių bei 258 galimus objektus, kurie galėtų būti klasifikuojami kaip spiečiai. Caldwell et al. (2009) paskelbė naują 670 tiketinų žvaigždžių spiečių katalogą, pateikdami tikslias koordinates iš "Local Group Galaxy Survey" ir "Digitized Sky Survey" duomenų. Nepaisant šių pastangų, sukurti išsamų ir homogenišką M 31 disko žvaigždžių spiečių katalogą pasirodė esą sudėtinga. Dauguma darbų orientavosi į kamuolinius žvaigždžių spiečius, kurii žvaigždės yra koncentruotos į centrą. Šie objektai yra masyvūs, ryškūs ir sferiniai, todėl juos lengviau stebėti M 31 halo srityje. Tuo tarpu aptiki santykinai blankius spiečius, kurie projektuoja M 31 diske buvo sudėtinga.

Išsamesni disko žvaigždžių spiečių tyrimai prasidėjo atsiradus HST (Williams & Hodge 2001b,a). Tačiau spiečių imtys buvo per mažos (Barmby et al. 2009; Perina et al. 2010) arba nehomogeniškos (Krienke & Hodge 2007a, 2008; Hodge et al. 2009), kad būtų galima daryti išvadas apie M 31 disko evoliuciją ar formavimąsi. Pirmasis homogeniškas žvaigždžių spiečių tyrimas buvo atliktas pietvakarinėje M 31 dalyje (Kodaira et al. 2004; Narbutis et al. 2008; Vansevičius et al. 2009). Naudojant Subaru teleskopą, M 31 diske buvo identifikuoti 238 žvaigždžių spiečiai. Po kelių metų sekė PHAT tyrimas šiaurės rytų dalyje (Dalcanton et al. 2012), kuris papildė disko žvaigždžių spiečių imtį maždaug 10 kartų. Visai neseniai buvo atliktas PHAST (angl. Panchromatic Hubble Andromeda Southern Treasury) tyrimas (Chen et al. 2025), kuris yra gretimas PHAT apžvalgai ir apimantis pietinę M 31 pusę, taip dar labiau išplečiantis žvaigždžių spiečių tyrimus. Tad galima teigti, kad vienas didžiausiu iššūkiu nagrinėjant spiečių formavimąsi ir evoliuciją slypi stebėjimų ir matavimų sudėtingume, bei ribotuose imčių dydžiuose, kurios dažnai įtraukia tik didelės masės spiečius (Krumholz et al. 2019).

# Skyrius 2

## Stebėjimų duomenys

### 2.1 PHAT apžvalga

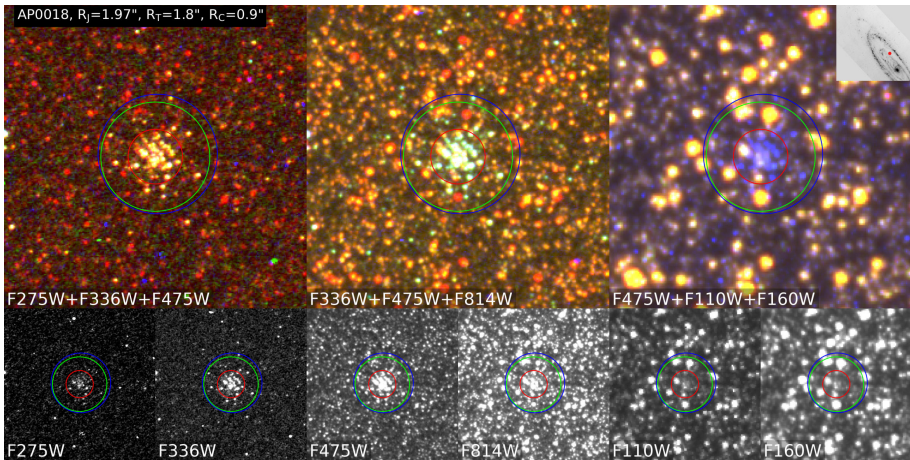
Andromedos galaktikos žvaigždžių spiečių tyrimams naudojome HST PHAT apžvalgos duomenis (Dalcanton et al. 2012), kurie yra paimti iš "Hubble Legacy Archive" (HLA)<sup>1</sup>. PHAT stebėjimai yra padalinti į 23 stačiakampius blokus, kurie yra sunumeruoti didėjimo tvarka einant nuo galaktikos centro. Kiekvienas blokas yra sudarytas iš 18 HST stebėjimo laukelių, kurie yra išdėstyti  $6 \times 3$  tinkleliu. Vienas blokas danguje padengia  $12' \times 6,5'$  dydžio lauką. Žvaigždžių spiečių stebėjimai yra atliliki šešiose fotometrinės juostose naudojant tris HST kameras. Nuotraukos optinėje srityje gautos ACS/WFC kamera naudojant  $F475W$  ir  $F814W$  filtrus, artimoje ultravioletinėje srityje gautos WFC3/UVIS kamera naudojant  $F275W$ ,  $F336W$  filtrus, artimoje infraraudonoje srityje gautos WFC3/IR kamera naudojant  $F110W$ ,  $F160W$  filtrus. Taip pat PHAT apžvalgoje skirtingų fotometriniai juostų (FJ) nuotraukos turi skirtinę pasikartojančią ekspozicijų skaičių:  $F475W$  turi penkias ekspozicijas,  $F814W$  ir  $F160W$  – keturias,  $F275W$  ir  $F336W$  – dvi,  $F110W$  – vieną.

### 2.2 Spiečių imtis

PHAT apžvalgai yra publikuotas 2753 spiečių katalogas (Johnson et al. 2015) su integruota fotometrija. Pirmoji katalogo dalis ( $N = 1181$ ) buvo ištirta Naujalis et al. (2021) pasitelkiant adaptyvią apertūrinę fotometriją. Mūsų tikslas yra išnagrinėti likusių katalogų dalį ( $N = 1572$ ) pritaikant tą pačią metodiką. Atlikus vizualinę vaizdų analizę (2.1 pav.) iš savo nagrinėjamos imties pašalinome 90 objektų, kurie turėjo signalą tik  $F475W$  ir  $F814W$  filtruose. AP1848 ir AP2446 objektus išmetėme dėl fone besiprojektuojančios galaktikos. AP1588, AP1661 ir AP2687 objektais savo nuotraukose turi ryškių žvaigždžių atspindį arba emisijos linijas, dėl to mes jų taip pat atsisakėme. AP3630, AP4034, AP4132 objektais turi nepataisomus tuščių pikselių defektus  $F475W$  FJ. Trys spiečiai – AP0239, AP1782, AP3306 – savo apertūroje turėjo dvi skirtinas populiacijas, dėl to mes juos atskyrėme ir antrus komponentus pažymėjome: AP60239, AP61782, AP63306. Kiekvienam spiečiui individualiai taip pat peržiūrėjome nuotraukas ir parinkome geriausius  $F275W$ ,  $F336W$ ,  $F110W$ ,

---

<sup>1</sup><https://hla.stsci.edu>



**2.1 pav.** Spiečiaus AP0018 nuotrauka su įvairiomis filtrų kombinacijomis (viršuje) ir visose šešiose fotometrinėse juostose (apačioje). Fotometrinių juostų pavadinimai ir kombinacijos pateiktos nuotraukų apatinėje dalyje. Mėlynas, žalias ir raudonas apskritimai žymi Johnson et al. (2015), T ir C apertūras atitinkamai. Kiekvienos nuotraukos dydis  $10'' \times 10''$ . Intarpas nuotraukos viršuje rodo spiečiaus poziciją M 31 galaktikoje.

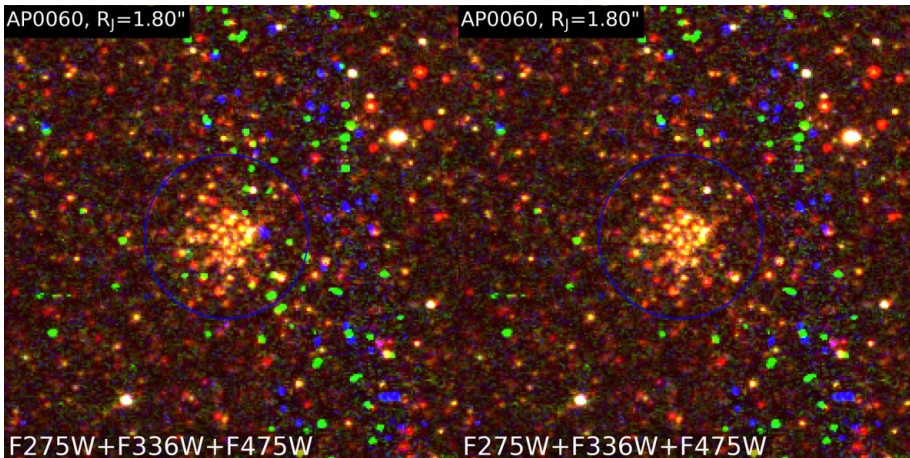
*F160W* FJ laukelius, parinkdami variantus kurie turi didžiausią signalo-triukšmosantykį (S/N), bei kurie pasižymi mažiausiu kosminių spindulių kiekiu. 11 objektų *F110W*, *F160W* laukelius pakeitėme, nes jie neturėjo jokio signalo; 64 objektams pakeitėme *F275W*, *F336W* laukelius, kadangi nauji variantai turėjo geresnį S/N santykį ir mažiau kosminių spindulių defektų.

## 2.2.1 Defektų valymas

Dėl mažo ekspozicijų skaičiaus *F275W* ir *F336W* FJ yra išlikę kosminių spindulių defektai. Kosminiai spinduliai yra aukštos energijos dalelės, kurios smūgio metu perduoda energiją detektoriaus pikseliams, sukurdamos signalus, imituojančius išorinius šviesos šaltinius. Todėl kosminių spindulių defektai gali atrodyti panašūs į žvaigždiņius objektus. Kiekvienas defektas esantis Johnson et al. (2015) apibrėžtoje spiečiaus apertūroje buvo išvalytas naudojant *imedit* funkciją *IRAF*<sup>2</sup> pakete (Tody 1986). Ši funkcija leidžia pažymeti nuotraukos sričią, kurioje yra defektas ir interpoliuoti ją į statistiškai aplinkinį foną. 2.2 pav. yra spiečiaus pavyzdys spalvotoje nuotraukoje (*F275W+F336W+F475W*), kur yra pavaizduotas objektas prieš kosminių spindulių išvalymą ir po. Abejose nuotraukose kosminiai spinduliai matomi kaip žalios ir/arba mėlynos dėmės, neturinčios atitinkmenų kituose filtruose. Šių dėmių dydis gali skirtis nuo kelių pikselių iki kelių dešimčių, dėl to jas yra sunku išvalyti naudojant automatinius metodus. Kartais defektai gali persikloti su žvaigždėmis. Tokie atvejai yra aptinkami pasitelkiant augimo kreives ir atitinkamos fotometrinės juostos yra atmetamos. Nors akivaizdūs defektai buvo pašalinti vizualinės patikros metu, kai kuriais atvejais nepastebėti kosminiai spinduliai galėjo likti.

Kai kuriose nuotraukose taip pat pasitaikė tuščių pikselių. Tai ypač būdinga *F110W*

<sup>2</sup><https://iraf-community.github.io>



**2.2 pav.** Spiečiaus AP0060 nuotrauka  $F275W+F336W+F475W$  fotometrinijų juostų kombinacijoje. Kairėje parodytos nevalytos  $F275W$  ir  $F336W$  nuotraukos su kosminiu spinduliu defektais (žali ir mėlyni objektais), dešinėje tas pats objektas po išvalymo.

filtrui, kuris neturi pasikartojančių ekspozicijų. Tokiu atveju mes priskyrėme aštuonių supančių aktyvių pikselių verčių vidurkį. Tačiau tais atvejais, kai po šios procedūros apertūroje liko bent vienas nekoreguotas pikselis, matavimų šioje FJ atsisakėme.

## 2.2.2 Centro koordinačių nustatymas

Pastebėjus, kad spiečius yra blogai sucentruotas, naujas centrų koordinates parinkome atsižvelgdami į  $F336W$ ,  $F475W$  ir  $F814W$  FJ. Šie filtrai buvo pasirinkti, nes jie yra mažiau paveikti lauko žvaigždžių, todėl galime aiškiau identifikuoti spiečių centrus. Centro koordinates pakoregavome 1331 spiečiams naudodami DS9 programinę įrangą (Joye & Mandel 2003). Daugeliu atveju koordinatės buvo pakeistos tik keliais pikseliais, išskyrus žvaigždžių asociacijas, kuriose daugiausia pasirinkome į spiečius panašias sritis.

# Skyrius 3

## Apertūrinė fotometrija

Šiame darbe pritaikėme adaptyvios apertūrinės fotometrijos metodą, kuris buvo pristatytas Naujalis et al. (2021). Naudodami atnaujintas koordinates, kiekvienam spiečiui nubraižėme augimo kreives visose šešiose fotometrinėse juostose, pritaikant  $0'',01$  žingsnį. Spiečiams su mažoms apertūromis buvo taikomas minimalus  $5''$  matavimo spindulys, kad būtų užtikrintas pakankamas dangaus fono padengimas.

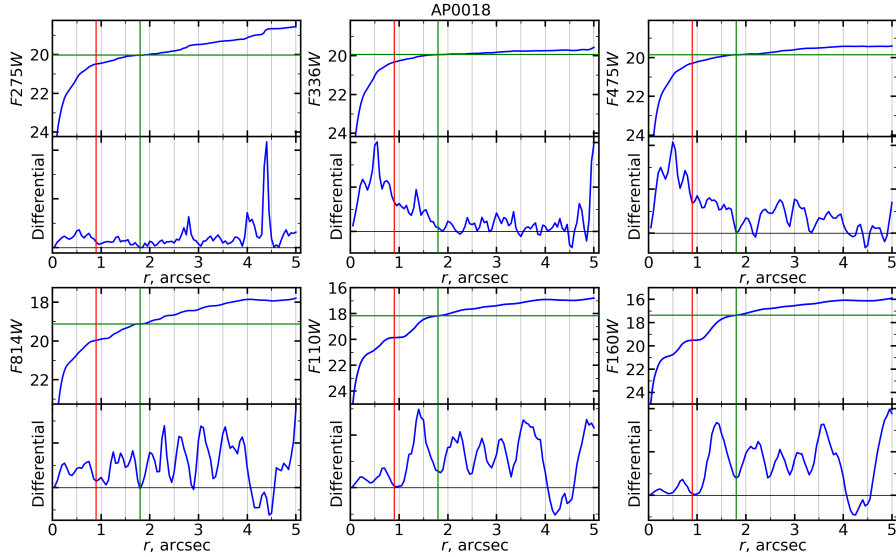
Toliau kiekvienam analizuojamam spiečiui buvo parengtas nuotraukų rinkinys (2.1 pav.) su augimo ir diferencialinėmis kreivėmis (3.1 pav.), bei parinktos dvi naujos apertūros. 2.1 pav. žalias apskritimas žymi pilnutinę, T apertūrą, kuri yra skirta matuoti pilnutinį ryškį  $F475W$  fotometrinėje juosteje ir apimanti kuo daugiau spiečiaus šviesos; raudonas apskritimas žymi spalvinę, C apertūrą, kuri skirta matuoti spiečiaus spalvą ir parinkta taip, kad į ją pakliūtų kuo mažiau lauko žvaigždžių, kurios gali iškraipyti objekto spalvą.

3.1 pav. pavaizduotos spiečiaus AP0018 augimo kreivės (viršuje) ir diferencialiniai profiliai (apačioje) kiekvienoje FJ. Vertikalios raudonos ir žalios linijos žymi atitinkamai  $R_C$  ir  $R_T$  apertūrų spindulius. Žalios horizontalios linijos rodo iš T srautų gautus ryškius. Neigiamos vertės diferencialiniame profilyje rodo, kad išmatuotas signalas šioje srityje yra mažesnis už atimtą vidutinį fono lygi. Tuo tarpu žvairūs pikai rodo išskirtas ryškias žvaigždžes ir pabrėžia aplinkinio dangaus fono sudėtingumą.

Žvaigždžių spiečių ir jų aplinkinio dangaus fonų žvairovė apsunkina atskirų spiečiaus žvaigždžių atskyrimą nuo lauko objektų. Tačiau daugeliu atvejų, naudojant daugiaspalvius spiečių vaizdus (2.1 pav.) kartu su spiečių profiliais (3.1 pav.), pavyko nustatyti optimalius  $R_C$  ir  $R_T$  apertūrų spindulius.

### 3.1 Fono lygio nustatymas

Spiečių supantį foną sudaro spiečiui nepriklausančios M 31 galaktikos disko žvaigždės, fonišės galaktikos ir besiprojektuojančios Galaktikos žvaigždės. Taip pat didžioji dalis M 31 žvaigždžių yra pilnai arba tik dalinai išskirtos, tad fonas M 31 diske yra netolygus. Fono lygio nustatymo sudėtingumas lemia, kad tai yra vienas iš didžiausių neapibrėžtumų šaltinių apertūrinėje fotometrijoje. Norint išspręsti fono lygio nustatymo problemą, yra pasiūlyta nemažai automatinių algoritmų (Barmby & Huchra 2001; Krienke & Hodge 2007b; Johnson et al. 2012), tačiau jų patikimumas yra ypač žemas itin tankiose srityse kaip M 31 diske. Kadangi automatiniai metodai



**3.1 pav.** Spiečiaus AP0018 augimo kreivės (viršuje) ir diferencialiniai profiliai (apačioje). Vertikali raudona ir žalia linijos rodo  $R_C$  ir  $R_T$  apertūrų spindulius. Horizontali žalia linija rodo ties T apertūra gautą ryškį.

skirtingose FJ duoda nenuoseklus fono lygio rezultatus, dėl to kiekvienam spiečiui nubraižėme augimo/diferencialinio srauto profilius (3.1 pav.) ir interaktyviai parinkome atitinkamus fono lygius. Diferencialiniai profiliai (apatiniai skydeliai 3.1 pav.) rodo atskirų žvaigždžių arba defektų sukeltas fliktuacijas ir buvo itin svarbūs priimant sprendimą dėl apertūrų parinkimo. Ypatingą dėmesį skyrėme ryškių lauko žvaigždžių tiksliai korekcijai  $F110W$ ,  $F160W$  FJ. Taip pat kosminių spinduliu defektams, kurie ypač ryškūs ultravioletinėse (UV) fotometrinėse juostose. Fono lygius pakoregovome interaktyviai kiekvienai FJ, siekiant padaryti plokščias augimo kreives ir diferencialinius profilius priartinti prie nulio dangaus fono nustatymo srityje.

Naudodami spiečių nuotraukų analizę, augimo kreives ir diferencialinius profilius, mes nustatėme tikslius fono lygius visose šešiose fotometrinėse juostose. Deja, interaktyvus fono nustatymo metodas turi du pagrindinius trūkumus – tai labai daug laiko reikalaujantis procesas, kuris gali įvesti ir sistemines paklaidas, jeigu fonas turi labai sudėtingą struktūrą.

## 3.2 Apertūrų parinkimas

Norėdami sumažinti besiprojektuojančių lauko žvaigždžių poveikį spiečių apertūrose, mes parinkome dvi koncentrinės apertūras: T ir C. Pagrindinis T apertūros parinkimo kriterijus, kad ji nekirstų ryškių lauko objektų, kurie galėtų stipriai paveikti spiečiaus matavimus; C apertūros parinkimo kriterijus buvo išvengti ryškiausių lauko žvaigždžių jų viduje (2.1 pav.). Mūsų parinkti T apertūrų spinduliai kinta nuo  $\sim 1''$ , mažiemis ir kompaktiškiems spiečiams, iki  $\sim 4''$  kamuoliniam spiečiamams ir žvaigždžių asociacijoms.

### 3.1 lentelė. M 31 galaktikos žvaigždžių spiečių T apertūros fotometrijos rezultatai.

AP	RA(2000) <sup>(a)</sup>	DEC(2000) <sup>(a)</sup>	R <sub>T</sub> <sup>(b)</sup>	F275W <sub>T</sub>	F336W <sub>T</sub>	F475W <sub>T</sub>	F814W <sub>T</sub>	F110W <sub>T</sub>	F160W <sub>T</sub>
12	11,45697	41,65734	1,95	21,201 0,082	20,491 0,017	19,887 0,005	18,384 0,004	17,784 0,005	17,124 0,007 <sup>(c)</sup>
17	11,49040	42,02750	1,80	20,857 0,057	20,724 0,019	20,377 0,005	19,523 0,006	19,326 0,013	19,066 0,020
18	10,87149	41,57674	1,80	20,035 0,030	19,946 0,010	19,860 0,006	19,128 0,013	18,171 0,020	17,364 0,019

**Pastabos.** Lentelėje pateikta tik dalis pirmų trijų spiečių duomenų. <sup>(a)</sup>RA(2000) ir DEC(2000) pusiaujinės koordinatės laipsniais. <sup>(b)</sup>T apertūros spindulys kampinėms lanko sekundėms. <sup>(c)</sup>T apertūros paklaidos ( $\sigma_T$ ) kiekvienoje fotometrinėje juosteje.

### 3.2 lentelė. M 31 galaktikos žvaigždžių spiečių C apertūros fotometrijos rezultatai.

AP	RA(2000) <sup>(a)</sup>	DEC(2000) <sup>(a)</sup>	R <sub>C</sub> <sup>(b)</sup>	F275W <sub>C</sub>	F336W <sub>C</sub>	F475W <sub>C</sub>	F814W <sub>C</sub>	F110W <sub>C</sub>	F160W <sub>C</sub>
12	11,45697	41,65734	0,80	21,533 0,103	20,539 0,017	19,887 0,005	18,547 0,007	18,083 0,009	17,543 0,010 <sup>(c)</sup>
17	11,49040	42,02750	0,95	20,898 0,055	20,660 0,017	20,377 0,005	19,715 0,009	19,595 0,014	19,406 0,023
18	10,87149	41,57674	0,90	20,055 0,024	19,896 0,010	19,86 0,006	19,534 0,013	19,423 0,031	19,081 0,045

**Pastabos.** Lentelėje pateikta tik dalis pirmų trijų spiečių duomenų. <sup>(a)</sup>RA(2000) ir DEC(2000) pusiaujinės koordinatės laipsniais. <sup>(b)</sup>C apertūros spindulys kampinėms lanko sekundėms. <sup>(c)</sup>C apertūros paklaidos ( $\sigma_C$ ) kiekvienoje fotometrinėje juosteje.

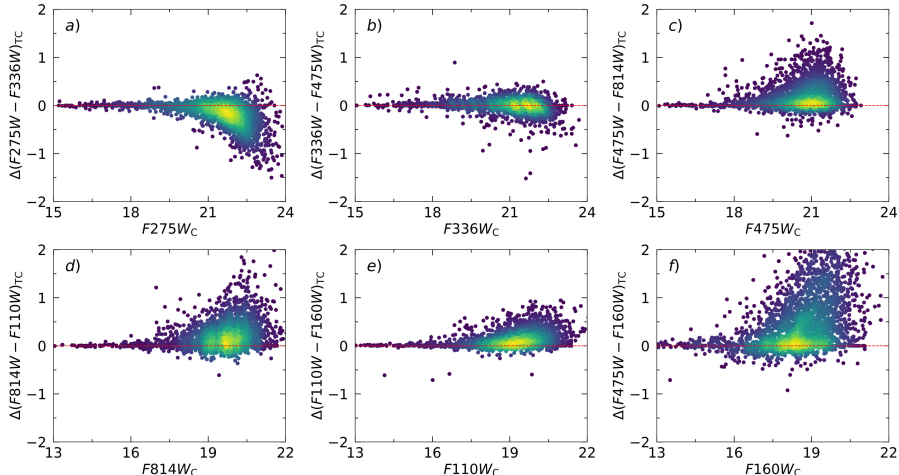
Žvaigždžių spiečių ryškiai, naudojant C apertūrą, buvo skaičiuoti pagal formulę:  $F?W = F?W_C - F475W_{AC}$ , kur "?" žymi HST fotometrinės juostos pavadinimą,  $F?W_C$  – ryškiai išmatuoti naudojant C apertūrą,  $F475W_{AC}$  – apertūrinė korekcija. Kadangi naudojama C apertūra neapima dalies spiečiaus šviesio, todėl jo iškaitymui naudojame pilnutinį ryškį išmatuotą  $F475W$  filtrę ir apertūrinę korekciją skaičiuojame pagal:  $F475W_{AC} = F475W_T - F475W_C$ . Mes pasirinkome  $F475W$  filtrą, nes jis turi aukštą S/N santykį, bei nėra stipriai paveiktas ryškių RGB žvaigždžių kaip  $F814W$ .

2.1 ir 3.1 pav. naudojame kaip pavyzdžius, kuriuose parodome kodėl pasirinkome atitinkamas apertūras. Pagrindinis C apertūros pasirinkimo kriterijus buvo ryškių IR žvaigždžių buvimas į šiaurę ir pietus nuo spiečiaus. Šios išskirtos lauko žvaigždės taip pat matomos ir diferencialiniame profilyje  $F814W$ ,  $F110W$ ,  $F160W$  FJ (3.1 pav.). Siekdami išvengti šių ryškių žvaigždžių itraukimo, kurios gali paveikti spiečiaus spalvą, pasirinkome mažesnę C apertūrą. Pagrindinis T apertūros pasirinkimo kriterijus buvo išvengti ryškių žvaigždžių suskirstymo ties apertūros kraštu. 3.1 pav. diferencialiniai profiliai taip pat padėjo parinkti tinkamas T apertūras, kurių spindulys nebūtų ant išskirtų žvaigždžių maksimumų. Išmatuoti T ryškiai spiečiui AP0018 visose FJ yra pavaizduoti 3.1 pav. žaliomis horizontaliomis linijomis. Žalias ir raudonos vertikalios linijos atitinka T ir C apertūrų spindulius.

## 3.3 Fotometrijos rezultatai

Gauti katalogo rezultatai su paklaidomis, 1477 spiečiams, yra pateikti 3.1 ir 3.2 lentelėse. Norėdami parodyti visą žvaigždžių spiečių apertūrinės fotometrijos imtį, toliau nagrinėjamą katalogą (N = 1477) sujungėme su Naujalis et al. (2021) publikuotu katalogu (N = 1181). Šiuos rezultatus panaudojome panagrinėti skirtumus tarp spalvos

indeksų (3.2 pav.), kurie yra gauti iš T ir C ryškių. Skirtumai tarp spalvos indeksų atsiranda dėl to, nes C apertūros buvo parinktos taip, kad išvengtų ryškiausią lauko žvaigždžių. Kiti fotometrijai įtaką darantys parametrai, tokie kaip žvaigždžių spiečių centrai, T apertūrų dydžiai ir dangaus fono lygiai, abiem apertūroms lieka tie patys. Gauti spalvos indeksų skirtumai rodo matavimų jautrumą lauko objektams ir pabrėžia šio tyrimo metu iškeltas problemas. Didžiausi skirtumai yra matomi 3.2f pav., kurie atsiranda dėl padrikai išsidėsčiusių, pavienių lauko žvaigždžių. Ryškesniems objektams šios pavienės žvaigždės neturi tokios didelės įtakos, todėl spalvų skirtumai yra mažesni. Tuo tarpu UV FJ turi mažiausią S/N santykį, dėl to padidėja sklaida blyškesniems spiečiams (3.2a pav.). Mažiausi spalvų skirtumai yra stebimi  $F336W - F475W$  spalvose (3.2b pav.), kadangi šiose FJ lauko žvaigždės turi mažiausios įtakos ir yra pakankamai didelis S/N santykis.

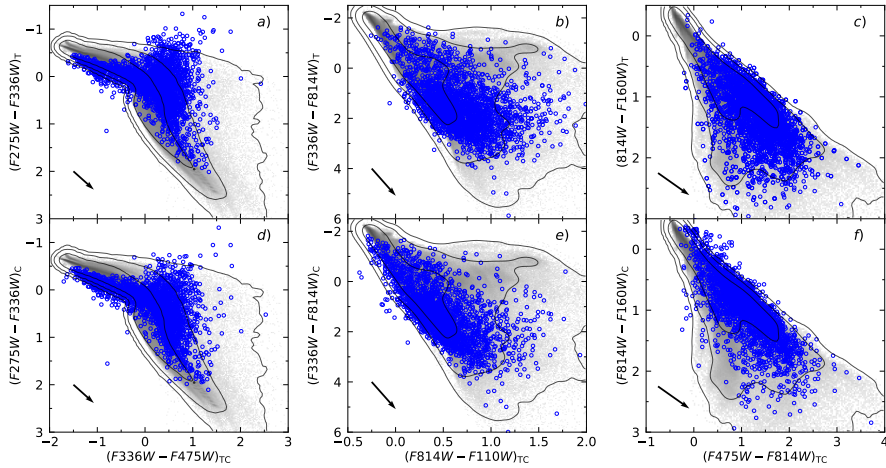


**3.2 pav.** Skirtumai tarp spalvos indeksų, gautų iš T ir C ryškių (spalvos indeksas, apskaičiuotas iš T ryškių, atinttas iš spalvos indekso, apskaičiuoto iš C ryškių).

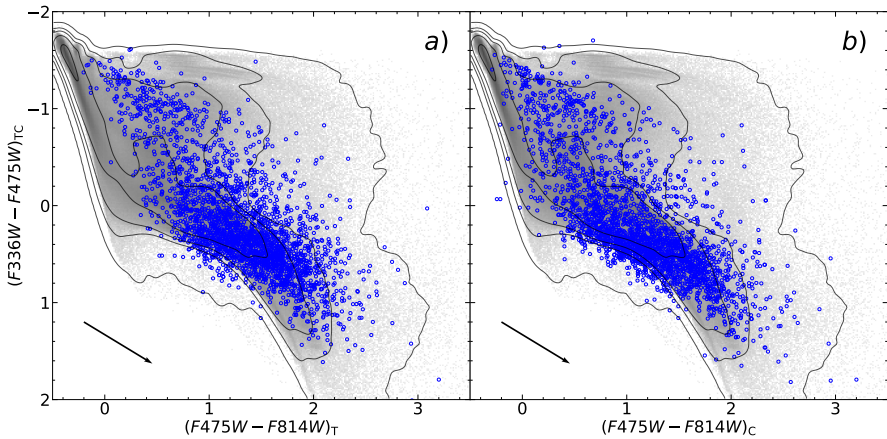
Norėdami patikrinti fotometrijos duomenų kokybę, gautus rezultatus palyginome su stochastiniai žvaigždžių spiečių modeliais, kurių amžius kinta nuo  $\log_{10}(t/\text{yr}) = 6,6$  iki 10,1, masė nuo  $10^2 M_\odot$  iki  $10^5 M_\odot$ , metalingumas [M/H] nuo  $-2,2$  iki  $+0,4$ . Modeliai buvo sugeneruoti naudojant tą pačią metodiką kaip Deveikis et al. (2008); de Meulenaer et al. (2017); Daugevičius et al. (2024), remiantis "PAdova ir tRieste Stellar Evolutionary Code" (PARSEC)-COLIBRI izochronomis<sup>1</sup> (Marigo et al. 2017). Ekstinkcijos nepaveikti modeliai yra pavaizduoti 3.3 ir 3.4 pav. pilka spalva fone.

3.3 pav. yra pateiktos įvairių kombinacijų spalvos-spalvos diagramos rezultatai T apertūrai (a-c skydeliai) ir C apertūrai (d-f skydeliai). Fone pilka spalva atvaizduoti stochastiniai spiečių modeliai. Tarpžvaigždinės ekstinkcijos vektoriai yra pavaizduoti kiekvienos panelės apačioje. Didžiausi skirtumai tarp T ir C ryškių stebimi IR FJ, kurie atsiranda dėl didesnio lauko žvaigždžių užterštumo. Taip pat jauniausią žvaigždžių spiečių C apertūros fotometriniai rezultatai yra mažiau patikimi, nes išmatuoti srautai yra labai silpni  $F110W$ ,  $F160W$  filtruose (3.3f pav.). Tuo tarpu UV spalvos

<sup>1</sup><http://stev.oapd.inaf.it/cgi-bin/cmd>



**3.3 pav.** Spalvos-spalvos diagrammos rodančios T apertūros fotometrijos rezultatus (a-c skydeliai); ir C apertūros fotometrijos rezultatus (d-f skydeliai). Fone pilka spalva yra pavaizduoti stochastiniai modeliai, kurių masės kinta nuo  $10^2$  iki  $10^5 M_{\odot}$ . Rodyklės rodo ekstinkcijos vektorius, kai  $A_V = 1$  mag.



**3.4 pav.** Spalvos-spalvos diagrammos rodančios T ir C apertūrinės fotometrijos rezultatus. Fone pilka spalva yra pavaizduoti stochastiniai modeliai, kurių masės kinta nuo  $10^2$  iki  $10^5 M_{\odot}$ . Indeksas TC rodo, kad spalvos indeksas yra skaičiuotas atitinkamai T ir C apertūrine fotometrija a ir b panelėse. Rodyklės rodo ekstinkcijos vektorius, kai  $A_V = 1$  mag.

indeksų tikslumas (3.3a,d pav.) yra apribotas dėl žemo S/N santykio. Nutolę objektai 3.3d-f pav. dažnai turi sudėtingą aplinkinį dangaus foną kurį sunku įvertinti net ir interaktyviu metodu. Taip pat spiečiai turi į C apertūras patenkančias ryškias lauko žvaigždes kurių neįmanoma išvengti. Dalis spiečių yra paveikti tarpžvaigždinės ekstinkcijos ir yra išskiriamas sistematinis spalvos indeksų poslinkis, lyginant stebimus spiečius su modeliais. 3.4a pav. pateikiami fotometrijos rezultatai, kurie gauti taikant T apertūras  $F336W$ ,  $F475W$  ir  $F814W$  FJ; 3.4b pav. fotometrijos rezultatai naudojant C apertūras. Didžioji dalis spiečių gerai dera su stochasticiais modeliais, kurie yra atidėti pilka spalva fone. Lyginant C ir T apertūrų fotometrijos rezultatus, C fotometrijos rezultatai geriau dera su žvaigždžių spiečių modeliais.

### 3.4 Stochasticiniai žvaigždžių spiečių efektai

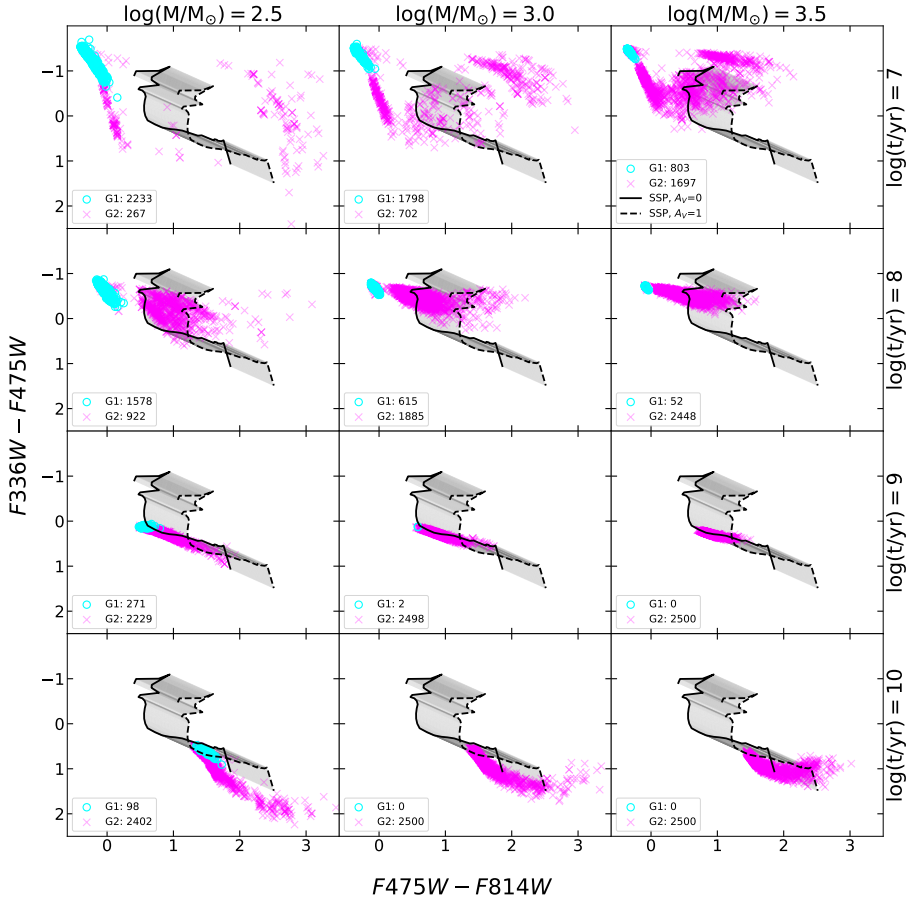
Spiečiaus žvaigždžių stochasticumas yra vienas iš pagrindinių faktorių, nuo kurių priklauso fizinių parametru tikslumas naudojant apertūrinę fotometriją. Tam tikslui, norėdami ištirti stochasticius žvaigždžių spiečių efektus apertūrinėje fotometrijoje, pa-naudojome dirbtinius spiečių modelius. Detalus spiečių modeliavimo algoritmas yra aprašytas Daugevičius et al. (2024).

Žvaigždžių spiečių mases sugeneravome pritaikant Kroupa (2001) pradinių masių funkciją (IMF), kuri nurodo žvaigždžių skaičių konkrečiame masės intervale. Žvaigždes generavome intervale, kurio ribos kinta nuo  $0,1 M_{\odot}$  iki  $100 M_{\odot}$ . Tada kiekvienai sugeneruotai žvaigždei priskyrėme ryškius, suinterpoliuodami PARSEC-COLIBRI izochronas (Marigo et al. 2017), parinkdami atitinkamo amžiaus ir masės žvaigždžių spiečiaus modelį. Visiems dirbtiniams spiečiams darėme prielaidą, kad jie yra saulės metalingumo ir su nuline tarpžvaigždine ekstinkcija. Siekiant sumodeliuoti realistiškus dirbtinius spiečius, panašius į M 31 objektus, izochronas interpolavome šešiose PHAT apžvalgos HST fotometrinėse juostose, apimančias spektrinį diapazoną nuo  $0,25$  iki  $1,6 \mu\text{m}$ .

Siekiant išnagrinėti stochasticinius efektus, nagrinėjamus objektus suskirstėme pagal amžių ir masę, naudojant spalvos-spalvos ir spalvos-ryškio diagramas (3.5 ir 3.6 pav., Daugevičius et al. 2024). Šiuose grafikuose taip pat atidėjome nestochasticinius SSP žvaigždžių spiečių modelius su saulės metalingumu (Marigo et al. 2017). 3.5, 3.6 pav. galime išskirti, kad mažos masės spiečiai ( $\log_{10}(M/M_{\odot}) \leq 4,0$ ) pasižymi didesne sklaida, kur spalvos indeksai ir srautai kinta per kelis ryškius. Toks pat efektas buvo stebimas ir Deveikis et al. (2008); Fouesneau & Lançon (2010); de Meulenaer et al. (2013) darbuose. Fotometrinį parametru sklaida yra stipresnė jaunesniems ir mažesnės masės spiečiams. Tai rodo, kad stochasticumas gali sukelti didelius ne-apibréžtumus ir išsigimimus (Worthey 1994; Bridžius et al. 2008) nustatant spiečių parametrus kaip: amžių, masę, metalingumą ir ekstinkciją. Taip pat, ryškiausi spiečiai su masėmis  $\log_{10}(M/M_{\odot}) = 2,5$  ir  $\log_{10}(M/M_{\odot}) = 3,5$ , pasižymimi panašiomis spalvomis ir ryškiaisiais nagrinėjamam spalvų ir ryškių intervale, kadangi spiečių srautą dominuoja viena arba kelios ryškios UV žvaigždės.

Mažos masės spiečiams, jaunesniems nei 1 mlrd. m., dėl stochasticumo atsiranda dvi fotometriškai skirtinės objekto grupės (3.5, 3.6 pav.). Pirmoji grupė (G1) yra sudaryta iš spiečių, kurie neturi po pagrindinės sekos (PMS) žvaigždžių, o antroji grupė (G2) apima spiečius kurie turi bent vieną PMS žvaigždę. Skirtumas tarp šių grupių yra ypač pastebimas jauniems amžiams ( $\leq 100$  mln. m) ir mažėja spiečiams senstant. G1 žvaigždžių spiečiai pasižymi nuoseklėmis ir patikimesniais fotometriniais matavimais.

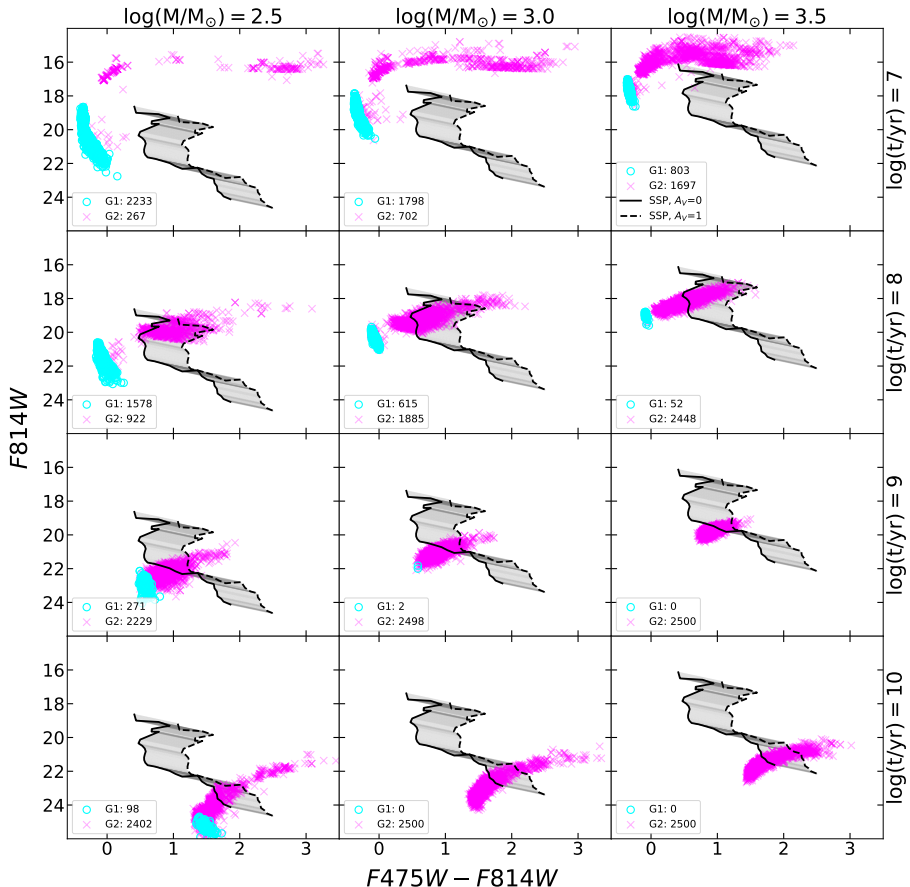
mais, užimdamis gerokai mažesnį plotą spalvos-spalvos ir spalvos-ryškio diagramose. Tuo tarpu G2 spiečiai yra raudonesni ir apima platesnį spalvos indeksų intervalą. Čia norime atkreipti dėmesį, kad mažos masės ( $\log_{10}(M/M_\odot) \leq 4,0$ ) spiečiamams reikšmingi fotometriniai skirtumai tarp šių dviejų grupių atsiranda dėl kelių, o dažniausiai – vienos ryškios PMS žvaigždės, kurios srautas dominuoja prieš likusią spiečiaus šviesą. Šie rezultatai atitinka Beerman et al. (2012) išvadas ir rodo, kad patikima spiečių fotometrija su fiziniiais parametrais gali būti gauta tiksliau, jei šios ryškios žvaigždės yra pašalinamos arba jų išvengiama atliekant apertūrinę fotometriją.



**3.5 pav.** Spalvos-spalvos diagramos dirbtiniams žvaigždžių spiečiams (Daugevičius et al. 2024). Kiekvienoje panelėje yra parodytai apertūrinės fotometrijos rezultatai skirtingo amžiaus ir masės grupėms. G1 grupė nurodo, kad šie spiečiai neturi PMS žvaigždžių; G2 grupė nurodo spiečius kurie turi bent vieną PMS žvaigždę. Juodos linijos (ištisinės – be tarpžvaigždinės ekstinkcijos; punktyrinės –  $A_V = 1$ , naudojant Fitzpatrick 1999 ekstinkcijos kreivę) PARSEC-COLIBRI nestochastiniai SSP modeliai su saulės metalingumu (Marigo et al. 2017), kurių amžius kinta nuo 10 mln. m. iki 12,6 mlrd. m. Matavimai yra atlirkinti naudojant  $R_{ap} = 3,0$  arcsec spindulio apertūrą.

Toliau kiekvienoje panelėje atidėjome SSP modelius (3.5, 3.6 pav.) ir parodėme,

kad su jais negalime nustatyti tikslų parametrų mažos masės ir jauniems spiečiams. SSP modeliai yra pasiskirstę srityse tarp dviejų grupių (G1 ir G2), kur stochastinių modelių nėra daug. Žinoma, reikėtų pabrėžti ir tai, kad SSP modeliai gan gerai sutampa su stochastiniais modeliais, kai spiečių amžius  $>1$  mldr. m.



**3.6 pav.** Tas pats kaip 3.5 pav., tik yra pavaizduotos spalvos-ryškio diagrammos.

### 3.5 Apibendrinimas

Atlikome daugiaspalvę apertūrinę fotometriją 1477 žvaigždžių spiečiams, naudojant M 31 galaktikos PHAT apžvalgos (Dalcanton et al. 2012; Johnson et al. 2012, 2015) objektus. Fotometrijai naudojome dvi apertūras: pilnuitinę (T) ir spalvinę (C). T ir C apertūrų fotometrijos rezultatų katalogo ištrauka pateikta 3.1 ir 3.2 lentelėse.

3.4 pav. pateikėme spalvos-spalvos diagramą, kurioje yra pavaizduoti adaptyvios apertūrinės fotometrijos matavimai visai PHAT apžvalgos spiečių imčiai (iš viso 2658 objektais). Čia išskyrėme du svarbius aspektus: mūsų fotometrijos rezultatai gerai dera su stochastiniais spiečių modeliais; T fotometrijos rezultatai (3.4a pav.) žymiai skiriasi nuo C fotometrijos rezultatų (3.4b pav.).

Taip pat, norime pabrėžti dvi pagrindines problemas, susijusias su žvaigždžių spiečių fotometrijos metodu, kurios riboja rezultatų tikslumą tankiose srityse: (i) dangaus fono nustatymo neapibrėžtumai ir (ii) lauko žvaigždžių projekcija į apertūras. Todėl tikslūs apertūrinės fotometrijos rezultatai M 31 diske gali būti garantuojami tik kruopščiai įvertinus minėtas problemas.

Mes parodėme, kad spiečių su PMS žvaigždėmis (G2) fotometriniai rezultatai ženkliai skiriasi lyginant su spiečiais, kuriuose nėra PMS žvaigždžių (G1). G2 spiečiai pasižymi didesne sklaida fotometrinėje erdvėje ir didesniais matavimų neapibrėžtumais. Mūsų išvados sutampa su Beerman et al. (2012), rodydamos, kad PMS žvaigždžių nebuvis duoda nuoseklesnius ir geriau apibrėžtus spiečių fotometrinius parametrus, kas savo ruožtu leidžia patikimiau nustatyti fizinius parametrus.

## Skyrius 4

# Žvaigždžių spiečių parametrai

Žvaigždžių spiečių parametrų (amžius, masė, metalingumas ir ekstinkcija) nustatymui panaudojome pilną 2658 objektų katalogą su fotometriniais duomenimis pristatytais šiame darbe ir Naujalis et al. (2021).

### 4.1 Parametrų nustatymas

Žvaigždžių spiečių parametrus nustatėme taikydami de Meulenaer et al. (2013, 2014, 2017) metodiką, kur objektų fotometrinius matavimus lyginame su stochastinių modelių tinkleliu. Modelių paruošimui buvo priimtas atstumo modulis  $(m - M)_0 = 24,47$  (McConnachie et al. 2005), standartinis Galaktikos tarpžvaigždinės ekstinkcijos dėsnis su  $R_V = 3,1$ , žvaigždžių raidos modeliai iš PARSEC-COLIBRI v1.2S (Marigo et al. 2017), bei Kroupa (2001) IMF. Naudojamas modelių tinklelis apima šiuos parametru intervalus: amžius,  $\log_{10}(t/\text{yr})$  nuo 6,0 iki 10,3 kas 0,02 žingsniu; masė,  $\log_{10}(M/M_\odot)$  nuo 2 iki 7 kas 0,05 žingsniu; metalingumas, [M/H] nuo  $-2,2$  iki  $+0,7$  kas 0,1 žingsniu; tarpžvaigždinė ekstinkcija,  $E(B - V)$  nuo  $-0,03$  iki  $2,00$  kas 0,01 žingsniu. Neigiama ekstinkcija yra įskaitoma dėl to, nes prieš lyginimą su modeliais visi stebėjimai yra atbalinami vidutine Galaktikos ekstinkcija. Kiekviename tinklelio mazge su konkrečiu parametru rinkiniu yra po 10 000 modelių.

Spiečių parametrus nustatėme remdamiesi C ir T apertūrinės fotometrijos rezultatais, naudodami penkias skirtinges filtrių kombinacijas, kurios apibrėžiamos taip: F0 – naudoti visi šeši WFC3+ACS filtrai; F1 – pašalintas  $F275W$  filtras; F2 – pašalinti  $F275W$  ir  $F336W$  filtrai; F5 – pašalintas  $F110W$  filtras; F6 – pašalinti  $F110W$  ir  $F160W$  filtrai. Kiekvienam mazgui, kuriam atrenkamas bent vienas stebėjimus atitinkantis modelis, yra apskaičiuojama tikimybė kuri lygi visų atrinktų modelių tikimybių sumai. Vieno modelio tikimybė (de Meulenaer et al. 2017) yra apibrėžiama:

$$L_{\text{model}} = \prod_{f=1}^F \frac{1}{\sqrt{2\pi} \sigma_f} \exp \left[ -\frac{(\text{mag}_{f,\text{obs}} - \text{mag}_{f,\text{model}})^2}{2\sigma_f^2} \right], \quad (4.1)$$

kur  $f$  – konkretus PHAT apžvalgos filtras,  $\text{mag}_{f,\text{obs}}$  ir  $\text{mag}_{f,\text{model}}$  – stebėjimų ir modelių ryškiai konkretiame filtre,  $F$  – naudojamų fotometrinijų juostų skaičius. Tada viso mazgo tikimybė, su konkretiu amžiumi, mase, ekstinkcija ir metalingumu, yra lygi:

$$L_{\text{node}}(t, M, E(B-V), [\text{M/H}]) = \sum_{n=1}^N L_{\text{model}, n}, \quad (4.2)$$

kur  $N$  – atrinktų modelių skaičius mazge. Parametru rinkinys atitinkantis didžiausią tikimybę turintį mazgą, žymimas BEST indeksu. Su saulės metalingumu didžiausią tikimybę turintis mazgas yra BESTsun. Taip pat konkretaus parametru histogramas maksimumas yra žymimas MAX indeksu (4.1 pav.).

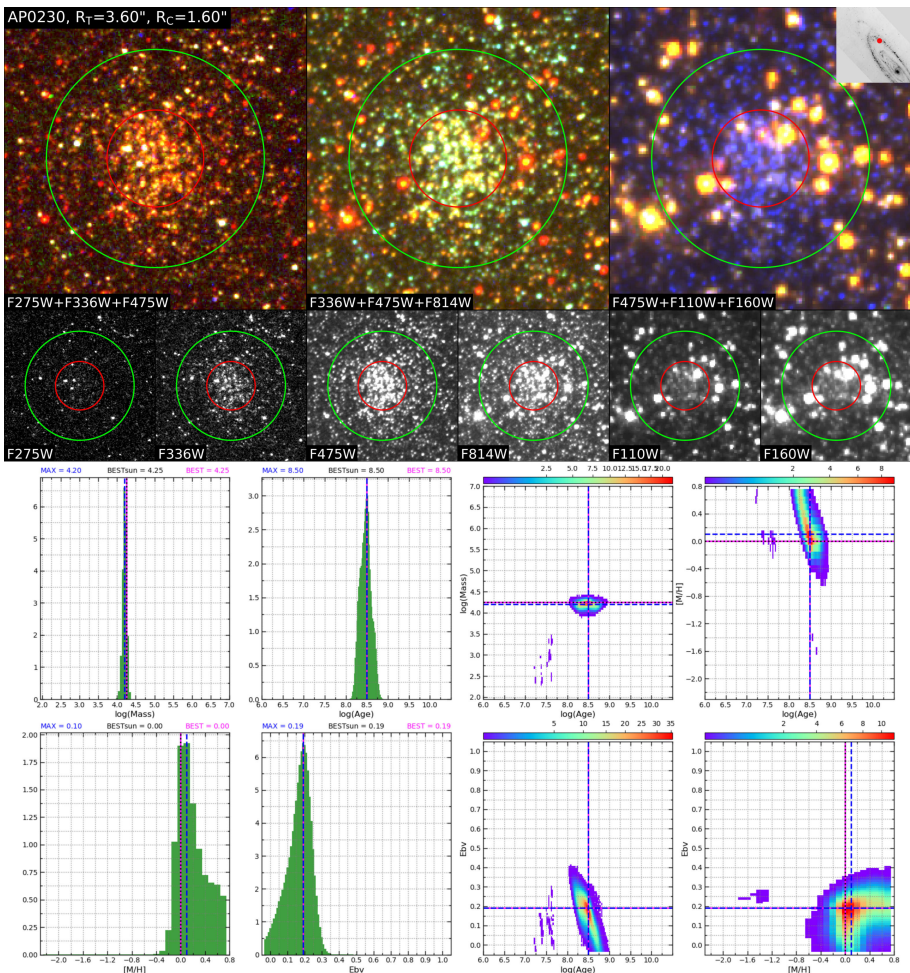
Galutinius parametru rinkinius nustatėme nagrinėjant spiečių nuotraukas ir jų tikimybinės histogramos su dvimačiais tankio žemėlapiais. Kiekvienai filtrų kombinacijai sudaryti grafikai buvo tarpusavyje lyginami ir vertinami kartu su spiečių vaizdais, o C ir T apertūrinės fotometrijos rezultatai analizuoti atskirai (žr. 4.1 pav. F0 atvejį su C apertūra). Pagrindinis šios interaktyvios procedūros tikslas buvo užtikrinti kuo tikslesnį parametru įvertinimą, kadangi gautos reikšmės gali būti paveiktos įvairių veiksniių kaip: (i) spiečiaus padėtis dulkių juostos atžvilgiu; (ii) ryškių UV ir IR lauko žvaigždžių buvimas C ir T apertūrose.

4.1 pav. turime AP0230 spiečiaus atvejį. Šis objektas yra tankiamė ryškių mėlynų ir raudonų žvaigždžių lauke. Kelios ryškios lauko žvaigždės yra matomos  $F814W$ ,  $F110W$  ir  $F160W$  FJ, kurios patenka į C ir T apertūras, paveikdamos objekto fotometrinius matavimus ir, atitinkamai, spiečiaus parametrus. Kadangi šios žvaigždės turi panašias spalvas palyginus su lauko objektais, mes padarėme išvadą, kad jos greičiausiai spiečiui nepriklauso. Tad toliau pasirinkome nagrinėti C apertūrą su F0 filtrų kombinacija ir BESTsun sprendiniu, kur buvo gautas 300 mln. m. amžius, kuris atrodo tinkamas tokio tipo spiečiams. Taip pat BEST, BESTsun ir MAX parametrai tarpusavyje sutampa šiam objektui, kas patvirtina mūsų amžiaus pasirinkimą. Atsižvelgiant į modelių skaičių ir amžiaus parametrą, toliau atitinkamai nustatėme masės ir spalvos eksceso vertes. Sudėtingesniais atvejais interaktyvi analizė yra būtina, norint nustatyti spiečiaus parametrus kuo tiksliau.

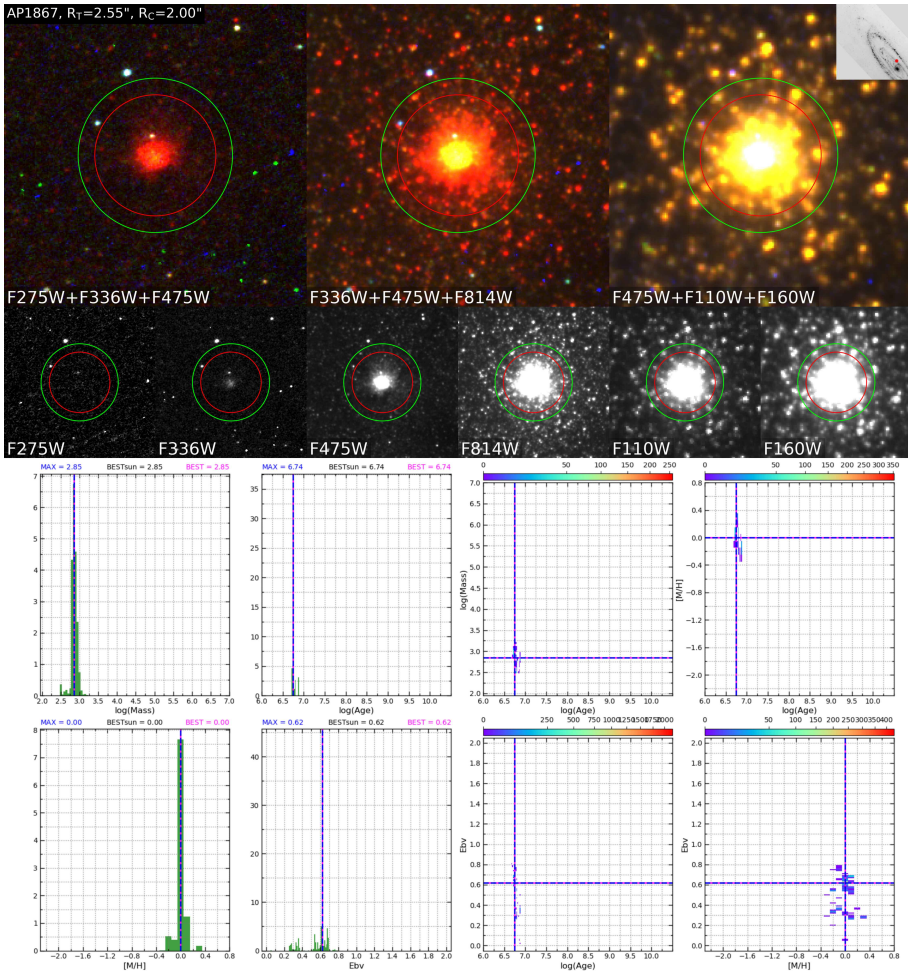
Kitas atvejis į kurį norime atkreipti dėmesį yra AP1867 (4.2 pav.). Šis objektas yra stipriai paveiktas ekstinkcijos ir tikėtina, kad jis projektuoja už M 31 žvaigždėdaros žiedo. Be to, jaunos, masyvios žvaigždės, kurios yra ryškios UV dalyje, patenka į C ir T apertūras taip paveikdamos parametru nustatymo rezultatus, dėl kurių spiečius automatiškai klasifikuojamas kaip jaunas objektas. Tokie atvejai iš tolimesnės analizės buvo pašalinti, kadangi jų parametrai negali būti nustatyti su aukštu tikslumu.

Nustatę spiečių parametrus, pašalinome 733 objektus, kurių amžius viršija 800 mln. m. Šiemis spiečiams negalėjome priskirti saulės metalingumo ir jų apertūrose projektyuojasi ryškios, spiečiui nepriklausančios žvaigždės. Tad galutinę spiečių imtį su parametrais – amžius, masė, spalvos ekscesas – sudaro 1922 objektais. Gauti katalogo rezultatai yra pateikti 4.1 lentelėje. Kiekvienam spiečiui yra nurodyta parametru tikslumo ( $\delta$ ) grupė ( $Q$ ), kuri galioja visiems parametrams ir yra apibrėžiama taip:  $Q = 0$  ( $\delta \leq 0,08$ );  $Q = 1$  ( $0,08 < \delta \leq 0,12$ );  $Q = 2$  ( $0,12 < \delta \leq 0,20$ );  $Q = 3$  ( $\delta > 0,20$ ).

Johnson et al. (2022) ir Daugevičius et al. (2024) parodė, kad jauniems žvaigždžių spiečiams ( $\lesssim 40$  mln. m.) parametru negalime patikimai nustatyti naudojant apertūrinę fotometriją. Todėl jauniausiems spiečiams pritaikėme tikimybinį CMD metodą, kur nustatėme žvaigždžių spiečių amžių ir ekstinkciją, pritaikydami teorines izochronas prie išskirtų spiečiaus žvaigždžių (Čeponis et al. 2024). CMD metodu parametrai buvo nustatyti 426 spiečiams. Visais atvejais buvo fiksotas saulės metalingumas, o spiečiaus masė nustatyta naudojant stochastinius modelius.



**4.1 pav.** Viršutinė panelė: spiečiaus AP0230 nuotrauka su įvairiomis filtrų kombinacijomis (viršuje) ir visose šešiose fotometrinėse juostose (apačioje). Fotometriniių juostų pavadinimai ir kombinacijos pateiktos nuotraukų apatinėje dalyje. Žalias ir raudonais apskritimais žymi T ir C apertūras atitinkamai. Kiekvienos nuotraukos dydis  $10'' \times 10''$ . Intarpas nuotraukos viršuje rodo spiečiaus poziciją M 31 galaktikoje. Apatinė panelė: spiečiaus AP0230 klasifikacijos histogramos ir dvimačiai tankio žemėlapiai. Spalvos atitinka atrinktą modelių skaičių. Raudonesnės spalvos atitinka didesnį modelių skaičių, mėlynesnės – mažesnį. Nubrėžtos tiesės rodo suskaičiuotą sprendinį: BEST (rožinė), BESTsun (juoda), MAX (mėlyna). Nustatyti spiečiaus parametrai: amžius –  $\log_{10}(t/\text{yr}) = 8,50$ , masė –  $\log_{10}(M/M_\odot) = 4,25$ , spalvos ekscesas –  $E(B - V) = 0,19$ , metalingumas –  $[\text{M}/\text{H}] = 0,0$ .



**4.2 pav.** Tas pats kas 4.1 pav., tik spiečiui AP1867. Šis objektas projektuoja už žvaigždėdaros žiedo, dėl to jis yra paveiktas tarpžvaigždinės ekstinkcijos. Dėl mažo parametru tikslumo, šis spiecius iš tolimesnės analizės buvo pašalintas.

#### 4.1 lentelė. M 31 galaktikos žvaigždžių spiečių parametrai.

AP <sup>(a)</sup>	R.A.(2000) <sup>(b)</sup>	DEC(2000) <sup>(b)</sup>	$\log_{10}(t/\text{yr})^{(c)}$	$\log_{10}(M/M_\odot)^{(d)}$	$E(B - V)^{(e)}$	$R_{50}^{(f)}$	$Q^g$
0001	11,43552	41,69856	8.80	4,35	0,06	0,56	0
0002	11,36651	41,70101	8,56	3,80	0,27	0,59	2
0003	11,47129	42,04925	8,44	3,30	0,21	0,74	1

**Pastabos.** Lentelėje pateikta tik dalis pirmų trijų spiečių duomenų. <sup>(a)</sup> identifikacijos numeris (Johnson et al. 2015); <sup>(b)</sup> pusiaujinės koordinatės laipsniais (Naujalis et al. 2021; Kriščiūnas et al. 2023); <sup>(c)</sup> amžius; <sup>(d)</sup> masė; <sup>(e)</sup> spalvos ekscesas; <sup>(f)</sup> pusės šviesio spindulys kampinėms lanko sekundėms; <sup>(g)</sup> kokybės parametras.

## 4.2 Žvaigždžių spiečių savybės

Žvaigždžių spiečių masės priklausomybė nuo amžiaus yra parodyta 4.3a pav. Čia raudonos linijos žymi spiečių aptikimo ribas ties  $F475W < 21,5$  mag ir  $F475W < 22,5$  mag. Šios aptikimo ribos buvo suskaičiuotos naudojant saulės metalingumo SSP modelius be ekstinkcijos. Čia reikėtų pabrėžti, kad tikroji aptikimo riba stipriai priklauso nuo konkrečios objekto ekstinkcijos vertės ir aplinkoje esančio lauko žvaigždžių tankio.

Spiečių masės (4.3a pav.) kinta nuo  $\sim 200 M_{\odot}$  iki  $\sim 30 000 M_{\odot}$ . Spiečių skaičiaus sumažėjimas mažos masės srityje yra dėl selekcijos efektų. Kuo mažesnė objekto masė, tuo yra sunkiau ji aptikti. Tuo tarpu didesnės masės spiečių ( $\log_{10}(M/M_{\odot}) > 4,5$ ) mūsų nagrinėjome imtyje beveik nėra, nes mes nagrinėjame objektus jaunesnius nei 800 mln. m., kur yra pašalinti didelės masės kamuoliniai spiečiai. Tačiau spiečių aptikimas ties  $\sim 2000 M_{\odot}$  neturėtų būti iškraipytas selekcijos efektų (Daugevičius et al. 2025). Tokių objektų aptikimas turi būti pakankamai geras norint priderinti spiečių masės funkciją. Taip pat jauni ( $\lesssim 100$  mln. m.) ir masvyūs ( $\gtrsim 10 000 M_{\odot}$ ) spiečiai daugiausiai yra žvaigždžių asociacijos.

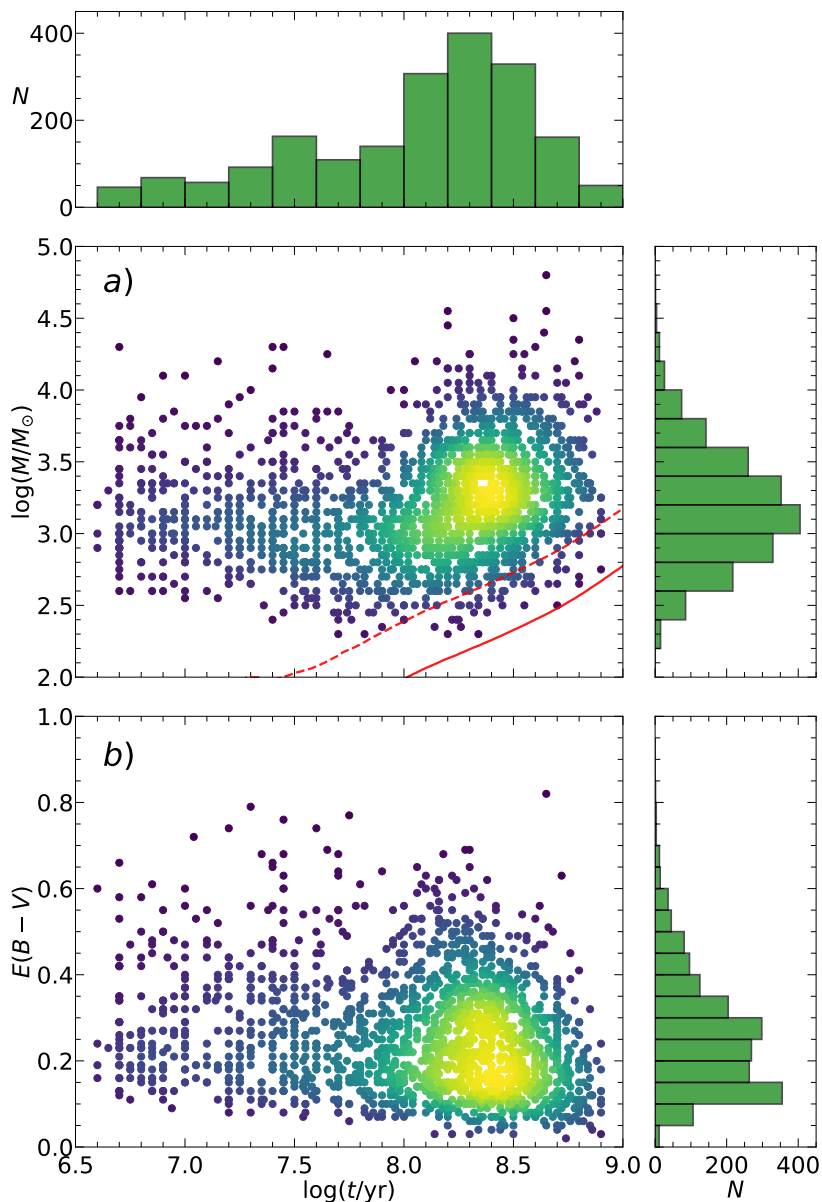
Spiečių spalvos eksceso priklausomybė nuo amžiaus yra parodyta 4.3b pav. Medianinė spalvos eksceso vertė yra  $E(B - V) \sim 0,24$ . Septyni objektai pasižymi aukštomas spalvos eksceso vertėmis,  $E(B - V) > 0,7$  (4.3b pav.). Šeši iš jų yra jaunesni nei 100 mln. m. ir jie yra išsidėstę žvaigždėdaros regionuose. Dalis senesnių ( $> 100$  mln. m.) spiečių taip pat pasižymi aukštėsnėmis ekstinkcijos vertėmis ( $E(B - V) \gtrsim 0,6$ ). Šie objektai greičiausiai yra kitoje galaktikos pusėje, užstoti tankios difuzinės medžiagos sluoksniu. Be to, nustatėme, kad individualaus spiečiaus  $E(B - V)$  labiau priklauso nuo vietinės tarpžvaigždinės aplinkos nei nuo radialinio atstumo iki M 31 centro. Tačiau norime pabrėžti ir tai, kad diferencialinė ekstinkcija konkretiam spiečiui nėra išskiriamā. Kai kuriais atvejais, ypač jauniems spiečiams kurie yra nehomogeniškuose dulkių debesyse, diferencialinė ekstinkcija gali stipriai iškraipyti nustatytais parametrus.

## 4.3 Spiečių masės funkcija

Spiečių masės funkcija yra gerai aprašoma Schechter įvesta forma (Schechter 1976; Gieles 2009):

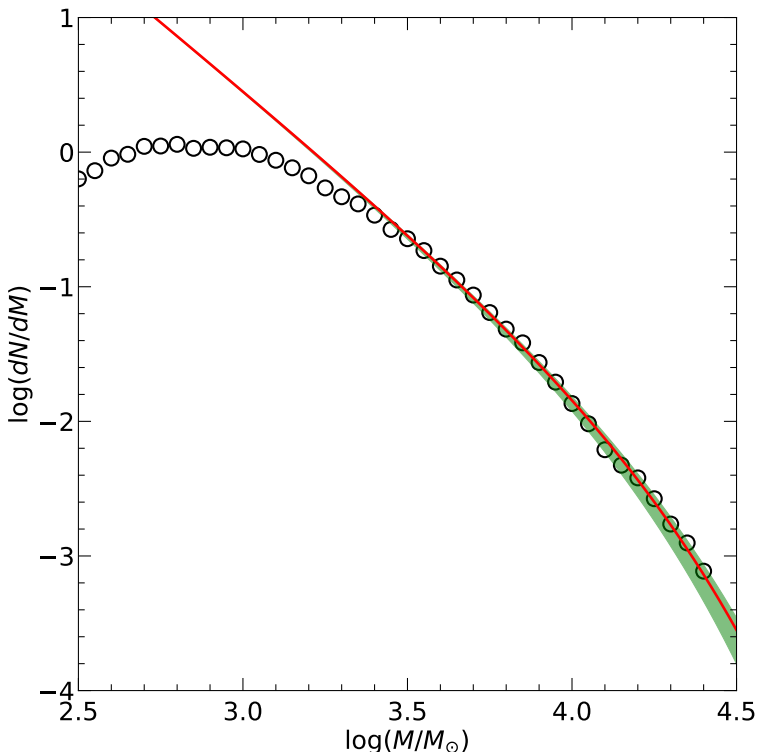
$$\frac{dN}{dM_i} = AM_i^{-\alpha} \exp\left(-\frac{M_i}{M_C}\right), \quad (4.3)$$

kur  $M_C$  – charakteringa masė ties kuria įvyksta lūžis ir funkcija pradedą eksponentiškai mažėti,  $A$  – normavimo konstanta,  $\alpha$  – laipsnio rodiklis kuris nurodo mažos masės spiečių santykinę gausą. Atsižvelgus į kitų autorų darbus Zhang & Fall (1999); Gieles et al. (2006); Larsen (2009); Portegies Zwart et al. (2010); Fall & Chandar (2012); Krumholz et al. (2019), laipsnio rodiklį  $\alpha$  fiksavome ties 2, bei nustatėme globalią charakteringos masės vertę M 31 žvaigždžių spiečiams. Diferencialinis masės pasiskirstymas yra parodytas 4.4 pav., kur prie nagrinėjamų spiečių priderinome masės funkciją, parinkdami objektus masyvesnius nei  $\sim 2500 M_{\odot}$ . Gauta charakteringa vertė  $-M_C = (13,3^{+1,3}_{-2,6}) \cdot 10^3 M_{\odot}$ . Šis rezultatas yra didesnis palyginus su Johnson et al. (2017) nustatyta verte  $M_C = (8,5^{+2,8}_{-1,8}) \cdot 10^3 M_{\odot}$ . Ši neatitinkamą galima paaiškinti tuo,



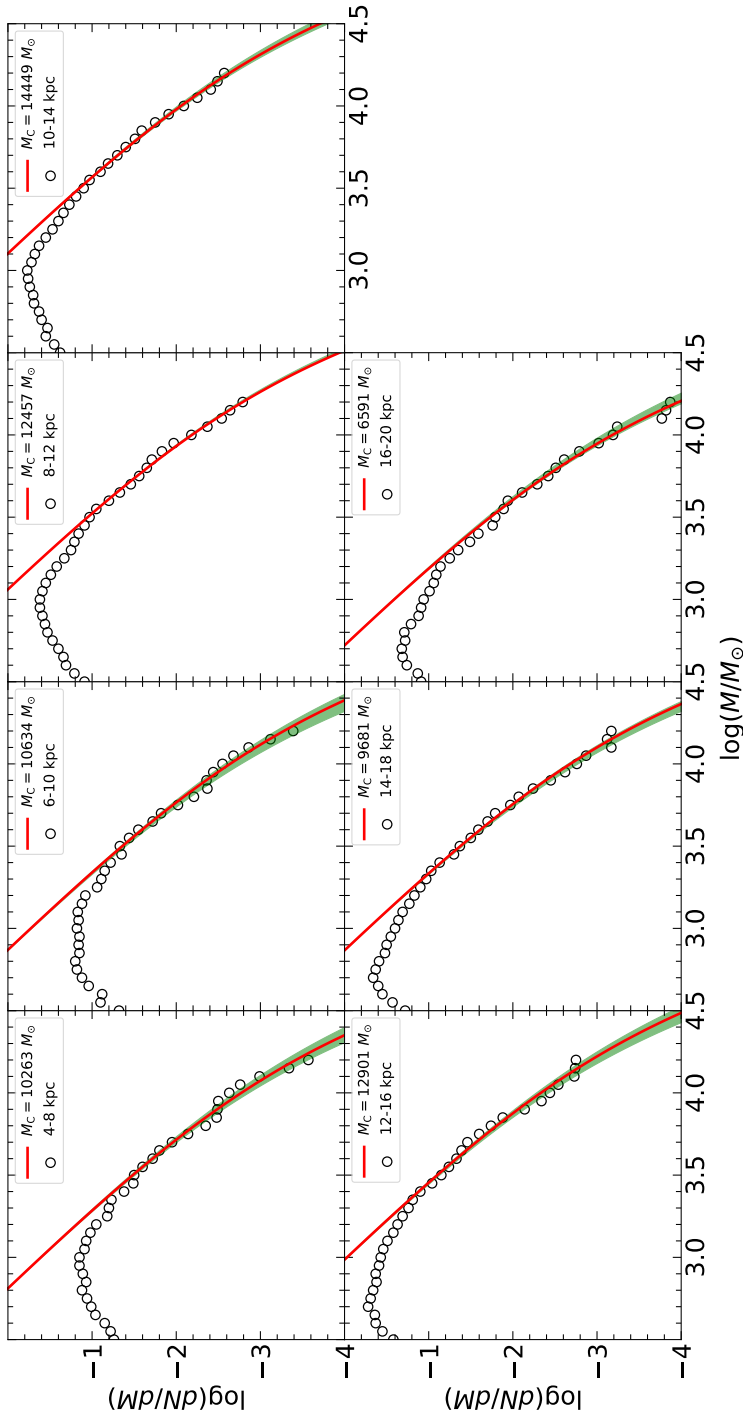
**4.3 pav.** Spiečių masės (a) ir spalvos eksceso (b) priklausomybė nuo amžiaus. Linijos rodo spiečių aptikimo ryškio ribas:  $F475W < 21,5$  mag (brūkšninė) ir  $F475W < 22,5$  mag (ištisinė).

kad jie analizavo spiečius jaunesnius nei 300 mln. m. Tuo tarpu mūsų imtis įtraukia objektus iki 800 mln. m.

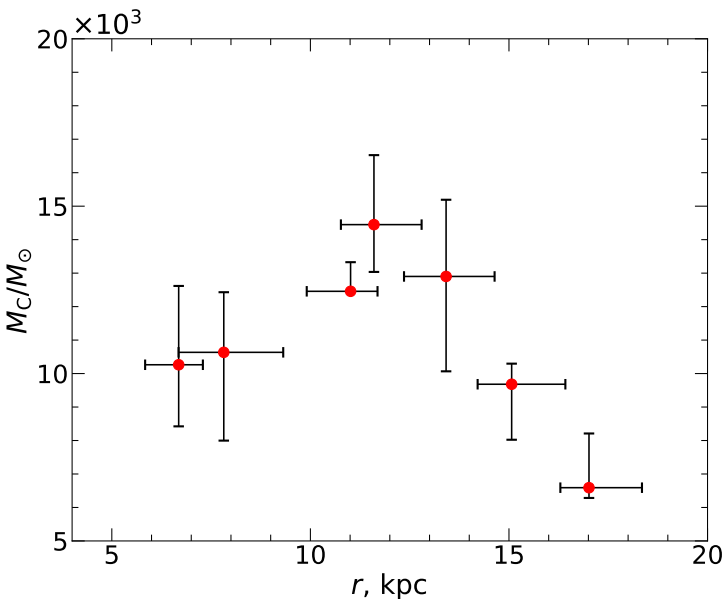


**4.4 pav.** Žvaigždžių spiečių diferencialinis masės pasiskirstymas. Raudona linija rodo priderintą Schechter funkciją su charakteringa mase –  $M_C = (13, 3^{+1,3}) \cdot 10^3 M_\odot$ . Žalia zona nurodo neapibrėžtumo intervalą aplink prideriną kreivę.

Toliau įvertiname kaip spiečių masės funkcija kinta tolstant nuo galaktikos centro. Tam tikslui nagrinėjamus objektus sugrupavome į 4 kpc pločio segmentus, einant nuo 4 iki 20 kpc. Pradedant nuo pirmo segmento, mes priderinome masės funkciją. Kaip ir praeitu atveju, siekdami užtikrinti katalogo pilnumą (Daugevičius et al. 2025), masės funkciją priderinome prie spiečių kurių masė viršija  $\sim 2500 M_\odot$ . Tada nagrinėjamas segmentas buvo pastumtas per 2 kpc ir procedūra kartojama kol pasiekiamas 20 kpc vertė. 4.5 pav. pateikiame kiekvieno segmento diferencialinį masės pasiskirstymą su priderinta masės funkcija. Gautas  $M_C$  vertes toliau atidėjome nuo radialinio atstumo (4.6 pav.), kur buvo imtos spiečių atstumų medianos konkrečiame žiede. Čia išskyrėme, kad  $M_C$  priklauso nuo galaktikos aplinkos. Didesnės vertės yra stebimos 10-14 kpc žvaigždėdaros regione dėl didesnio dujų tankio, kur atitinkamai yra formuojami masyvesni spiečiai. Tuo tarpu išoriniame galaktikos žiede, ties 16-20 kpc,  $M_C$  vertė sumažėja. Išoriniuose regionuose spiečiai yra mažiau paveikti kitų masyvių objektų galaktikos diske, kas leidžia išgyventi mažos masės spiečiams. Radialinė  $M_C$  priklausomybė taip pat buvo analizuota ir M 83 galaktikoje (Adamo et al. 2015), kur buvo parodyta, kad galaktikos aplinka reguliuoja viršutinę masės funkcijos ribą.



**4.5 pav.** Žvaigždžių spiečių diferencialiniai masės pasiskirstymai 4 kpc pločio segmentuose. Raudonos linijos rodo priderintą Schechter masės funkciją su charakteringa masės vete nurodyta legendoje. Žalia zona nurodo neapibrėžtumo intervalą aplink prideriną kreivę.

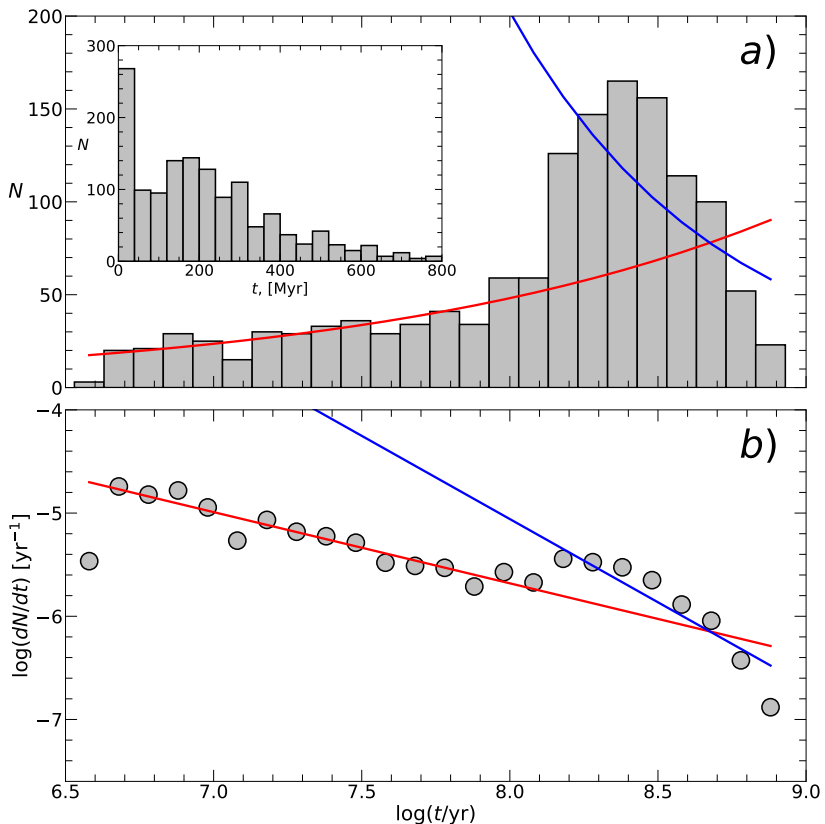


**4.6 pav.** Charakteringos masės ( $M_C/M_\odot$ ) radialinė priklausomybė M 31 galaktikoje. Y-axies vertės yra padaugintos iš  $10^3$ . Vertikalios linijos žymi min-max  $M_C$  paklaidas. Horizontalios linijos žymi 16-84 procentilius. Kiekvienu atveju Schechter funkcija buvo priderinta prie spiečių, kurie yra 4 kpc pločio žiede, su 2 kpc žingsniu, padengiant radialinius atstumus nuo 4 iki 20 kpc (žr. 4.5 pav.).

## 4.4 Spiečių formavimosi istorija

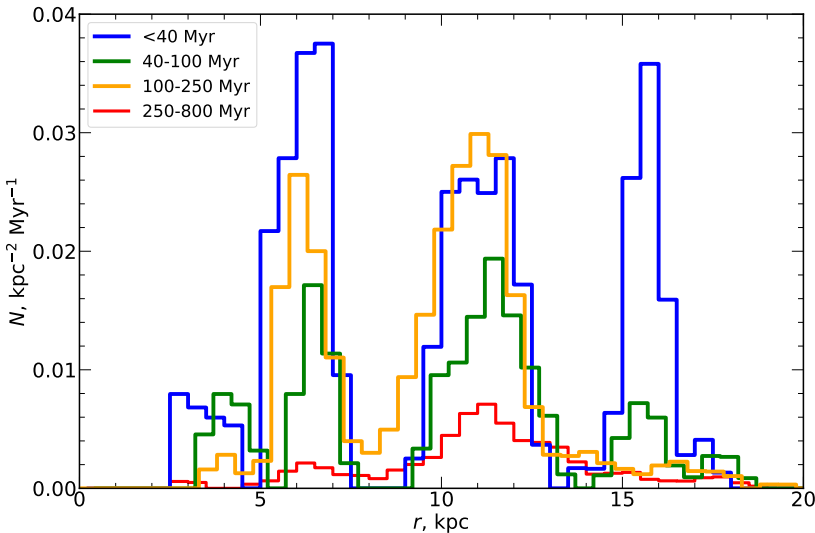
Diferencialinis žvaigždžių spiečių amžiaus pasiskirstymas yra pateikiamas 4.7 pav. Čia įtraukėme spiečius masyvesnius nei  $1000 M_\odot$  norint išvengti selekcijos efekto platiame amžiaus intervale. Diferencialinis skirstinys yra gan gerai apibūdinamas evoliuciniu blausimo (raudona kreivė) ir suardymo (mėlyna kreivė) modeliais (Boutloukos & Lamers 2003), kurių polinkio koeficientai yra paimti iš Vansevičius et al. (2009) ( $\alpha = 2.0$ ,  $\zeta = 0.69$ ,  $\gamma = 0.62$ ). Spiečių skaičiaus pasiskirstymas,  $dN/dt$ , bendru atveju atitinka evoliucinį blausimo modelį. Per pastaruosius  $\sim 100$  mln. m. spiečių formavimasis vyko gan pastoviai. Adamo et al. (2015) taip pat pabrėžė, kad daugelyje stebėjimais grįstų tyrimų spiečių amžiaus funkcija rodo beveik pastovų pasiskirstymą iki  $\sim 100$  mln. m., o viršijus šią ribą yra stebimas žymus sumažėjimas, kuris gali būti paaiškinamas spiečių ardymu ir nagrinėjamos imties nepilnumu. Nuo  $\sim 130$  mln. m. spiečių skaičius pradėjo didėti ir pasiekė piką ties  $\sim 200$  mln. m. Toliau spiečių skaičius nuo  $\sim 300$  mln. m. pradedė mažėti. Tai rodo, kad yra būdingas charakteringas spiečių ardymo laikas, kuris gali būti ilgesnis nei 500 mln. m. Visgi, dėl sustiprėjusio spiečių formavimosi ties tuo pačiu amžiumi, charakteringa ardymo vertė negali būti tiksliai įvertinta. Palyginimui, Lamers et al. (2005) pateikė šiuos būdingus spiečių ardymo įverčius kitose galaktikose:  $\sim 70$  mln. m. M 51 centrinėje srityje,  $\sim 630$  mln. m. M 33 galaktikoje,  $\sim 560$  mln. m. Paukščių Tako saulės aplinkoje ir  $\sim 8$  mlrd. m. Mažame Magelano Debesyje.

4.7 pav. išsiskiria žvaigždėdaros suaktyvėjimo pikas ties  $\sim(200 \pm 50)$  mln. m.



**4.7 pav.** Viršuje: žvaigždžių spiečių amžių pasiskirstymas masyvesniems nei  $1000 M_{\odot}$  objektams. Intarpas vaizduoja tą pačią spiečių amžiaus sklaidą tiesinėje skaleje. Apačioje: tos pačios imties diferencialinis amžių pasiskirstymas. Raudona ir mėlyna linijos rodo spiečių evoliucinio blausimo ir suardymo funkcijas. Tiesių polinkio koeficientai yra paimti iš Vansevičius et al. (2009).

Šis epizodas galėjo būti sukeltas dėl sąveikos su kaimynine galaktika M 32 (Gordon et al. 2006; Block et al. 2006; Dierickx et al. 2014). Gordon et al. (2006) ir Dierickx et al. (2014) pasiūlė, kad susidūrimas įvyko atitinkamai prieš 20 mln. m. ir 800 mln. m. Tuo tarpu Block et al. (2006) iškėlė hipotezę, kad M 32 perėjo per M 31 centrą prieš maždaug 210 mln. m., dėl ko diske susidarė stebima žiedinė struktūra. Be to, Vansevičius et al. (2009) pietvakarinėje galaktikos dalyje nustatė išskiriantį spiečių formavimosi piką ties  $\sim 70$  mln. m., kurį šiame scenarijuje galėjo sukelti antrasis perėjimas per galaktikos diską. Taip pat, Lewis et al. (2015) ir Williams et al. (2017) tyrimai rodo, kad M 31 galaktikos žiedinė struktūra yra ilgalaikė, senesnė nei  $\sim 500$  mln. m., todėl stebimos struktūros kilmė neturėtų būti susijusi vien tik su galaktikos susidūrimu. Nepaisant to, mes siūlome, kad spiečių formavimosi spartos padidėjimą prieš  $\sim 200$  mln. m. vis tik galėjo sukelti sąveika su M 32 pagal scenarijų kurį pasiūlė Block et al. (2006), tačiau tuo metu žiedinė struktūra jau galėjo būti susiformavusi. Detalesnė PHAST apžvalgos analizė turėtų suteikti daugiau įžvalgų, ar M 32 iš tiesų buvo atsakinga už padidėjusią spiečių formavimosi spartą.



**4.8 pav.** Masyvių ( $\geq 1000 M_{\odot}$ ) žvaigždžių spiečių skaičiaus paviršinio tankio priklausomybė nuo radialinio atstumo. Pasiskirstymai skaičiuoti  $60^{\circ}$  segmente (nuo  $-25^{\circ}$  iki  $+35^{\circ}$ ) aplink didžiąją ašį. Histogramos yra pastumtos pagal X-aštį dėl matomumo. Naudojami spiečių populiacijos amžiaus intervalai yra nurodyti legendoje.

## 4.5 Erdvinis pasiskirstymas

Norëdami panagrinėti spiečių erdvinį pasiskirstymą, deprojektavome M 31 galaktikos diską. Disko deprojektavimui pritaikėme pozicinių didžiosios ašies kampą  $37,7^{\circ}$  (Chemin et al. 2009) ir diskų polinkį  $77,5^{\circ}$  (van der Marel et al. 2019). Gautas koordinates panaudojome suskaičiuoti kiekvieno objekto atstumą iki galaktikos centro. 4.8 pav. turime spiečių paviršinio tankio priklausomybę nuo radialinio atstumo. Čia spiečius suskirstėme į keturias amžiaus grupes azimutiniame  $60^{\circ}$  segmente (nuo  $-25^{\circ}$  iki  $+35^{\circ}$  aplink pagrindinę ašį). Jaunesni (<250 mln. m.) spiečiai radialine kryptimi koncentruojasi į tris žvaigždžių formavimosi žiedus, kurie yra išsidėstę ties  $\sim 6$  kpc,  $\sim 11$  kpc ir  $\sim 16$  kpc. Ryškiausio žvaigždėdaros žiedo ( $\sim 11$  kpc) pikas dera su De Somma et al. (2025) rezultatais, kurie nustatė tokią pačią vertę naudodami klasikines cefoides. Tuo tarpu žvaigždėdaros žiedas ties 16 kpc išskiria tik kaip jaunesnių (<40 mln. m.) spiečių koncentracija. Po  $\sim 40$  mln. m. spiečių tankis sumažėja  $\sim 4$  kartus, kas rodo, kad žybsnis turėjo ivykti neseniai (4.8 ir 4.9a pav.).

Galima  $\sim 11$  kpc žiedo susidarymo priežastis yra plačiai nagrinėjama Block et al. (2006); Gordon et al. (2006); Dierickx et al. (2014); Lewis et al. (2015) darbuose. Čia galima išskirti du pagrindinius scenarijus, kurie įtakojo šio žiedo atsiradimo priežastis: (i) rezonansiniai efektai M 31 galaktikos diske; (ii) susidūrimas su kaimynine galaktika kuri kirto M 31 diską. Rezonansai galaktikos diske gali būti sukelti dėl skersės sukimosi, dėl kurios gali susiformuoti trijų tipų žiedai: branduolinis, vidinis ir išorinis. 11 kpc žiedas greičiausiai yra susiformavęs išorinėje dalyje ties Lindblado rezonanso riba, kuri atsiranda tuomet, kai žvaigždžių ar duju orbitinis dažnis diske rezonouoja su skerse arba spiraline tankio banga (Binney & Tremaine 2008). Tokia sąveika gali sukelti orbitinį sutankėjimą ir duju kaupimąsi, kas dažnai lemia žiedinių struktūrų

formavimąsi. Athanassoula & Beaton (2006) parodė, kad remiantis M 31 stebėjimų ir "N-body" modelių palyginimais, išorinis Lindblado spindulys yra ties  $\sim 45 \pm 4$  arcmin, kas atitinka  $\sim 10$  kpc M 31 atstumu.

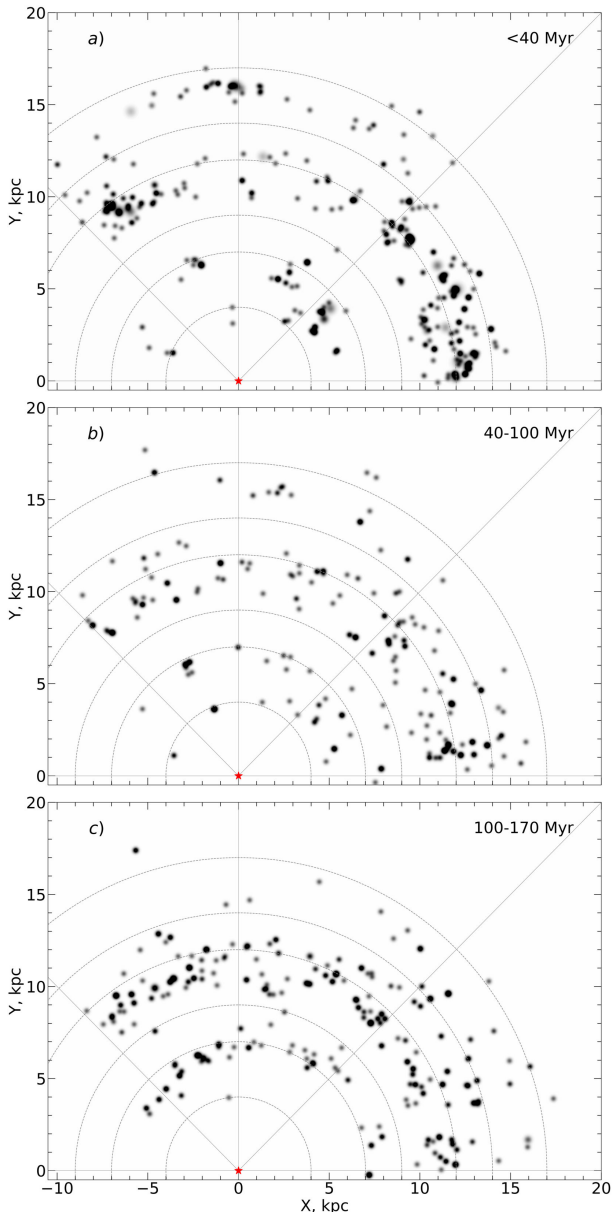
Kitas plačiai priimtas scenarijus teigia, kad žiedas susiformavo dėl praeityje įvykusių sąveikos su kaimynine galaktika M 32. Nors 11 kpc žiedas yra beveik apskritas, netoli M 32 padėties yra aiškiai matomas jo skilimas. Be to, M 31 žiedo struktūra yra fragmentuota, kas leidžia manyti, jog ji formavo išoriniai procesai, o ne vidinės sąveikos. Block et al. (2006) ir Gordon et al. (2006) atliko dinaminius modeliavimus, siekdami nustatyti ar artimas M 32 praėjimas pro M 31 diską galėjo sukelti žiedo susidarymą. Modeliavimo rezultatai parodė, kad toks susidūrimas galėjo suformuoti tankio bangą, kuri suspaudė dujas iš žiedo formos struktūrą ir paskatino žvaigždžių formavimąsi  $\sim 10$  kpc atstumu. Taip pat Block et al. (2006) ir Gordon et al. (2006) sėkmingai atkūrė stebimą žiedo skilimą, pateikdami stiprius argumentus, kad M 32 gravitacinė įtaka buvo esminis veiksny. Vis dėlto tokie modeliai susiduria su dideliais neapibrėžtumais, ypač įskaitant M 32 masės ir orbitinius parametrus, nuo kurių priklauso sąveikos pobūdis ir galutinė morfologija. Be to, Williams et al. (2015) nustatė, kad stiprus žvaigždėdaros žybsnis M 31 galaktikoje įvyko prieš 2–4 mlrd. m. Šios amžiaus ribos viršija laikotarpis, kurie buvo pasiūlyti Gordon et al. (2006) ir Block et al. (2006) darbuose. Tad stebima žiedo morfologija gali būti abiejų scenarijų padarinys.

4.9 ir 4.10 pav. pavaizduotas erdvinis žvaigždžių spiečių pasiskirstymas šeiso-se amžiaus intervalų grupėse. Kiekvienas objektas vaizduojamas kaip 2D Gauso funkcija, kurios plotis ir intensyvumas priklauso nuo spiečiaus pusės šviesio spin-dulio ir masės. Spiečių pasiskirstymas rodo, kad jauni spiečiai ( $\leq 170$  mln. m.) yra išsidėstę siauresniuose žvaigždėdaros žieduose, palyginti su vyresne spiečių populiacija ( $> 170$  mln. m.). Tai leidžia daryti prielaidą, kad spiečiai iš pradžių susiformuoja tankiose žvaigždėdaros srityse ir palaipsniui išsisklaido po galaktiką. 6 kpc žiede žvaigždėdara buvo aktyvi apie 170 mln. m., po to žiedo struktūra pradėjo nykti. Ši amžiaus riba gali būti susijusi su dinaminiu periodu toje vietoje, kuris yra  $\sim 170$  mln. m. (Chemin et al. 2009). Tuo tarpu 11 kpc žiedas yra ilgalaikis ir gan stacionarus, tame žvaigždės formavosi pastaruosius 400 mln. m., kas atitinka maždaug 1,5 dinaminio periodo. Visgi tai, kad žvaigždžių spiečiai išlieka ir iki  $\sim 400$  mln. m., rodo nedidelį sklaidos greitį spiečių grupių atžvilgiu. Todėl žvaigždžių spiečiai yra patikimi objektais, nagrinėjant žvaigždėdaros regionų morfologiją diskinėse galaktikose.

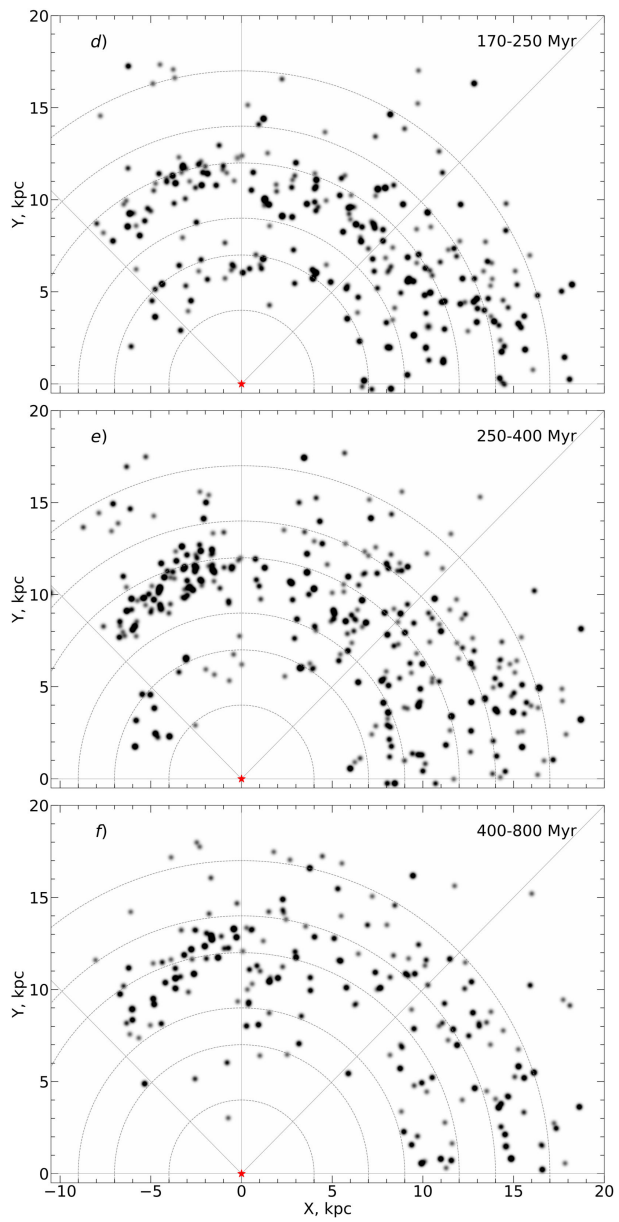
Senesni spiečiai ( $> 400$  mln. m.) yra plačiau pasiskirstę galaktikos diske. Tai gali būti paaškinama, kad spiečiai nuolat formavosi netoli žiedo centro ir didėjant amžiui jie išsisklaidė (Bastian et al. 2009; Lewis et al. 2015). Stebėtina, kad spiečių formavimosi sparta taip pat reikšmingai sumažėjo azimutiniame segmente nuo  $45^\circ$  iki  $90^\circ$ . Tuo tarpu azimutiniame segmente nuo  $-45^\circ$  iki  $0^\circ$  net ir po 400 mln. m. išlieka didesnis žvaigždžių spiečių skaičius.

## 4.6 Struktūriniai parametrai

Naudojant augimo kreives  $F475W$  fotometrinėje juoste, kiekvienam spiečiui išvedėme pusės šviesio spindulį,  $R_{50}$ .  $R_{50}$  priklausomybė nuo amžiaus,  $\log_{10}(t/\text{yr})$ , pavaizduota 4.11a pav.  $R_{50}$  vertės yra pasiskirsčiusios intervale nuo  $\sim 0,4$  pc iki  $\sim 8$  pc, ir nerodo jokios aiškios  $R_{50}$  evoliucijos nuo spiečiaus amžiaus. Mažų spiečių mažėjimą didėjant amžiui galima paaiškinti selekcijos efektais, kadangi jie néra aptinkami. Tuo



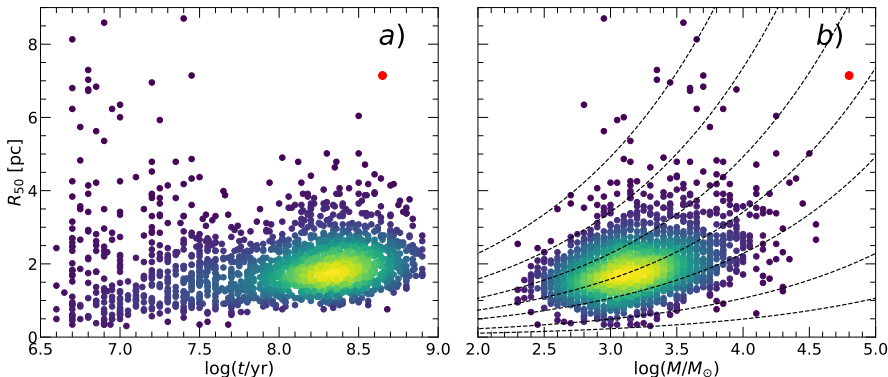
**4.9 pav.** Masyvių ( $\geq 1000 M_{\odot}$ ) žvaigždžių spiečių pasiskirstymas deprojektuotame M 31 galaktikos diske. Vertikali linija ties  $X = 0$  rodo galaktikos disko didžiają ašį. Spiečiai esantys arčiau mūsų turi neigiamas X koordinates, spiečiai esantys tolimesnėje pusėje turi teigiamas X koordinates. Apskritimai žymi 4, 7, 9, 12, 14 ir 17 kpc atstumus nuo galaktikos centro.



**4.10 pav.** 4.9 pav. тәсінys.

tarpu jauni objektai, turintys dideles  $R_{50}$  reikšmes, yra žvaigždžių asociacijos.

$R_{50}$  priklausomybė nuo masės,  $\log_{10}(M/M_\odot)$ , pavaizduota 4.11b pav., kur taip pat yra pateiktos ir fiksuotos pusės masės tankio linijos,  $\rho_{50} = 3M/8\pi R_{50}^3$ , kintančios nuo 1 iki  $10^4 M_\odot \text{ pc}^{-3}$ . Didžioji dalis M 31 galaktikos spiečių yra kompaktiški ir tankūs, jų tipiniai parametrai:  $R_{50} \sim 1,7 \text{ pc}$ ,  $\rho_{50} \sim 30 M_\odot \text{ pc}^{-3}$ ,  $M \sim 1500 M_\odot$ . Palyginimui, pietvakarinėje galaktikos dalyje tipinės vertės:  $R_{50} \sim 1,5 \text{ pc}$ ,  $M \sim 4000 M_\odot$ ,  $t \sim 100 \text{ mln. m}$ . (Kodaira et al. 2004; Narbutis et al. 2008; Vansevičius et al. 2009). Nors charakteringos amžiaus ir masės reikšmės skiriasi dėl aplinkos sąlygų ir imties atrankos ypatumų,  $R_{50}$  vertės išlieka beveik vienodos skirtinguose M 31 galaktikos regionuose.



**4.11 pav.** (a) Pusės šviesio spindulio,  $R_{50}$ , priklausomybė nuo amžiaus,  $\log_{10}(t/\text{yr})$ . (b)  $R_{50}$  priklausomybė nuo masės,  $\log_{10}(M/M_\odot)$ , su uždėtomis fiksuoto pusės masės tankio linijomis,  $\rho_h = 1, 3, 10, 30, 10^2, 10^3, 10^4 M_\odot \text{ pc}^{-3}$  (atitinkamai iš viršaus į apačią). Raudonos taškas – AP0226 spiečius.

## 4.7 Apibendrinimas

Žvaigždžių spiečių parametrai (amžius, masės, spalvos ekscesas) M 31 galaktikoje buvo nustatyti 1922 objektams, naudojant PHAT apžvalgos katalogus (Johnson et al. 2015; Naujalis et al. 2021; Kriščiūnas et al. 2023). Parametrų katalogo ištakua yra pateikta 4.1 lentelėje.

Nustatyti spiečių amžiai rodo, kad spiečių formavimosi sparta M 31 galaktikoje buvo gana pastovi per pastaruosius  $\sim 130 \text{ mln. m}$ . Visgi, maždaug prieš  $200 \pm 50 \text{ mln. m}$ , įvyko bent vienas aktyvus žvaigždėdaros epizodas, kuris galimai buvo sukeltas dėl sąveikos su M 32 galaktika prieš  $\sim 210 \text{ mln. m}$ . (Block et al. 2006). Taip pat, nustatėme sustiprėjusi spiečių formavimąsi 16 kpc spiralinėje vijoje, kuris įvyko prieš 40 mln. m.

Nustatėme spiečių masės funkcijos charakteringą vertę –  $M_C = (13, 3^{+1,3}_{-2,6}) \cdot 10^3 M_\odot$ , bei parodėme, kad  $M_C$  priklauso nuo galaktikos aplinkos.

Žvaigždžių spiečių sklaida nuo jų gimimo vietas vyksta gan lėtai. Dalis objekto žvaigždėdaros regionuose išlieka iki  $\sim 400 \text{ mln. m}$ . Todėl spiečiai yra patikimi objektai, nagrinėjant žvaigždėdaros regionų morfologiją diskinėse galaktikose.

# Išvados

Šiame darbe pritaikėme daugiaspalvę apertūrinę fotometriją 1477 žvaigždžių spiečiams M 31 galaktikoje, naudojant Panchromatic *Hubble* Andromeda Treasury (PHAT) apžvalgos duomenis (Dalcanton et al. 2012; Johnson et al. 2012, 2015). Kiekvienam objektui nustatėme ryškius pritaikant standartinę (T) ir spalvinę (C) apertūras. Ištraukos iš gautų fotometrijos katalogų pateiktos 3.1 lentelėje (T apertūros) ir 3.2 lentelėje (C apertūros).

Sujungus fotometrijos matavimų rezultatus pristatytus šiame darbe su Naujalis et al. (2021) duomenimis, sudarėme 2658 spiečių imtį kur buvo pritaikyta vienoda adaptyvios fotometrijos metodika. Parodėme, kad C apertūros fotometrijos rezultatai geriau dera su stochastiniais spiečių modeliais, kas pabrėžia apertūros pasirinkimo svarbą atliekant fotometriją tankiame galaktikos diske.

Fotometrijos tikslumą tankiuose M 31 disko regionuose apriboja dangaus fono neapibrėžumas ir lauko žvaigždžių projekcijos nagrinėjamose apertūrose. Norint gauti patikimus srauto ir spalvų matavimus, šie veiksnių turi būti kruopščiai įvertinti. Be to, spiečiai, turintys pagrindinę seką palikusių (PMS) žvaigždžių, rodo didesnį išsibarstymą ir didesnes paklaidas nei objektai be PMS žvaigždžių. Šis rezultatas atitinka Beerman et al. (2012) išvadas – PMS žvaigždžių nebuvimas leidžia tiksliau įvertinti spiečių fotometrinius parametrus ir atitinkamai patikimiau apskaičiuoti jų fizines savybes.

Remdamiesi PHAT apžvalgos fotometriniais katalogais (Johnson et al. 2015; Naujalis et al. 2021; Kriščiūnas et al. 2023), nustatėme žvaigždžių spiečių parametrus 1922 objektams. Spiečių amžiai rodo, kad per pastaruosius  $\sim$ 130 mln. m. spiečių formavimosi sparta buvo pastovi. Aktyvus žvaigždėdaros epizodas įvyko prieš  $\sim$ (200  $\pm$  50) mln. m., kurį galimai sukėlė M 32 galaktikos sąveika su M 31 prieš  $\sim$ 210 mln. m. (Block et al. 2006). Taip pat aptikome lokalų spiečių formavimosi sustiprėjimą 16 kpc spiralinėje vijoje per paskutinius 40 mln. m.

Nustatėme globalią spiečių masės funkcijos charakteringą vertę –  $M_C = (13, 3^{+1,3}_{-2,6}) \cdot 10^3 M_\odot$ . Be to, parodėme, kad galaktikos aplinka įtakoja kokios masės spiečiai bus formuojami.

Iš spiečių erdynio pasiskirstymo galaktikos diske nustatėme, kad spiečiai žvaigždžių formavimosi regionuose išlieka iki  $\sim$ 400 mln. m. Tai rodo, kad M 31 galaktikos spiečiai yra patikimi šaltiniai, nagrinėjant žvaigždėdaros regionų morfologiją diskinėse galaktikose.

# Acknowledgements

First and foremost, I would like to thank my parents Edita and Artūras for their unconditional love, support, and believing in me throughout every stage of my life and studies. Without them, everything that I do would not be possible. Their help has laid the foundation of this journey, and I am endlessly grateful for everything You have done. Ačiū!

I am also deeply thankful to my life partner, Ieva, for her patience, understanding, and unwavering support. Having you in my life is a blessing.

I am indebted to my supervisor Vladas Vansevičius for his guidance, constant help, and especially for his patience working with me. His mentorship played a vital role in shaping both this dissertation and my academic growth.

I am grateful to my colleagues Rima Stonkutė and Karolis Daugevičius for their helpful discussions, support, and for making this academic journey a more enjoyable and motivating experience.

Thank You Universe for being such a fascinating and captivating place to live in and to study.

# Gyvenimo aprašymas

**Vardas:**

Eimantas

**Pavardė:**

Kriščiunas

El. paštas:

eimantas.krisciunas@ftmc.lt

## Išsilavinimas:

2021 – 2025	Fizinių ir technologijos mokslų centras (FTMC), Megasistemų fizikos laboratorija, <i>Doktorantūra.</i>
2019 – 2021	Vilniaus universitetas, Fizikos fakultetas, <i>Fizikos magistro laipsnis.</i>
2015 – 2019	Vilniaus universitetas, Fizikos fakultetas, <i>Fizikos bakalauro laipsnis.</i>
2011 – 2015	Rygiškių Jono gimnazija, <i>Vidurinis išsilavinimas.</i>
2003 – 2011	Petro Armino progimnazija, <i>Vidurinis išsilavinimas.</i>

## Profesinė veikla:

2024-01 – dabar	Fizinių ir technologijos mokslų centras (FTMC), <i>Jaunesnysis mokslo darbuotojas.</i>
2022-11 – 2024-01	Fizinių ir technologijos mokslų centras (FTMC), <i>Vyresnysis inžinierius.</i>
2020-03 – 2022-11	Fizinių ir technologijos mokslų centras (FTMC), <i>Inžinierius.</i>

# Curriculum Vitae

**Name:** Eimantas  
**Surname:** Kriščiunas  
**E-mail:** eimantas.krisciunas@ftmc.lt

## **Education:**

- |             |  |
|-------------|--|
| 2021 – 2025 | Center for Physical Sciences and Technology<br><i>Ph.D. studies.</i> |
| 2019 – 2021 | Vilnius University, Faculty of Physics<br><i>Master's degree.</i>    |
| 2015 – 2019 | Vilnius University, Faculty of Physics<br><i>Bachelor's degree.</i>  |

## **Work experience:**

- |                   |   |
|-------------------|---|
| 2024-01 – now     | Center for Physical Sciences and Technology,<br><i>Junior Researcher.</i> |
| 2022-11 – 2024-01 | Center for Physical Sciences and Technology,<br><i>Senior Engineer.</i>   |
| 2020-03 – 2022-11 | Center for Physical Sciences and Technology,<br><i>Engineer.</i>          |

## **NOTES**

## **NOTES**

Vilnius University Press  
Saulėtekio al. 9, LT-10222 Vilnius  
e-mail: [info@leidykla.vu.lt](mailto:info@leidykla.vu.lt), [www.leidykla.vu.lt](http://www.leidykla.vu.lt)  
[bookshop.vu.lt](http://bookshop.vu.lt), [journals.vu.lt](http://journals.vu.lt)  
Print run copies 15